

Electronic Thesis and Dissertation Repository

9-23-2011 12:00 AM

Advanced Islanded-Mode Control of Microgrids

Mohammad Bagher Delghavi, *The University of Western Ontario*

Supervisor: Dr. Amirnaser Yazdani, *The University of Western Ontario*

A thesis submitted in partial fulfillment of the requirements for the Doctor of Philosophy degree
in Electrical and Computer Engineering

© Mohammad Bagher Delghavi 2011

Follow this and additional works at: <https://ir.lib.uwo.ca/etd>



Part of the [Electrical and Computer Engineering Commons](#)

Recommended Citation

Delghavi, Mohammad Bagher, "Advanced Islanded-Mode Control of Microgrids" (2011). *Electronic Thesis and Dissertation Repository*. 297.

<https://ir.lib.uwo.ca/etd/297>

This Dissertation/Thesis is brought to you for free and open access by Scholarship@Western. It has been accepted for inclusion in Electronic Thesis and Dissertation Repository by an authorized administrator of Scholarship@Western. For more information, please contact wlsadmin@uwo.ca.

ADVANCED ISLANDED-MODE CONTROL OF MICROGRIDS

(Spine title: Plib)

(Thesis format: Monograph)

by

Mohammad Bagher Delghavi

Graduate Program in Electrical and Computer Engineering

A thesis submitted in partial fulfillment
of the requirements for the degree of
Doctor of Philosophy

The School of Graduate and Postdoctoral Studies
The University of Western Ontario
London, Ontario, Canada

© Mohammad Bagher Delghavi 2011

THE UNIVERSITY OF WESTERN ONTARIO

School of Graduate and Postdoctoral Studies

CERTIFICATE OF EXAMINATION

Supervisor:

.....
Dr. Amirnaser Yazdani

Joint Supervisor:

.....

Supervisory Committee:

.....

.....

Examiners:

.....
Dr. Mehrdad Kazerani

.....
Dr. Sam Asokanthan

.....
Dr. Ilia Polushin

.....
Dr. Tarlochan S. Sidhu

The thesis by

Mohammad Bagher Delghavi

entitled:

Advanced Islanded-Mode Control of Microgrids

is accepted in partial fulfillment of the

requirements for the degree of

Doctor of Philosophy

.....
Date

.....
Chair of the Thesis Examination Board

Abstract

This thesis is focused on modeling, control, stability, and power management of electronically interfaced Distributed Energy Resource (DER) units for microgrids. Voltage amplitude and frequency regulation in an islanded microgrid is one of the main control requirements. To that end, first a mathematical model is developed for an islanded DER system and then, based on the developed model, amplitude and frequency control schemes are proposed for (i) balanced and linear loads and (ii) unbalanced and nonlinear loads. The proposed control strategy for unbalanced and nonlinear loads, utilizes repetitive control scheme to reject the effects of unbalanced and/or distorted load currents. Moreover, a new approach is proposed to maintain the effectiveness of the repetitive control under variable-frequency operational scenarios. The thesis also presents an adaptive feedforward compensation strategy to enhance the stability and robustness of the droop-controlled microgrids to droop coefficients and network uncertainties. The proposed feedforward strategy preserves the steady-state characteristics that the conventional droop control strategy exhibits and, therefore, does not compromise the steady-state power shares of the DER systems or the voltage/frequency regulation of the microgrid. Finally, a unified control strategy is proposed to enable islanded and grid-connected operation of DER systems, with no need to detect the microgrid mode of operation or to switch between different controllers, simplifying the control of the host microgrid. The effectiveness of the proposed control strategies are demonstrated through time-domain simulation studies conducted in the PSCAD/EMTDC software environment.

Keywords: Adaptive control, Current-Mode Control, Distributed Energy Resource (DER), Droop, Feedforward, Frequency Regulation, Grid-Connected Mode, Islanded Mode, Microgrid, Repetitive Control.

Dedication

To Navideh and my parents

Acknowledgements

I would like to express my sincere gratitude to Professor Amirnaser Yazdani for his excellent supervision, ideas, and encouragement throughout this research. It was a great honor for me to pursue my higher education under his supervision.

Also, financial support provided by Professor Amirnaser Yazdani and the University of Western Ontario is gratefully acknowledged.

Contents

Certificate of Examination	ii
Abstract	iii
Dedication	iv
Acknowledgements	v
List of Figures	x
List of Tables	xv
List of Appendices	xvi
Abbreviations	xvii
Nomenclature	xviii
1 Introduction	1
1.1 Statement of Problem and Thesis Objectives	1
1.2 Microgrids: Structure, Components, and Principles of Operation	2
1.2.1 Motivations and Benefits	2
1.2.2 Structure and Components	4
1.2.3 Microgrid Control	6
Overall Control (Supervisory Control)	6
Local Control (DER Control)	7
1.2.4 DER Control	8

Grid-Connected-Mode DER Control	8
Islanded-Mode DER Control	10
1.3 Thesis Contributions	11
1.4 Literature Survey Pertinent to Thesis Contributions	13
2 Islanded-Mode DER Control with Load Effect Compensation	18
2.1 Introduction	18
2.2 Structure of the Islanded DER System	19
2.3 Mathematical Model of the Islanded DER System	20
2.4 Control of the Islanded DER System	23
2.5 Study Cases and Simulation Results	27
2.5.1 Configurable Passive Load	27
2.5.2 Induction Machine Load	32
2.6 Conclusion	34
3 Islanded-Mode DER Control for Distorted Load Currents	35
3.1 Introduction	35
3.2 Structure of the Islanded Network and DER System	36
3.3 Current-Control Scheme	38
3.4 Islanded Network Voltage and Frequency Regulation	42
3.4.1 Amplitude Regulation Scheme	42
3.4.2 Frequency Regulation Scheme	44
3.5 Repetitive-Control-Based Compensator for Amplitude Regulation Scheme	46
3.5.1 Fundamentals	46
3.5.2 Extension to Variable-Frequency Systems	49
3.5.3 Closed-Loop Stability	51
3.6 Study Cases and Simulation Results	52
3.6.1 Response to Output Current Imbalance	53
3.6.2 Response to Output Current Distortion	56
3.7 Extension to Multi-System Networks	59
3.7.1 Power Sharing and Decentralized Frequency Control	59

3.7.2	Synchronization to the Network	61
3.7.3	Simulation Results for a Two-System Example Network	62
3.8	Conclusion	65
4	Stability Enhancement in Droop-Controlled Microgrids	66
4.1	Introduction	66
4.2	Structure of the DER System	67
4.3	Basic Control	69
4.3.1	Current-Control Scheme	69
4.3.2	Amplitude Regulation Scheme	69
4.3.3	Frequency Regulation Scheme	70
4.4	Proposed Adaptive Feedforward Compensation	72
4.5	Recursive Least-Square Identification Scheme	77
4.6	Study Cases and Results	79
4.6.1	Case 1: Transition to the Grid-Connected Mode Following Inaccurate Synchronization	81
4.6.2	Case 2: Network Topological Change in the Islanded Mode	84
4.6.3	Case 3: Stepwise Increase in Droop Coefficients	85
4.6.4	Case 4: Change in Load/Network Properties	86
4.7	Conclusion	89
5	Unified DER Control	90
5.1	Introduction	90
5.2	Structure of the DER System	91
5.3	Mathematical Model and Control Schemes	92
5.3.1	Current-Control Scheme	92
5.3.2	Amplitude Regulation Scheme	93
5.3.3	Frequency Regulation Scheme	96
5.3.4	Power Control Scheme	97
	Real-Power Control Scheme	98
	Reactive-Power Control Scheme	101

5.4	Application Examples	102
5.4.1	PV System	102
5.4.2	Battery Energy Storage System (BESS)	103
5.5	Study Cases and Simulation Results	104
5.5.1	Case 1: Response in the Grid-Connected Mode	106
5.5.2	Case 2: Response in the Islanded Mode	108
5.6	Conclusion	110
6	Summary, Conclusions, and Future Work	111
6.1	Summary and Conclusions	111
6.2	Future Work	112
A	Load Model and System Parameters for Chapter 2	114
A.1	Mathematical Model of the Load of Fig. 2.6	114
A.2	System Parameters	115
B	Load and System Parameters for Chapter 3	117
C	Load, System, and Asynchronous Machine Parameters for Chapter 4	119
C.1	System Parameters	119
C.2	Asynchronous Machine Parameters	119
C.3	Load and Distribution Line Parameters	121
D	Base Values and System Parameters for Chapter 5	123
	Bibliography	126
	Curriculum Vitae	132

List of Figures

1.1	Schematic diagram of an example microgrid.	5
1.2	Schematic diagram of a grid-connected DER system with voltage-mode control of real and reactive powers [10].	9
1.3	Schematic diagram of a grid-connected DER system with current-mode control of real and reactive powers.	10
1.4	Schematic diagram of a grid-connected nondispatchable DER system with current-mode control of real and reactive powers.	11
1.5	Centralized DER control.	12
1.6	Decentralized DER control.	12
2.1	Schematic diagram of a DER system in the islanded mode.	20
2.2	Block diagram of the current-control scheme.	22
2.3	Block diagram of the voltage-control scheme.	25
2.4	Equivalent block diagrams for the closed-loop voltage control scheme.	25
2.5	Block diagram of the frequency control loop.	27
2.6	Schematic diagram of the configurable passive load.	28
2.7	Start-up transient and voltage step responses of the islanded DER system under the no-load condition.	29
2.8	Start-up transient and voltage step responses of the islanded DER system under the partially-loaded condition.	29
2.9	Start-up transient and voltage step responses of the islanded DER system under the fully-loaded condition.	30
2.10	Frequency step responses of the islanded DER system under the no-load condition.	30

2.11	Frequency step responses of the islanded DER system under the partially-loaded condition.	31
2.12	Frequency step responses of the islanded DER system under a fully-loaded condition.	31
2.13	Response of the islanded DER system to sudden changes in the load configuration.	32
2.14	Response of the islanded DER system to sudden switching of the induction machine load.	33
2.15	System behavior in response to a power flow reversal and step changes in the frequency setpoint.	33
3.1	Single-line schematic diagram of the study islanded distribution network. . . .	37
3.2	Schematic diagram of islanded DER system and loads.	38
3.3	Block diagram of the current-control scheme of the DER system.	41
3.4	Block diagrams of two closed loops equivalent to the current-control scheme of Fig. 3.3.	42
3.5	Block diagram of the amplitude regulation scheme of the DER system.	44
3.6	Block diagrams of the d - and q -axis closed loops equivalent to the amplitude regulation scheme of Fig. 3.5.	45
3.7	Block diagram of the frequency regulation loop of the DER system.	46
3.8	Block diagram of a hypothetical compensator based on the internal model principle to reject a periodic disturbance input.	47
3.9	Block diagram of the discrete-time realization of the compensator of Fig. 3.8 if the disturbance input frequency is an integer sub-multiple of the sampling frequency.	48
3.10	Block diagram of the proposed repetitive-control-based compensator incorporated in the d -axis amplitude regulation loop of Fig. 3.6(a).	48
3.11	Frequency response of the FIR fractional delay filter $Q(z)$	51
3.12	Overall system response to switching from a balanced load to an unbalanced load when PI compensators are employed.	54

3.13	Zoomed view of (a) i_{oabc} , (b) v_{sabc} , and (c) PCC voltage, under unbalanced output current and PI compensators.	54
3.14	Overall system response to switching from a balanced load to an unbalanced load, when repetitive-control-based compensators are employed.	55
3.15	Zoomed view of (a) i_{oabc} , (b) v_{sabc} , and (c) PCC voltage, under unbalanced output current and repetitive-control-based compensators.	55
3.16	Overall system response to switching from a balanced load to a rectifier load, when PI compensators are employed.	57
3.17	Zoomed view of (a) i_{oabc} , (b) v_{sabc} , and (c) PCC voltage, under distorted output current and PI compensators.	57
3.18	Overall system response to switching from a balanced load to a rectifier load, when repetitive-control-based compensators are employed.	58
3.19	Zoomed view of (a) i_{oabc} , (b) v_{sabc} , and (c) PCC voltage, under distorted output current and repetitive-control-based compensators.	58
3.20	Schematic diagram of an example two-system network illustrating the application of the proposed islanded-mode control strategy in a multi-system microgrid.	60
3.21	Synchronization scheme.	62
3.22	Power sharing between the two DER systems; (a) $m = \tilde{m} = 1.0$ (rad/s)/MW, and (b) $m = 1.0$ (rad/s)/MW, $\tilde{m} = 2.0$ (rad/s)/MW.	63
3.23	Zoomed view of (a) i_{oabc} , (b) v_{sabc} , and (c) PCC voltage, under distorted and unbalanced load currents.	64
3.24	Overall response of the two-system microgrid.	64
4.1	Schematic diagram of the DER system.	68
4.2	Block diagram of the current-control scheme of the DER system.	70
4.3	Block diagram of the amplitude regulation scheme.	71
4.4	Block diagrams of the d - and q -axis closed loops equivalent to the amplitude regulation scheme of Fig. 4.3.	71
4.5	Block diagram of the frequency regulation loop.	72
4.6	Block diagram of a microgrid embedding a droop-controlled DER system. . . .	73

4.7	Block diagram of the scheme for calculation of feedforward coefficients based on the estimated parameters.	79
4.8	Schematic diagram of the test microgrid.	81
4.9	Sample responses of the DER systems to the connection of their host subnetworks to the grid, under the conventional control (Case 1).	82
4.10	Sample responses of the DER systems to the connection of their host subnetworks to the grid, under the proposed control (Case 1).	83
4.11	Estimated parameters of DER1 under the proposed control (Case 1).	83
4.12	Sample responses of the DER systems to the interconnection of the two subnetworks, under the conventional control (Case 2).	85
4.13	Sample responses of the DER systems to the interconnection of the two subnetworks, under the proposed control (Case 2).	85
4.14	Sample responses of the DER systems to stepwise increase in their droop coefficients, under the conventional control (Case 3).	87
4.15	Sample responses of the DER systems to stepwise increase in their droop coefficients, under the proposed control (Case 3).	87
4.16	Sample responses of the DER systems to the introduction of an asynchronous machine to Subnetwork1, under the conventional control (Case 4).	88
4.17	Sample responses of the DER systems to the introduction of an asynchronous machine to Subnetwork1, under the proposed control (Case 4).	88
5.1	Schematic diagram of a DER system.	92
5.2	Block diagram of the amplitude-control scheme.	94
5.3	Equivalent block diagrams for the closed amplitude-control loops.	96
5.4	Block diagram of the frequency-control loop.	97
5.5	Block diagram of the real-power control scheme.	99
5.6	Simplified model of a grid-connected DER system.	100
5.7	Block diagram of the reactive-power control scheme.	102
5.8	Block diagram of the dc-link voltage control scheme for a PV system.	104
5.9	Block diagram of the current-control scheme for a battery energy storage system.	104

5.10	Single-line schematic diagram of the test microgrid.	105
5.11	System responses in the grid-connected mode (Case 1).	107
5.12	System responses in the islanded mode (Case 2).	109
5.13	Responses of DER systems to a three-phase to ground fault (Case 2).	110
B.1	Schematic diagram of the rectifier three-phase load.	117
C.1	Schematic diagram of the single-phase network.	122

List of Tables

B.1	DER System Circuit and Control Parameters	118
C.1	DER Systems Circuit and Control Parameters	120
C.2	Asynchronous Machine Parameters (Case 4)	120
C.3	Three-Phase Load Parameters	121
C.4	Distribution Line Parameters [1/km]	121
C.5	Single-Phase Load Parameters	122
D.1	Base Values	123
D.2	DER Systems Circuit and Control Parameters [pu]	124
D.3	Load Parameters [pu]	125
D.4	Distribution Line Parameters [1/km]	125

List of Appendices

Appendix A Load Model and System Parameters for Chapter 2	114
Appendix B Load and System Parameters for Chapter 3	117
Appendix C Load, System, and Asynchronous Machine Parameters for Chapter 4	119
Appendix D Base Values and System Parameters for Chapter 5	123

Abbreviations

A/D	Analog to Digital Converter
BESS	Battery Energy Storage System
CHP	Combined Heat and Power
DER	Distributed Energy Resource
DNO	Distribution Network Operator
FIFO	First-In-First-Out
FIR	Finite Impulse Response
HV	High-Voltage
LC	Local Controller
MCC	Microgrid Central Controller
MMS	Microgrid Main Switch
MO	Market Operator
MPC	Microgrid Point of Coupling
MPPT	Maximum Power-Point Tracking
MV	Medium-Voltage
PCC	Point of Common Coupling
PI	Proportional-Integral
PLL	Phase-Locked Loop
PV	Photovoltaic
PWM	Pulse-Width Modulation
RLS	Recursive Least-Square
S/H	Sample and Hold
SISO	Single-Input-Single-Output
THD	Total Harmonic Distortion
VCO	Voltage-Controlled Oscillator
VSC	Voltage-Sourced Converter

Nomenclature

- v_{tabc} : VSC ac-side terminal voltage
 v_{sabc} : DER system terminal voltage
 v'_{sabc} : Transformer voltage
 i_{abc} : VSC ac-side current
 i_{oabc} : DER system output current
 i_{Labc} : Load current
 v_{dc} : dc-link voltage
 P_o : Output real power of DER system
 Q_o : Output reactive power of DER system
 P_{of} : Low-pass filtered measure of P_o
 Q_{of} : Low-pass filtered measure of Q_o
 P_L : Load real power
 Q_L : Load reactive power
 i_{DER} : Output current of DER
 P_{DER} : Output real power of DER
 C_{dc} : dc-link capacitance
 C_f : Capacitance of the DER system LC filter
 L : Inductance of the DER system LC filter
 R : Parasitic resistance of L (including on-state resistance of VSC valves)
 ω : dq-frame rotational speed
 ρ : dq-frame reference angle
 T_s : Sampling period
 f_s : Sampling and switching frequencies
 m : Real power droop coefficient
 n : Reactive power droop coefficient

Chapter 1

Introduction

1.1 Statement of Problem and Thesis Objectives

A microgrid is defined as a part of an electric power distribution network that embeds an appreciable number of distributed generators and energy storage devices, in addition to regional loads; it may be disconnected from the rest of the power system, under emergency conditions or as planned, and operated as an island. A microgrid can be a residential neighborhood, an industrial or commercial facility, a university campus, a hospital, an off-grid remote community, etc. Microgrids should widely utilize renewable energy resources such as wind, sunlight, and hydrogen¹, to play a significant role in the electric power systems of the future, for cleaner air, reduced transmission and distribution costs, and enablement of energy efficiency enhancement initiatives. The economical and environmental benefits of microgrids have motivated extensive research and development efforts towards resolving the technical challenges of this new and fast-growing technology.

The coexistence of multiple of energy resources, which have versatile dynamic properties and electrical characteristics, has raised concerns over the safety, efficiency, and stability of microgrids. The control and operation of a microgrid is challenging especially in an off-grid scenario where the microgrid is isolated from the main utility grid. This condition is known as the islanded mode of operation which is the main subject of this thesis.

This thesis concentrates on the islanded-mode control of electronically-interfaced distributed

¹Produced through renewable energy resources, for example using solar energy.

generators and energy storage devices, for microgrid applications. Hereafter, a generator, or an energy storage device, without its interfacing power-electronic converter is referred to as a Distributed Energy Resource (DER), whereas the same with its power-electronic interface is referred to as a “*DER system*”.

The objectives of the thesis are:

- To introduce a continuous-time mathematical model for islanded DER systems and to develop a control strategy for the regulation of the amplitude and frequency of their terminal voltages in the islanded mode of operation, for linear and balanced load conditions.
- To develop a discrete-time mathematical model and a discrete-time control strategy for the regulation of the amplitude and frequency of the terminal voltages of islanded DER systems which can also mitigate the distortions caused by nonlinear and unbalanced loads.
- To develop a discrete-time mathematical model and control strategy for droop-controlled microgrids such that dynamic interactions amongst the DER systems, and those amongst the DER systems and the loads, are tailored and the stability is enhanced.
- To develop a unified control strategy for DER systems that enables them to operate in both islanded and grid-connected modes of operation, with no need for switching between different control strategies.

1.2 Microgrids: Structure, Components, and Principles of Operation

1.2.1 Motivations and Benefits

Due to the ever-increasing demand for high-quality and reliable electric power, the concept of distributed energy resources has attracted widespread attention in recent years [1]. Distributed energy resources consist of relatively small-scale generation and energy storage devices that are interfaced with low- or medium-voltage distribution networks and can offset the local power

consumption, or even export power to the upstream network if their generation surpasses the local consumption. An upcoming philosophy of operation which is expected to enhance the utilization of distributed energy resources is known as the microgrid concept [2]- [5]. A microgrid is referred to as a part of a distribution network embedding multiple distributed energy resources and regional loads, which can be disconnected from the upstream network under emergency conditions or as planned. The main benefits of microgrids are high energy efficiency through the application of Combined Heat and Power (CHP), high quality and reliability of the delivered electric energy, and environmental and economical benefits [2].

The waste heat from the conversion of fuel to electrical power in small generators can be used by local consumers, through the CHP technology, to raise the efficiency [2].

The issue of the power quality in microgrids is an important issue due to the presence of an appreciable number of sensitive loads whose performance and lifespan can be adversely affected by voltage sags, harmonics, and imbalances. In a microgrid, however, most distributed energy resources employ power-electronic converters which can rapidly correct voltage sags, harmonics, etc., even in the presence of nonlinear and/or unbalanced loads [2]. In addition, the proximity between generation and consumption can improve the reliability of service to sensitive loads. Reliability is further enhanced by diversification and decentralization of the supply; thus, loss of one unit can be compensated for by the other units. It should be noted that the distributed energy resources of a microgrid must have plug-and-play capabilities such that they can be connected to the microgrid with zero or minimum on-site engineering [3].

The use of clean and renewable energy resources can substantially reduce harmful emissions [2]. The environmental issues have become exceedingly important in developed countries. For example, the government of Ontario plans to terminate coal-fired generation and replace it with clean energy technologies; according to a 2005 study prepared for the government, the health-related damages of coal could exceed 3 billion dollars a year. In addition, smaller generators have economical benefits such as shorter construction times and transmission lines [6].

1.2.2 Structure and Components

The main components of a microgrid are distributed generators (photovoltaic arrays, small wind turbines, fuel cells, internal combustion engines, microturbines, etc.), distributed energy storage devices (flywheels, superconductor inductors, supercapacitors, compressed-air systems, batteries, etc.), and loads. Generators can be classified into two main groups, based on their interfacing media: (i) generators that consist of direct-coupled conventional rotating machines (e.g., a synchronous generator driven by a reciprocating engine or an induction generator driven by a fixed-speed wind turbine), and (ii) electronically interfaced generators [7]. Distributed energy storage devices are employed to compensate for the power shortage within the microgrid, mainly in the islanded mode when the generators may not be able to satisfy the entire load power demand. They also prevent transient instability of the microgrid by providing power in transients. The instability would occur as many DERs, such as rotating-machine-based DERs, fuel-cells, etc., are rather slow in responding to power demand variations; the transient power shortage in a microgrid can be compensated for by a fast energy storage device, e.g., a battery that is coupled with the microgrid through a dc/ac converter [8].

Fig. 1.1 shows the schematic diagram of an example microgrid which embeds a photovoltaic (PV) system, a variable-speed wind system, and a battery energy storage system. Each DER is interfaced with its corresponding host bus through a power-electronic converter and a transformer. The microgrid is interfaced with Bus 1 of the upstream network, at the Microgrid Point of Coupling (MPC), through the Microgrid Main Switch (MMS). In turn, Bus 1 is energized from a high-voltage transmission grid, through a substation transformer. The microgrid has two operating modes: the grid-connected mode and the islanded mode. In the grid-connected mode, the MMS is closed and the microgrid can exchange energy with the host grid. In this mode, the DER systems exchange real and reactive powers with the distribution network, according to the corresponding setpoints; the difference between the aggregate power generated by the DER systems and the power demanded by the local loads is balanced by the upstream network. The voltages on both sides of the MMS are continuously monitored, and the switch can be opened to disconnect the microgrid from the grid if a fault strikes the grid. Subsequently, the microgrid can continue to operate in the so-called islanded mode. Thus,

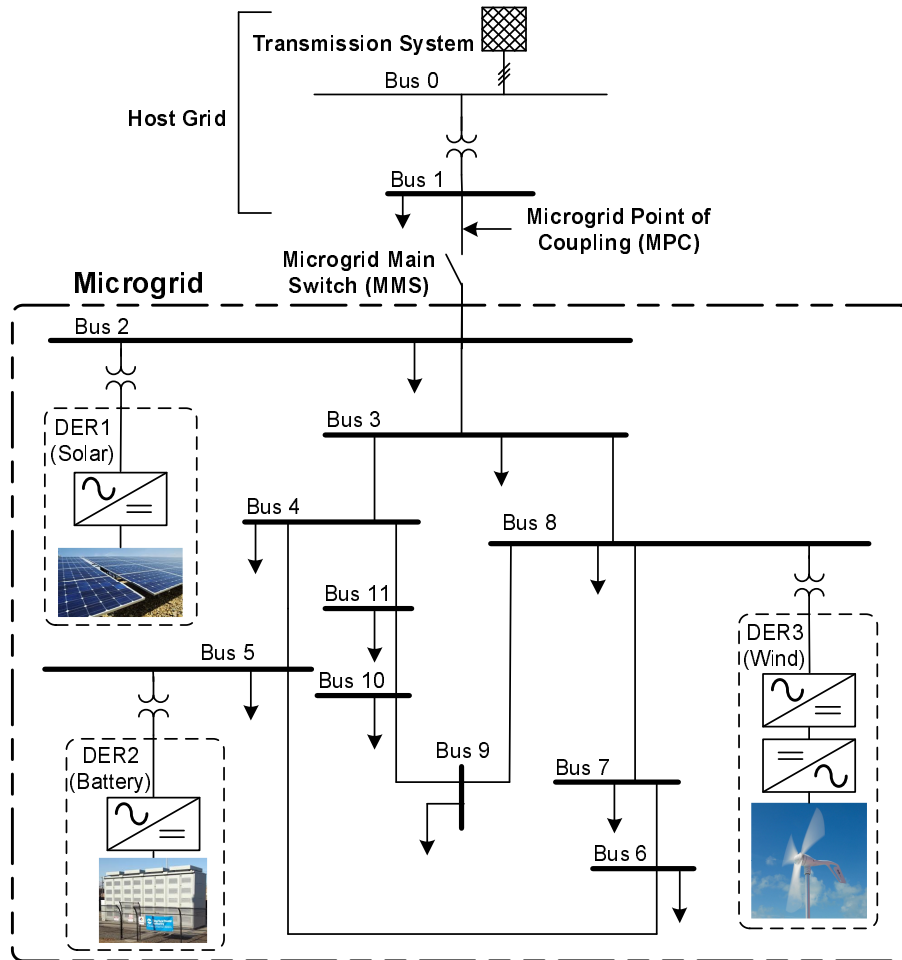


Figure 1.1: Schematic diagram of an example microgrid.

islanded operation is primarily intended to enhance system reliability and service continuity and, therefore, it is typically unplanned. However, it can also be introduced intentionally, for maintenance purposes or economical reasons. In some cases, islanded operation is the only mode of operation, e.g., in off-grid remote electrification systems.

1.2.3 Microgrid Control

Microgrid control can be broadly divided into (i) overall control and (ii) local control. These controls are described below.

Overall Control (Supervisory Control)

In the grid-connected mode, the microgrid voltage is imposed by the host utility grid. Thus, the hosted DER systems cannot play any appreciable role in determining the microgrid voltage magnitude or frequency (although they can locally affect the voltage magnitude through their reactive power or, to a lesser extent, real power contributions). However, they can be controlled to exchange pre-specified amounts of real and reactive powers with the rest of the microgrid. This, in turn, enables the control of the real and reactive powers that the microgrid exchanges, as a black box, with the host grid. In the grid-connected mode, the function of the overall control is thus to issue the real- and reactive-power commands for the DER systems. The overall control can calculate the commands based on a variety of criteria, such as market signals and economy of the microgrid; optimal operation and well being of the microgrid; host grid conditions and requirements; and microgrid internal conditions and requirements. For example, during hours when the grid electricity is cheap, the overall control may decide to reduce the power outputs of the gas microturbines and charge the energy storage devices mainly through the grid power. At the same time, in response to a grid command, it may dispatch the DER systems in such a way that the microgrid draws reactive power from the host grid, in order to prevent an overvoltage on the grid side of the MPC.

By contrast, in the islanded mode of operation, the DER systems are mainly controlled to regulate the microgrid voltage magnitude and frequency, a process that must be fast and reliable, and is the function of the local control. In the absence of a connection to the utility grid, a sustained islanded mode operation also implies that the sum of DER system power outputs equals the aggregate load power. Although, this is strictly and rapidly ensured by the local control, the overall control can specify the steady-state DER system output powers, subject to the constraint mentioned above, in such a way that the microgrid steady-state operation is optimized. The overall control can also specify the commands for steady-state voltage magni-

tudes and frequencies of the DER systems (if they have drifted away from their nominal values due to the islanded-mode operation), for the well being of the loads or safe reconnection of the microgrid to the host grid once the operating mode is to be switched to the grid-connected mode. Further, the overall control can shed loads in the islanded mode, depending on load criticalities, microgrid energy reserves, or other considerations.

The overall control is exercised centrally, through the Microgrid Central Controller (MCC). It requires a communications network to exchange information with the DER systems and loads. However, the communication links do not have to be fast or very reliable, since the overall control mainly concerns the steady-state operation of the microgrid; its malfunction shall not result in a system collapse, but would lead to the non-optimal operation of the microgrid.

In the technical literature, the overall control is also known as the “supervisory control”, which may also be augmented with higher levels of control such as Distribution Network Operator (DNO) or Market Operator (MO) [4] [9].

Local Control (DER Control)

The main function of the local control is to ensure the stability and robustness of the microgrid, in transients as well as steady states. Thus, the local control ensures that the DER systems operate in synchronism with the grid, in the grid-connected mode of operation. It also ensures that, in the islanded mode of operation, the aggregate of the DER system power outputs tracks the aggregate load power, subject to some dynamics, such that the microgrid voltage magnitude and frequency are regulated while the DER systems properly share the total load, both in transient and steady-state regimes. Further, the local control ensures that the DER systems operate within their limits and are protected against network faults, irrespective of the operating mode.

The local control also receives and enforces the commands that are issued by the overall control. As mentioned earlier, such commands include setpoints for steady-state output real and reactive powers of the DER systems; setpoints for steady-state magnitudes and frequencies of the DER system terminal voltages; and start-up, shut-down, and synchronization commands.

In contrast to the overall control, the local control must be fast and very reliable. Otherwise, either the microgrid voltage magnitude and frequency undergo unacceptable excursions with respect to their nominal values, or the microgrid collapses completely. Therefore, even though

its centralized realization is theoretically feasible, the consensus is that the local control should be implemented based on decentralized methods. The most notable decentralized method of local control is the one based on drooped characteristics. One distinct merit of the droop-based control method is that it grants plug-and-play capability to the DER systems [3]. The method will be treated in Chapter 4.

It should be pointed out that the local control may also be applied to the loads, for rapid and continuous power control, or even for load shedding. However, hereafter and throughout the rest of this thesis, the focus will exclusively be placed on the local control for the DER systems of a microgrid, and the loads are assumed to be uncontrollable. Hence, hereafter, the local control is referred more specifically to as the “*DER control*”.

1.2.4 DER Control

As discussed in Section 1.2.3, two main functions of a DER control are (i) real- and reactive-power control in the grid-connected mode, and (ii) microgrid voltage and frequency regulation in the islanded mode. These are discussed next.

Grid-Connected-Mode DER Control

In the grid-connected mode, the magnitude and frequency of the DER system terminal voltages are imposed by the utility grid. Thus, the control task boils down to the regulation of the real and reactive powers that the DER systems exchange with the host network. The DER systems can utilize either the current-mode control method or the voltage-mode control strategy, for the regulation of their output real and reactive powers.

Fig. 1.2 illustrates a simplified schematic diagram of a voltage-controlled DER system in which a DER is interfaced with the grid through a Voltage-Sourced Converter (VSC) and a three-phase inductor, L . Based on the voltage-mode control, the output real and reactive powers, P_o and Q_o , are controlled by the control of the phase-angle and amplitude of the VSC ac-side terminal voltage v_{tabc} , relative to those of the host bus voltage v_{sabc} [10]; if the resistance of the inductor is ignored, the two control variables are almost independent. Thus, each phase of the voltage to be synthesized by the VSC, v_{tabc}^* , is derived from shifting the phase-angle

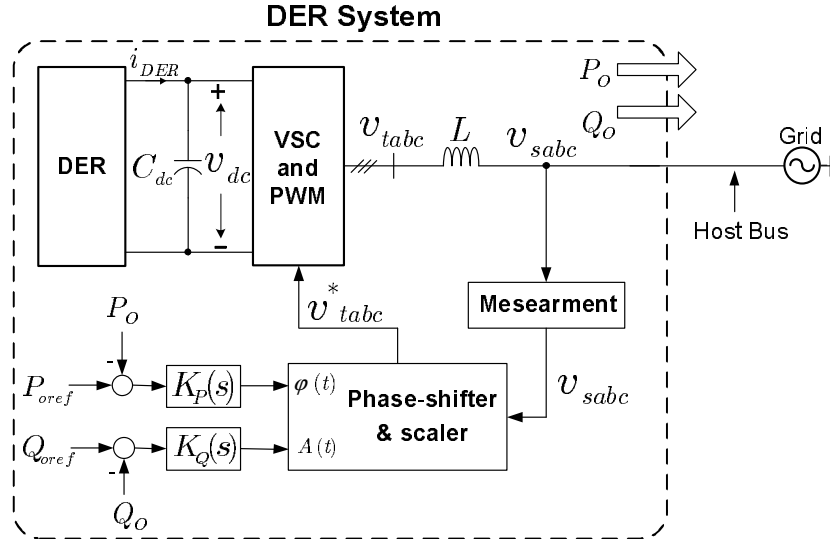


Figure 1.2: Schematic diagram of a grid-connected DER system with voltage-mode control of real and reactive powers [10].

and scaling the amplitude of the corresponding phase of v_{sabc} [10]. The required phase shift, $\phi(t)$, is determined by a feedback loop that processes the error between P_o and its respective setpoint. Similarly, the amplitude scale factor, $A(t)$, is calculated by another feedback loop that processes the error between the Q_o and its respective setpoint.

The second method for controlling the real and reactive powers of a grid-connected DER system is the current-mode control method [10]. In this approach, first the VSC line current is made controllable by a dedicated scheme and through the control of the VSC terminal voltage. Then, the real and reactive powers are controlled by the amplitude and phase angle of the current, relative to those of the host bus voltage. Due to the current regulation provision, the VSC is protected against overloads and external faults. Other advantages of the current-mode control include robustness against variations in parameters of the VSC system and the ac system, superior dynamic performance, and higher control precision [11]. Fig. 1.3 illustrates the process, which has been extensively discussed in [10].

For the voltage-mode and current-mode control strategies of Figs. 1.2 and 1.3, the DER has been assumed to be dispatchable, that is, its output real and reactive powers can be controlled by the setpoints P_{oref} and Q_{oref} (which, in turn, are determined by the MCC). By contrast, the output powers of a nondispatchable DER system are commonly the byproducts of an optimal operating condition. For example, a PV system normally operates in the Maximum Power-

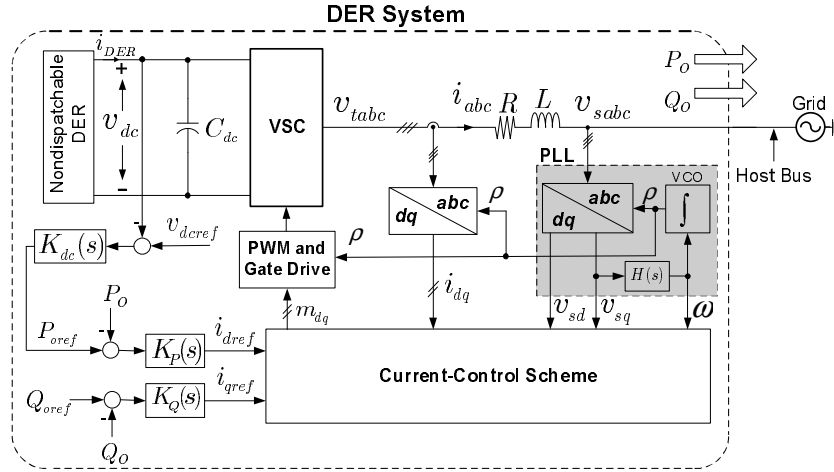


Figure 1.4: Schematic diagram of a grid-connected nondispatchable DER system with current-mode control of real and reactive powers.

shared amongst the DER systems of the microgrid. The islanded-mode control can be exercised centrally, as shown in Fig. 1.5. Centralized approaches, however, require remarkable data transfer capacities and reliable communication links [8] [13] [14]. As such, they may be suitable for small-scale microgrids in which the DER systems are close together. For DER systems that are scattered over a large geographical span, decentralized control schemes are preferable since they do not need data communications; Fig. 1.6 illustrates the concept. This thesis concentrates on the decentralized DER control, for the islanded mode of operation.

1.3 Thesis Contributions

The main contributions of this thesis can be listed as follows:

- The thesis proposes a voltage and frequency regulation strategy for islanded DER systems. Based on the proposed strategy, the frequency is regulated by controlling the q-axis component of the terminal voltage of the DER system; a Phase-Locked Loop (PLL) is employed to provide the frequency information. The proposed method is further extended to discrete-time control for a microprocessor-based implementation. The proposed discrete-time control strategy utilizes a combination of deadbeat and repetitive methods to enhance the performance of the DER system under unbalanced and/or

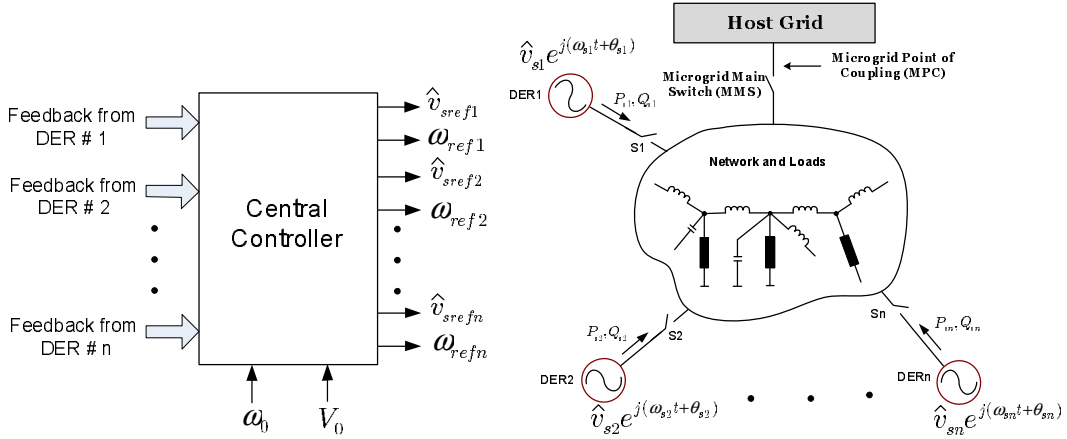


Figure 1.5: Centralized DER control.

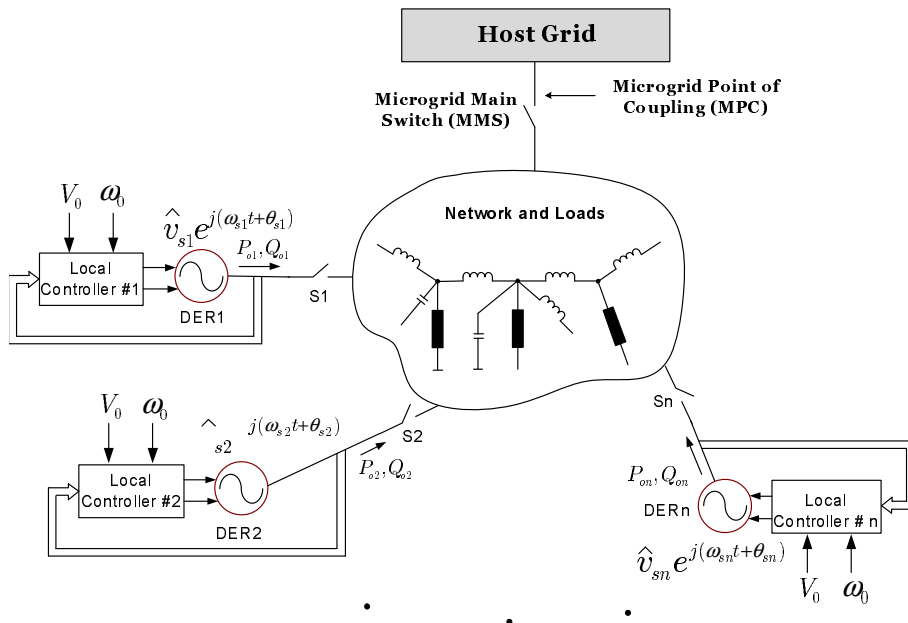


Figure 1.6: Decentralized DER control.

distorted load currents. Moreover, a new approach is proposed for maintaining the effectiveness of the repetitive control under variable-frequency scenarios.

- The thesis further proposes a discrete-time adaptive feedforward compensation strategy that alters the dynamic couplings between a DER system and its host microgrid. The objective is to enhance the stability and robustness to droop coefficients and network dynamic uncertainties. The proposed compensation strategy preserves the steady-state characteristics that the conventional droop-based control exhibits and, therefore, does

not compromise the steady-state power sharing regime of the microgrid or the regulation of its voltage magnitude and frequency. The proposed compensation is adaptive since the control is periodically modified according to the DER system steady-state operating point which, in turn, is estimated through the Recursive Least-Square (RLS) estimation technique.

- Finally, the thesis proposes a unified control strategy that allows for both the islanded and grid-connected operations of DER systems, with no need for detecting the mode of operation or switching between different controllers. The proposed unified control strategy benefits from both active feedback compensation and droop-based control; it can be directly adopted for dispatchable DER systems, e.g., battery energy storage systems, or, alternatively, in nested control loops for non-dispatchable DER systems. Further, it assumes the same power circuit, current-control structure, and synchronization mechanism as those widely used in the conventional grid-tied power-electronic systems.

1.4 Literature Survey Pertinent to Thesis Contributions

Chapters 2 and 3 of this thesis focus on the control of the amplitude and frequency of the terminal voltage of islanded DER systems; the developments of Chapter 2 are specific to balanced and linear load conditions, whereas Chapter 3 concentrates on distorted and unbalanced load conditions.

Reference [15] proposes one of the earliest and most elegant solutions to the islanded-mode control of DER systems. The control scheme proposed in [15] utilizes an *abc*-frame voltage-mode control strategy which is insensitive to load dynamic characteristics and also enables the incorporation of droop-based power sharing mechanisms. The voltage-mode control, however, renders the DER system vulnerable to external faults. Other publications in this area have primarily dealt with the issue of control robustness to loads uncertainties. In almost all of them, the developed models and control strategies are based on pre-specified, balanced, linear, load circuit configurations [16]- [21]. Therefore, in practice, the proposed methods may not necessarily guarantee the stability, robustness, or performance promised by the assumed models. In [17] the problem has been addressed by a robust control technique; the load configuration

is assumed to be known while its parameters are considered uncertain. Moreover, the method of [17] employs a voltage-mode control approach which calls for additional short-circuit protection measures. In [18] a voltage-mode control strategy has been proposed for a DER system. The method is intended for a pre-specified load configuration, but does not take into account the load topological variations. In an earlier published work, [19], a current-mode control approach has been employed. However, a parallel RL load has been assumed. Moreover, the control plant nonlinearities, inherent inter-couplings, and load dynamics are not compensated for. Consequently, the controller design task relies on linearization and is laborious, and the system performance depends on the operating point. To accommodate load imbalance, the control strategy presented in [20] has been extended in [21], based on a positive-/negative-sequence current-control strategy; again, a pre-specified linear load circuit has been assumed. In [22] a control strategy has been proposed based on a continuous-time model that includes load current feedforward, for better stability and performance. However, the control performance under unbalanced and nonlinear load conditions is not tested. In [23] a control strategy has been presented in which a feedforward scheme mitigates the impact of load dynamics on the control process; the load is assumed to be balanced, but no assumptions are made otherwise with respect to its circuit configuration or linearity. However, the operation is for a single-unit islanded system of constant frequency. Moreover, the terminal voltage becomes severely distorted under harmonically-polluted load currents.

Chapter 4 of this thesis concentrates on mitigating the dynamic interactions between the DER systems in a droop-based controlled microgrid. The droop-based control method is the most popular technique to ensure power sharing and coordinated voltage and frequency regulation in microgrids [15] [24] [25]. The popularity of the method can be attributed to its ease of implementation, based merely on local voltage and current information, in addition to the facts that it enables decentralized control of multiple DER systems, readily accommodates the grid-connected mode of operation, and enables plug-and-play operation of the DER systems.

The prime issue with respect to the conventional droop-based control is that, it is, in essence, a steady-state measure that is taken to prevent the DER systems from competing against each other, for individually imposing the network frequency and voltage; any such competition would inevitably result in a network collapse. Consequently, the transient perfor-

mance and stability of the droop-based decentralized control highly depend on the droop coefficients, and also on dynamic properties of the network, DER systems, and embedded loads [26]. Even in terms of steady-state performance, the droop-based control is effective the most for highly inductive networks, such as high-voltage transmission networks, but performs rather poorly when applied to distribution networks [27]. These dependencies, combined with the fact that the droop coefficients are commonly determined based merely on steady-state criteria [15] [24] [25], give rise to the likelihood of inaccurate power-sharing scenarios, unsatisfactory transient performances, or even instabilities, as recently noticed by researchers [26] [28]-[30].

References [26] and [7] report two studies on dynamic characteristics of islanded microgrids that embed droop-controlled electronically-coupled DER systems. In [26] the sensitivity of the overall system eigenvalues to droop coefficients is shown, whereas [7] places the emphasis on the controller parameters. Reference [29] proposes a method for improving the transient power sharing amongst the DER systems. Based on the proposed method, the magnitude and frequency of each DER system voltage are drooped also versus the derivatives/integrals of the real and reactive output powers. The method proposed in [29] is further advanced in [28] by making the droop coefficients dependant on the operating point, to mitigate the eigenvalue migration phenomenon and improve the damping of the critical eigenmodes. Based on a slightly different approach, proposed in [30], the droop coefficients of a DER system are made functions of the DER system real and reactive power outputs. In all three references, [26] [29] [30], it is assumed that a corresponding tie reactor interfaces each DER system with a common ac bus, which, in turn, is connected to a lumped load. Thus, the common bus voltage is taken as the reference voltage, and the real and reactive powers that a DER system exchanges with the network depend only on the magnitude and phase angle of the DER system terminal voltage, relative to those of the common bus voltage; however, the load is assumed to be an independent power sink and, as such, exhibits no dynamic interactions with the DER systems. Although simple, this model, which implicitly assumes a quasi steady-state condition, offers an approximate account of dynamic interactions amongst the DER systems, but obscures the existence of such interactions with the network/loads. The reason is that the DER system terminal voltages are functions of both dynamic and steady-state power flows within the overall network and,

thus, depend also on the loads. Reciprocally, the loads' real and reactive powers are functions of the network voltage and frequency. Consequently, in practice, the aforementioned simplified model may not guarantee system stability or a satisfactory performance.

On the other hand, due to the diversities in network topologies and equipment, dynamics of a real-life network are typically governed by complex dynamic models [7] [26] [31], even for relatively small networks with loads of pre-specified, e.g., RL, configurations. Consequently, the incorporation of network/load dynamics into the control design process is understandably involved [32], does not promise sufficient generality, and expectedly renders the design prone to case-by-case refinements and compromises the capability for plug-and-play operation.

Chapter 5 of the thesis deals with simplification of the DER control in microgrids. Microgrids require cooperation of multiple distributed energy resources (DERs) in both the islanded mode and the grid-connected mode [2]. This requirement presents the control of DERs, in particular electronically interfaced DERs, with a major challenge as the two modes of operation adhere to different and somewhat conflicting dynamic and steady-state characteristics. For example, in the grid-connected mode, the microgrid voltage and frequency are dictated by the utility grid and, thus, the DERs should act as controllable current sources which exchange energy with the host network (current-mode control strategy). In the islanded mode of operation, however, it is the collective responsibility of the DERs to regulate the microgrid voltage and frequency – a goal that can be achieved most effectively and conveniently if the DERs act as controllable voltage sources (voltage-mode control strategy) [15]. Therefore, researchers have indicated the need for two distinct sets of controllers, one for the grid-connected mode and the other one for the islanded mode. This approach, in turn, calls for a fast islanding detection strategy that detects the microgrid prevailing mode of operation and islanding instant, in order to activate the corresponding set of controllers [32]- [36].

The main issue associated with the aforementioned two-controller approach is that it makes the microgrid performance heavily reliant on the speed and accuracy of the islanding detection process, especially in transient regimes. To the authors' best of knowledge, there still exists no conclusive islanding detection method, and the research in this area continues. Having the knowledge of microgrid operating mode and moment of islanding should not be a pre-requisite for the microgrid control at the DER level, but may be employed at the supervisory control

level where reliability does not have to be high. Further, there already exists a great deal of experience, well-established circuit configurations, and control algorithms for grid-connected power-electronic interface systems [10]. Hence, from product development and manufacturing standpoints, it is highly desirable that DERs employ the same circuit configurations, feedback signals, and transducers also for the off-grid operation.

Reference [15] has shown that the conventional $P - \omega$ droop-based control is also effective for (real) power output control in the grid-connected mode. The shortcoming of this approach, however, is that the dynamics of the power control process are fixed by the droop coefficient (which is chosen for proper power sharing in the islanded mode, based on a steady-state criterion [15]) and, consequently, cannot be tailored. Moreover, the proposed control method is based on the voltage-mode control strategy and thus vulnerable to output shorts and network faults. Reference [16] proposes a unified control method based on the current-mode control strategy. To be able to tailor the dynamics, however, the proposed method assumes a two-DER-unit microgrid and a specific load configuration.

Chapter 2

Islanded-Mode DER Control with Load Effect Compensation

2.1 Introduction

As illustrated by Figs. 1.5 and 1.6, a DER control task requires rapid and faithful regulation of the magnitude and frequency of the DER system terminal voltage. The main difficulty, however, is the impact of the load current on the control performance. This chapter proposes a voltage and frequency regulation strategy that mitigates the load impact. The method will be extended in Chapter 3 to include nonlinear and unbalanced loads.

The proposed control employs a feedforward compensation strategy to mitigate the impact of nonlinearities, to eliminate the inter-couplings, and to compensate for the load dynamics. Therefore, the load dynamics are masked and the system performance is made, to a great extent, independent of the load type. Thus, the closed-loop system possesses very similar dynamic properties under no-load and loaded conditions. In addition, the control plant turns out to be linear, in turn, permitting utilization of classical control design methods and optimization of the control loops for a stable operation and satisfactory performance over a wide range of operating points.

The proposed control strategy takes advantage of a PLL and thus avoids the use of an external frequency synthesizer. Furthermore, under the proposed control strategy, the islanded DER system possesses black-start capability and is robust against load switching incidents. Another

merit of the proposed control is that it allows the DER system to preserve the construction and control architecture that are established and optimized for grid-connected power-electronic systems; these include six-pulse pulse-width modulated VSCs, three-phase ac filters, current-mode control schemes, synchronous dq reference frames, and PLLs.

The chapter details the mathematical modeling and control design methodology, and demonstrates the effectiveness of the proposed method through simulation studies conducted on a detailed switched model of the overall system, in the PSCAD/EMTDC environment.

2.2 Structure of the Islanded DER System

Fig. 2.1 illustrates a simplified schematic diagram of a DER system, consisting of a current-controlled VSC and a three-phase LC filter, that supplies an isolated distribution network; an aggregate of the network loads as viewed from the DER system terminals is labeled as the “effective load” and is referred to as the “load” throughout this chapter. L and C_f represent the inductance and capacitance of the filter. R models the ohmic loss of the filter inductor and also includes the effect of the on-state resistance of the VSC valves. The VSC dc side is paralleled with the dc-link capacitor C_{dc} and a voltage source. The voltage source models the effect of a dispatchable energy storage device, e.g., a battery, which is coupled with the VSC from the dc side.

Fig. 2.1 illustrates that the DER system is controlled in a rotating dq reference frame whose d axis makes an angle ρ against the stationary α axis. ρ is obtained from a PLL which constitutes an essential part of a modern DER system. The PLL also provides ω , i.e., the frequency of v_{sabc} . In the grid-connected mode of operation, v_{sabc} is dictated by the grid in which case ρ and ω represent the phase-angle of the host bus voltage and power system frequency, respectively. In the islanded mode, however, the switch S is open and the DER system of Fig. 2.1 solely supplies the load. Thus, the control objective is to regulate the amplitude and frequency of the host-bus/load voltage, i.e., v_{sabc} . Ideally, this should be accomplished in a stable manner and irrespective of the load dynamic characteristics.

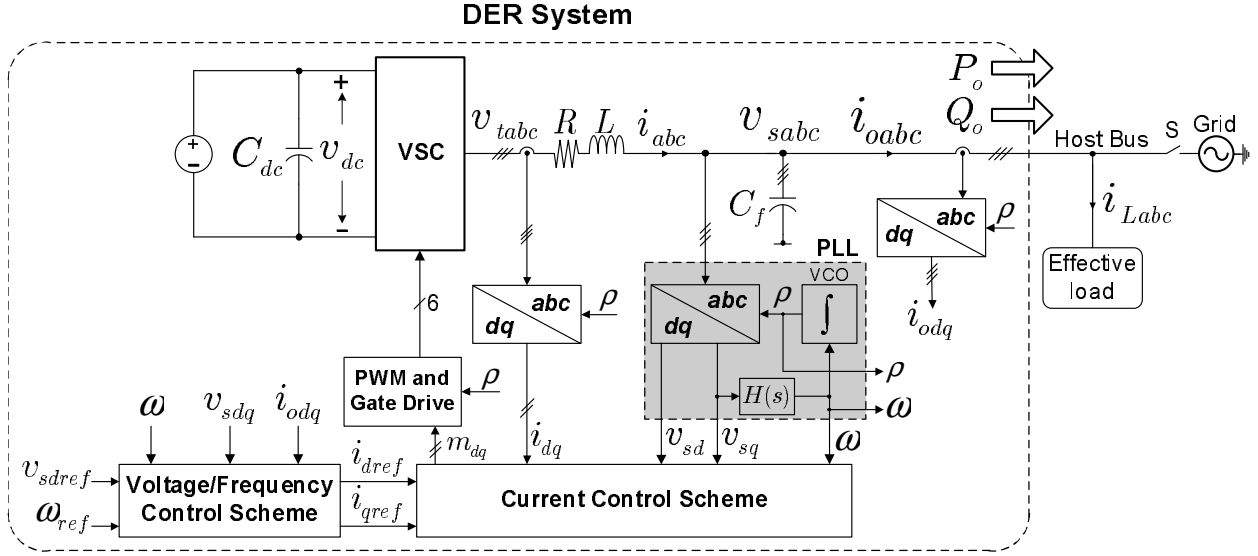


Figure 2.1: Schematic diagram of a DER system in the islanded mode.

2.3 Mathematical Model of the Islanded DER System

With reference to Fig. 2.1, dynamics of the host-bus/load voltage are described by the space-phaser equation

$$C_f \frac{d}{dt} \vec{v}_s = \vec{i} - \vec{i}_o, \quad (2.1)$$

where each space phasor is defined by the generic equation $\vec{f}(t) = (2/3)(f_a(t)e^{j0} + f_b(t)e^{j2\pi/3} + f_c(t)e^{j4\pi/3})$ in which $f_a(t)$, $f_b(t)$, and $f_c(t)$ constitute a three-phase signal or (current/voltage) waveform. Replacing each $\vec{f}(t)$ (i.e., \vec{v}_s , \vec{i} , and \vec{i}_o) with $(f_d(t) + jf_q(t))e^{j\rho(t)}$ in (2.1), one derives the dq -frame equivalent of (2.1) as

$$C_f \frac{d}{dt} [(v_{sd} + jv_{sq})e^{j\rho}] = (i_d + ji_q)e^{j\rho} - (i_{od} + ji_{oq})e^{j\rho}, \quad (2.2)$$

where $\rho(t)$ is the dq -frame angle. Equation (2.2) can be simplified and split into

$$C_f \frac{dv_{sd}}{dt} = (C_f \omega) v_{sq} + i_d - i_{od} \quad (2.3)$$

$$C_f \frac{dv_{sq}}{dt} = -(C_f \omega) v_{sd} + i_q - i_{oq}, \quad (2.4)$$

where

$$\frac{d\rho}{dt} = \omega(t) \quad (2.5)$$

is the output of the PLL.

As shown in Fig. 2.1, the PLL processes v_{sq} through the filter $H(s)$ and determines ω in such a way that v_{sq} is forced to zero [37]. In the grid-connected mode of operation v_{sabc} is dictated by the grid. This indicates that the real and reactive power that the DER system delivers to the distribution network are controlled by i_d and i_q , respectively. In the grid-connected mode, in a steady state, ω becomes equal to ω_0 , i.e., the power system angular frequency, while v_{sq} settles at zero. In order for that to happen, $H(s)$ must possess at least one pole at $s = 0$. The PLL is described by

$$\Omega(s) = H(s)V_{sq}(s), \quad (2.6)$$

which holds also for the islanded mode where v_{sabc} is not imposed by the grid, but is a variable based on (2.1).

As mentioned in the previous section, the electronic interface of the DER system employs a current-controlled VSC. Thus, the current components i_d and i_q are independently controlled through their respective reference commands, based on [38]

$$I_d(s) = G_i(s)I_{dref}(s) = \frac{1}{\tau_i s + 1} I_{dref}(s) \quad (2.7)$$

$$I_q(s) = G_i(s)I_{qref}(s) = \frac{1}{\tau_i s + 1} I_{qref}(s), \quad (2.8)$$

where the time-constant τ_i is a design choice. The current control is implemented based on the block diagram of Fig. 2.2 in which the compensator $K_i(s)$ is Proportional-Integral (PI) filter. Fig. 2.2 shows that ω is included in the current-control process as a feedforward term to decouple the control of i_d and i_q .

In the islanded mode of operation, the DER system output current is equal to the load current, i.e., $i_{oabc} = i_{Labc}$. The load current components i_{Ld} and i_{Lq} are regarded as the outputs

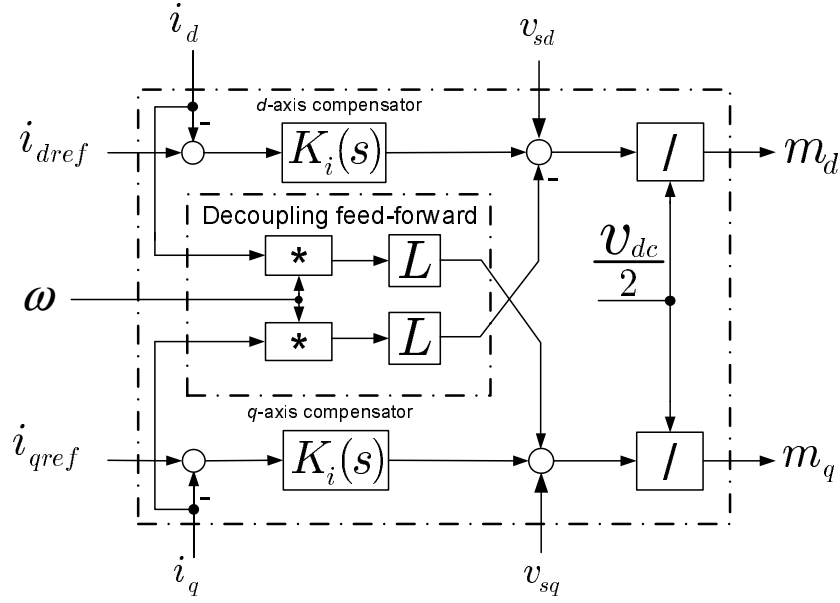


Figure 2.2: Block diagram of the current-control scheme.

of the following nonlinear, time-variant, dynamic system whose inputs are v_{sd} and v_{sq} :

$$\begin{bmatrix} \dot{i}_{od} \\ \dot{i}_{oq} \end{bmatrix} = \begin{bmatrix} \dot{i}_{Ld} \\ \dot{i}_{Lq} \end{bmatrix} = \begin{bmatrix} g_1(x_1, x_2, \dots, x_n, v_{sd}, v_{sq}, t, \omega) \\ g_2(x_1, x_2, \dots, x_n, v_{sd}, v_{sq}, t, \omega) \end{bmatrix}, \quad (2.9)$$

$$\frac{d}{dt} \begin{bmatrix} x_1 \\ x_2 \\ \cdot \\ \cdot \\ \cdot \\ x_n \end{bmatrix} = \begin{bmatrix} f_1(x_1, x_2, \dots, x_n, v_{sd}, v_{sq}, t, \omega) \\ f_2(x_1, x_2, \dots, x_n, v_{sd}, v_{sq}, t, \omega) \\ \cdot \\ \cdot \\ \cdot \\ f_n(x_1, x_2, \dots, x_n, v_{sd}, v_{sq}, t, \omega) \end{bmatrix}, \quad (2.10)$$

where $x_1(t), \dots, x_n(t)$ signify the state variables of the load; $f_1(\cdot), \dots, f_n(\cdot), g_1(\cdot)$, and $g_2(\cdot)$ are nonlinear functions of their corresponding arguments.

Equations (2.3) through (2.10) constitute a mathematical model for the islanded system of Fig. 2.1.

2.4 Control of the Islanded DER System

In the islanded mode, the control of the DER system involves regulation of the host bus line-to-neutral voltage magnitude, i.e., $\widehat{v}_s = \sqrt{v_{sd}^2 + v_{sq}^2}$, and the frequency ω . As explained in Section 2.3, v_{sq} settles at zero in a steady state. Therefore, the regulation of the voltage magnitude boils down to that of v_{sd} . On the other hand, based on (2.6), the frequency can be controlled by v_{sq} . However, control of v_{sd} and v_{sq} is not a straightforward task. The reasons are (i) based on (2.3) through (2.10), the open-loop control plant (with i_{dref} and i_{qref} as the inputs, and v_{sd} and v_{sq} as the outputs) is nonlinear; (ii) based on (2.3) and (2.4), dynamics of v_{sd} and v_{sq} are coupled; (iii) as (2.9) and (2.10) indicate, i_{od} and i_{oq} are functions of both v_{sd} and v_{sq} , most likely, with uncertain and time-varying parameters; and (iv) dynamics of the load are, in general, highly inter-coupled, of a high dynamic order, and nonlinear, even for a fairly simple linear load; an example of this is presented in Appendix A.

Fig. 2.3 illustrates a control scheme, capable of largely overcoming the foregoing issues, in which the filters $K_v(s)$ are the compensators for the d - and q -axis control loops. Fig. 2.3 shows that feedforward signals are utilized to eliminate the coupling between v_{sd} and v_{sq} . The decoupling mechanism employed here is similar to that used to decouple i_d and i_q in the current-control scheme of Fig. 2.2. The control scheme of Fig. 2.3 enables independent control of v_{sd} and v_{sq} , respectively, by i_{dref} and i_{qref} . Fig. 2.3 also shows that measures of i_{od} and i_{oq} are included in the control process as two other feedforward signals, to mitigate the impact of the load dynamics on v_{sd} and v_{sq} . Hence, the compensated system behaves under all load conditions in approximately the same way as the uncompensated system would behave under a no-load condition. The reason for the effectiveness of the control scheme of Fig. 2.3 can be understood based on the following discussions.

As Fig. 2.3 shows, one has

$$i_{dref} = u_d - (C_f \omega) v_{sq} + i_{od} \quad (2.11)$$

$$i_{qref} = u_q + (C_f \omega) v_{sd} + i_{oq}, \quad (2.12)$$

where u_d and u_q are two dummy control inputs. Substituting for i_{dref} and i_{qref} , from (2.11) and (2.12), in (2.7) and (2.8), one obtains

$$I_d = G_i(s)U_d - C_f G_i(s)\mathfrak{L}\{\omega v_{sq}\} + G_i(s)I_{od} \quad (2.13)$$

$$I_q = G_i(s)U_q + C_f G_i(s)\mathfrak{L}\{\omega v_{sd}\} + G_i(s)I_{oq}, \quad (2.14)$$

where $\mathfrak{L}\{\cdot\}$ denote the Laplace transform operator. It then follows from applying Laplace transform to both sides of (2.3) and (2.4), and substituting for $I_d(s)$ and $I_q(s)$ from (2.13) and (2.14), in the resultants, that

$$C_f s V_{sd} = G_i(s)U_d + \underbrace{C_f[1 - G_i(s)]\mathfrak{L}\{\omega v_{sq}\} - [1 - G_i(s)]I_{od}}_{\text{transient terms}} \quad (2.15)$$

$$C_f s V_{sq} = G_i(s)U_q - \underbrace{C_f[1 - G_i(s)]\mathfrak{L}\{\omega v_{sd}\} - [1 - G_i(s)]I_{oq}}_{\text{transient terms}}. \quad (2.16)$$

It is then noted that the transfer function $G_i(s) = 1/(\tau_i s + 1)$ has a unity dc gain, and therefore $[1 - G_i(s)] = \tau_i s/(\tau_i s + 1)$ has a zero dc gain. Hence, if τ_i is adequately small, those terms of (2.15) and (2.16) which are labeled as “*transient terms*” assume negligible values, and (2.15) and (2.16) can be approximated as

$$\frac{V_{sd}(s)}{U_d(s)} \approx G_i(s) \frac{1}{C_f s} \quad (2.17)$$

$$\frac{V_{sq}(s)}{U_q(s)} \approx G_i(s) \frac{1}{C_f s}. \quad (2.18)$$

Equations (2.17) and (2.18) indicate that v_{sd} and v_{sq} can be independently controlled by, respectively, u_d and u_q . This alternatively means that the control scheme of Fig. 2.3 divides the overall voltage control plant, effectively, into two independent Single-Input-Single-Output (SISO) plants of Fig. 2.4. To design $K_v(s)$, one notes that each loop in Fig. 2.4 includes an integral term, i.e., a pole at $s = 0$, and a real pole at $s = -p = -1/\tau_i$. For such a plant, a PI compensator can ensure a stable fast response and zero steady-state error, if the following procedure is exercised [39].

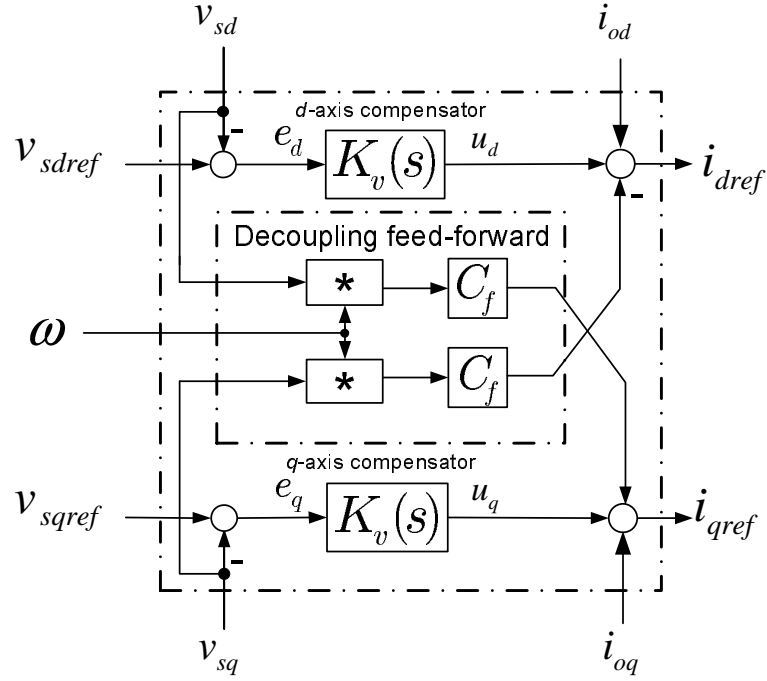


Figure 2.3: Block diagram of the voltage control scheme.

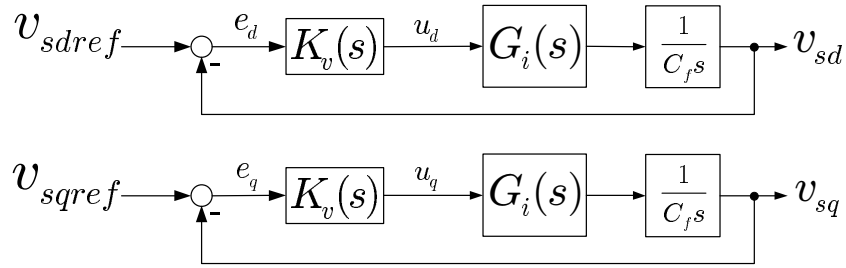


Figure 2.4: Equivalent block diagrams for the closed-loop voltage control scheme.

Let

$$K_v(s) = k \frac{s+z}{s}, \quad (2.19)$$

where k and $-z$ are the compensator gain and zero, respectively. Then, the open-loop gain is

$$\ell(s) = \frac{k}{\tau_i C_f} \left(\frac{s+z}{s+p} \right) \frac{1}{s^2}. \quad (2.20)$$

At very low frequencies, the open-loop phase $\angle \ell(j\omega)$ is approximately equal to -180° . If $z < p$, then $\angle \ell(j\omega)$ first increases until reaches its maximum, δ_m , at $\omega = \omega_m$. For $\omega > \omega_m$, $\angle \ell(j\omega)$

drops and approaches -180° at very high frequencies. Therefore, to achieve the maximum phase-margin, one should pick the gain crossover frequency as $\omega_c = \omega_m$, and δ_m becomes the phase-margin. Knowing δ_m , z can be calculated from

$$\sin \delta_m = \frac{(p/z) - 1}{(p/z) + 1}. \quad (2.21)$$

The gain crossover frequency is determined based on

$$\omega_c = \sqrt{p \times z}. \quad (2.22)$$

The compensator gain, k , is obtained from the solution to $|\ell(j\omega_c)| = 1$, that is

$$k = C_f \omega_c. \quad (2.23)$$

Based on the above-mentioned design procedure, the resultant closed-loop voltage control system is of the third order. It can be shown that the closed-loop system always has a real pole at $s = -\omega_c$, while the two other complex-conjugate poles are located on a circle whose radius is ω_c . The exact locations of the two poles depend on the phase margin which is typically chosen in the range of 30° to 75° . For the particular choice of $\delta_m = 53^\circ$, the two poles are $s = -\omega_c$ and thus the closed-loop system has a triple pole at $s = -\omega_c$.

In Fig. 2.3, v_{sdref} is set to \widehat{v}_{sn} , that is the nominal peak value of the host bus line-to-neutral voltage. However, v_{sqref} is issued by another control loop to regulate ω , as shown in Fig. 2.5. For this loop, the compensator $K_\omega(s)$ can be as simple as a pure gain. This however results in no steady-state error since $H(s)$ includes an integral term.

It should be pointed out that for the grid-connected mode of operation, i_{dref} and i_{qref} are not obtained from the voltage control scheme of Fig. 2.3; rather, they are determined based on the real and reactive power that the DER system is expected to exchange with the grid as

$$\begin{aligned} i_{dref} &= P_{oref} / (1.5\widehat{v}_{sn}) \\ i_{qref} &= -Q_{oref} / (1.5\widehat{v}_{sn}) + C_f \omega_0 \widehat{v}_{sn}. \end{aligned}$$

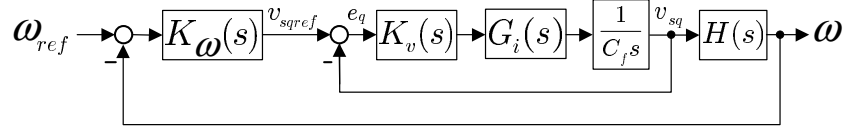


Figure 2.5: Block diagram of the frequency control loop.

2.5 Study Cases and Simulation Results

In this section, the performance of the DER system of Fig. 2.1, with a capacity of 5.0 MVA, is evaluated under the proposed control strategy. Thus, a detailed switched model of the overall system is simulated using the PSCAD/EMTDC software package [40]; the simulation time step is $10 \mu\text{s}$. Two types of loads are considered: (i) the configurable passive load of Fig. 2.6, and (ii) an induction machine. For the DER system, $v_{sdref} = 500 \text{ V}$ and $\omega_{ref} = 377 \text{ rad/s}$, unless otherwise mentioned. In the graphs, voltages are expressed in V, currents in A, frequency and rotational speeds in rad/s, real powers in MW, and reactive powers in MVar. The parameters of the system and the loads are given in Appendix A.

2.5.1 Configurable Passive Load

The first case study demonstrates the response of the DER system to the start-up transient and stepwise changes in v_{sdref} , when the configurable load of Fig. 2.6 is energized. To ensure a soft start-up process, v_{sdref} is ramped up from zero to 500 V, and is kept constant from $t = 0.02 \text{ s}$ onwards. Then, v_{sdref} is subjected to two step changes, one from 500 to 550 V, and the other one from 550 to 500 V, respectively, at $t = 0.05$ and 0.1 s . Figs. 2.7 through 2.9 illustrate the responses of the islanded DER system to the aforementioned sequence of events, for the no-load condition (i.e., when both Switch #1 and Switch #2 are open), the partially-loaded condition (i.e., when Switch #1 is closed but Switch #2 is open), and the full-load condition (when both Switch #1 and Switch #2 are closed), respectively.

Figs. 2.7 to 2.9 indicate that, based on the proposed control strategy, the system responds similarly under all three load conditions. In other words, the dynamic properties of the closed-loop system are, to a large extent, independent of the load dynamic characteristics. It is observed that, in all three cases, the host-bus/load voltage tracks its reference value in less than 6 ms, exhibiting a well-damped response. The figures also show that v_{sq} and ω remain unaffected

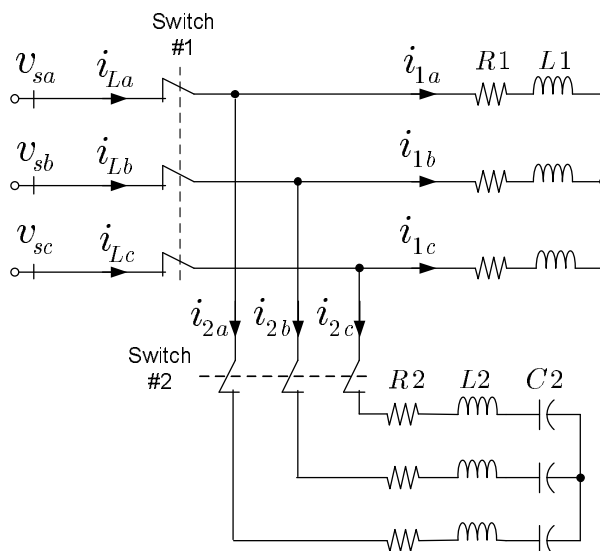


Figure 2.6: Schematic diagram of the configurable passive load.

subsequent to the changes in v_{sd} ; this is due to the dynamic decoupling strategy of Section 2.4.

Figs. 2.10 to 2.12 show the performance of the DER system in response to stepwise changes in ω_{ref} , respectively, for the no-load, partially-loaded, and fully-loaded conditions. Thus, ω_{ref} is step-changed from 377 to 400 rad/s, at $t = 0.05$ s, and is changed back to 377 rad/s at $t = 0.1$ s. It is observed that in all three cases, the frequency rapidly tracks its reference command. Moreover, while the change in the frequency disturbs v_{sq} , as expected, its impact on v_{sd} and therefore on the host-bus/load voltage is insignificant.

It should be pointed out that the frequency is usually not changed in practice. Here, the foregoing case study is used as a test means for evaluating the control design and performance.

Fig. 2.13 illustrates the performance of the DER system in response to sudden load switching incidents. Initially, the system is in a steady state, while both Switch #1 and Switch #2 are open and the system operates under a no-load condition. At $t = 0.05$ s, Switch #1 is closed and the RL branch of the load is switched on. This load, introduced earlier as the partial load, corresponds to a power rating of 3.28 MW and a lagging power-factor of 0.85. Subsequent to the load energization, the load current increases and, as Fig. 2.13 shows, i_{Ld} and i_{Lq} develop. It is noted that since the load is inductive, i_{Lq} settles at a negative value.

At $t = 0.1$ s, Switch #2 is also closed and the RLC branch of the load is brought into operation. This configuration, i.e., the full-load, corresponds to the power rating of 3.9 MW

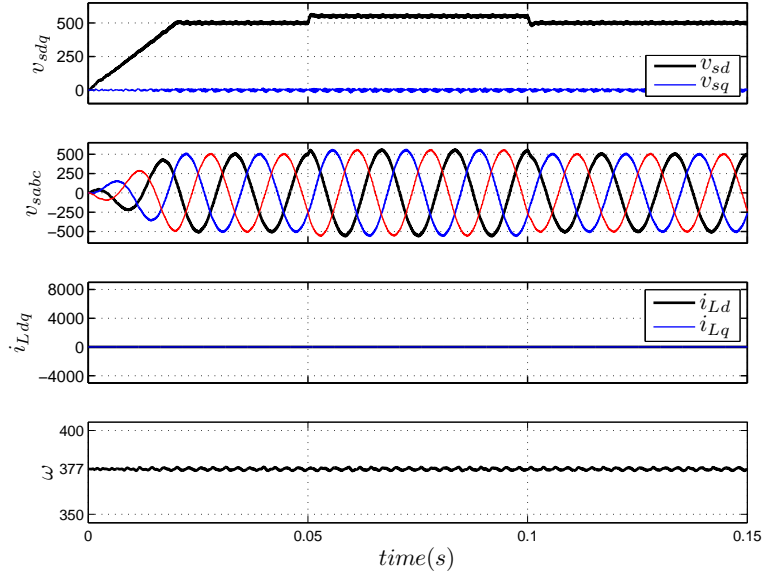


Figure 2.7: Start-up transient and voltage step responses of the islanded DER system under the no-load condition.

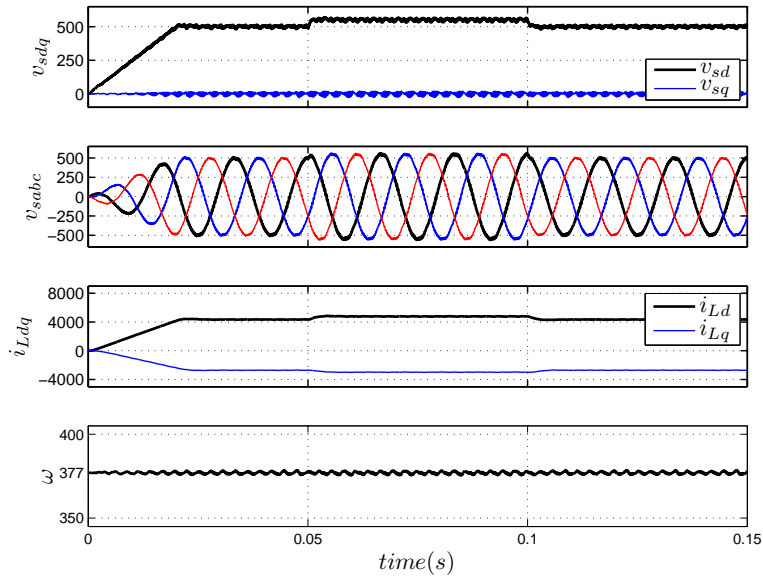


Figure 2.8: Start-up transient and voltage step responses of the islanded DER system under the partially-loaded condition.

and the unity power-factor. Thus, i_{Lq} approaches the steady-state value of zero, whereas i_{Ld} exhibits a large overshoot subsequent to the switching incident. The overshoot is due to the charging current of the capacitor C_2 .

At $t = 0.15$ s, Switch #2 is opened and the RLC branch of the load is switched off. Therefore, the load configuration and the system operating condition become identical to those for

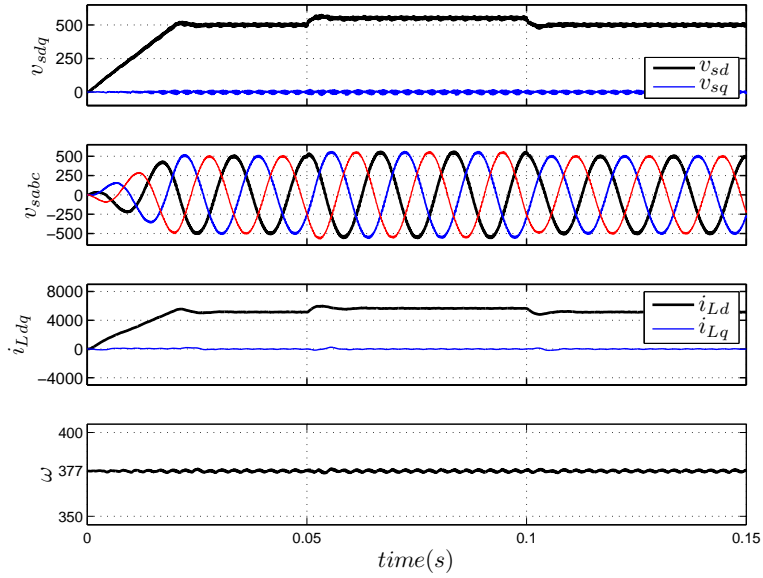


Figure 2.9: Start-up transient and voltage step responses of the islanded DER system under the fully-loaded condition.

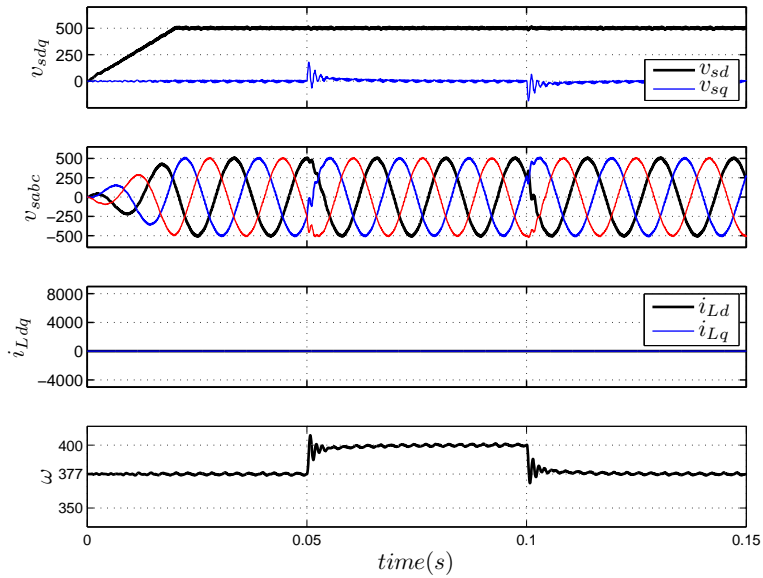


Figure 2.10: Frequency step responses of the islanded DER system under the no-load condition.

the time interval between 0.05 and 0.1 s. At $t = 0.2$ s, Switch #1 is also opened and the remainder of the load is switched off. Thereafter, the system continues operation under the no-load condition.

Fig. 2.13 indicates that, despite the load switching events, the host-bus/load voltage and frequency are well regulated, and the disturbances are rejected rapidly. The largest excursion

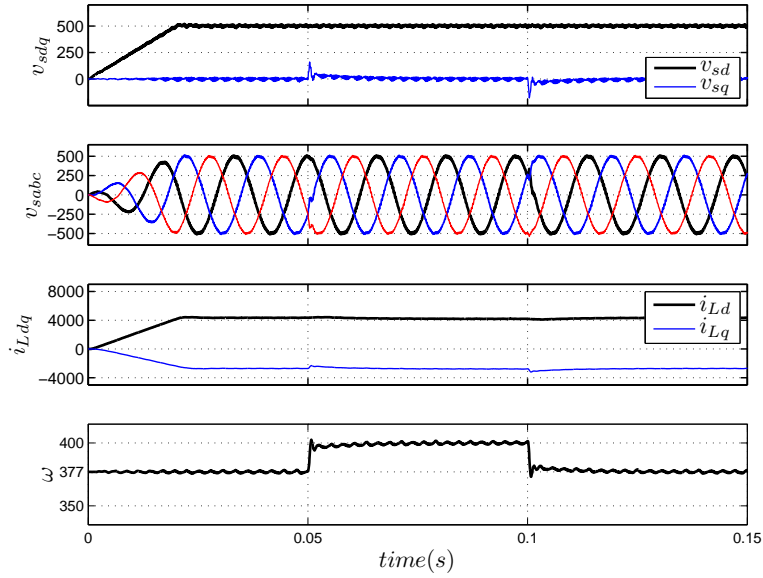


Figure 2.11: Frequency step responses of the islanded DER system under the partially-loaded condition.

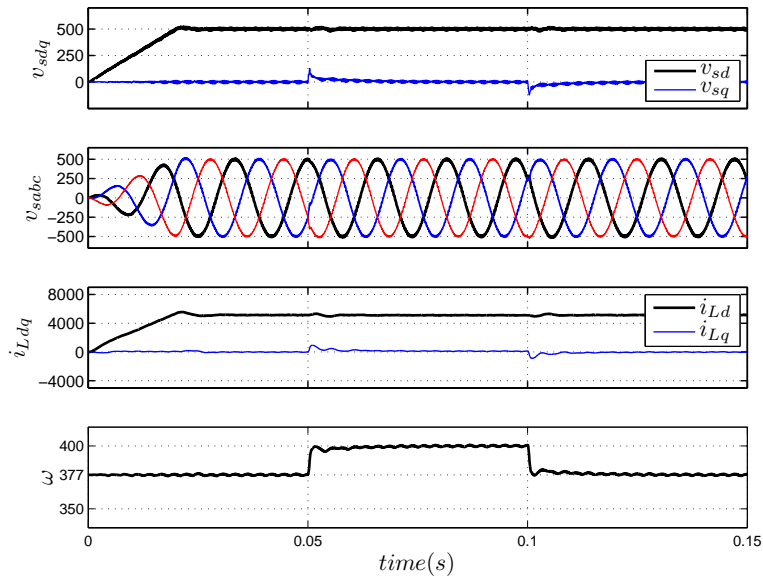


Figure 2.12: Frequency step responses of the islanded DER system under the fully-loaded condition.

in the voltage is due to the inrush current of the load RLC branch which takes place at $t = 0.1$ s. Nonetheless, the host-bus/load voltage retrieves its pre-disturbance form and quality in less than half 60-Hz cycle.

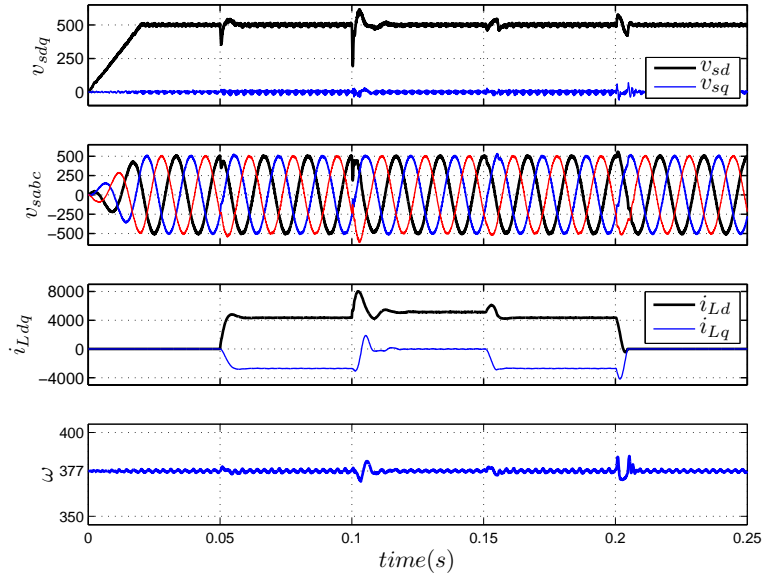


Figure 2.13: Response of the islanded DER system to sudden changes in the load configuration.

2.5.2 Induction Machine Load

This case study demonstrates the effectiveness of the proposed control strategy when a highly nonlinear load, being a two-pole induction machine, is energized by the DER system. Initially, the system is in a steady state while the induction machine is yet not connected to the host bus. In addition, the machine shaft speed (ω_r) and mechanical torque are both zero. At $t = 0.5$ s, the machine terminals are suddenly connected to the corresponding phases of the host bus, and the machine is energized; simultaneously, a mechanical torque of 0.7 pu is exerted on the machine shaft. Fig. 2.14 illustrates the response of the DER system and the machine.

Fig. 2.14 shows that subsequent to the switching incident, i_{Ld} , i_{Lq} , P_L , and Q_L exhibit large overshoots due to the machine inrush current. These overshoots, however, get damped in less than 0.17 s, as the machine speed increases. Despite the disturbance severity, v_{sd} , v_{sq} , and ω rapidly revert to their pre-disturbance values, and the system remains stable.

Fig. 2.15 shows the system response to a power-flow reversal followed by two frequency changes. The power flow is reversed by changing the external torque of the induction machine from 0.7 to -0.7 pu, at $t = 1.0$ s. Thus, P_L changes from about 600 kW to slightly higher than -600 kW; the discrepancy between the absolute values of P_L in the motoring and generating modes is due to the machine internal losses. A negative P_L can occur when other distributed

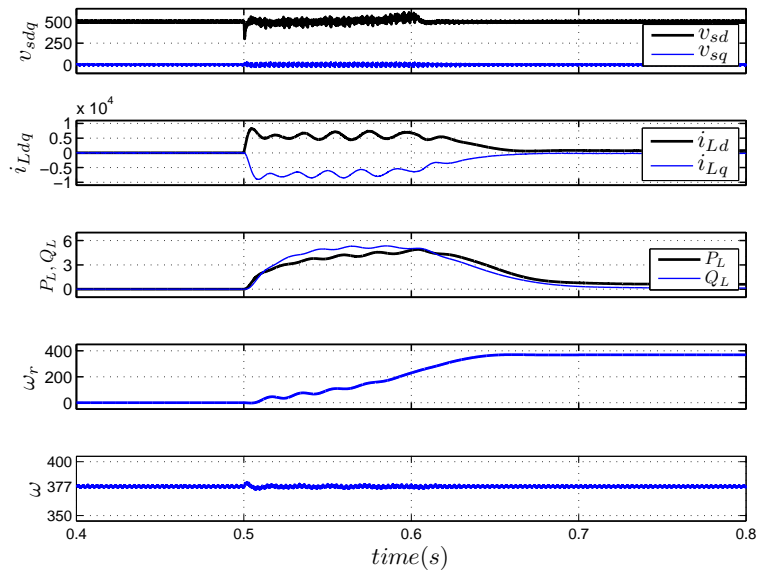


Figure 2.14: Response of the islanded DER system to sudden switching of the induction machine load.

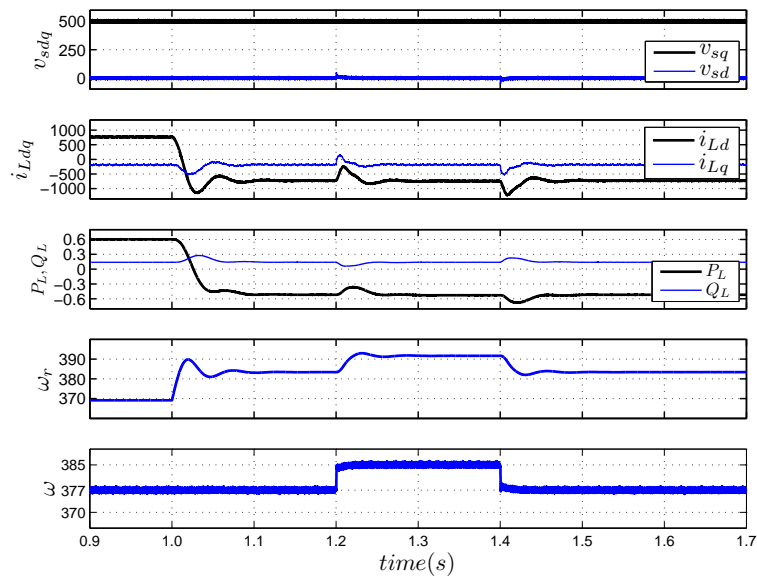


Figure 2.15: System behavior in response to a power flow reversal and step changes in the frequency setpoint.

generators, for example constant-speed wind turbines, are also connected to the islanded distribution network, and their aggregate power generation surpasses the total load. As Fig. 2.15 shows, the DER system maintains its stability under the power-flow reversal, and v_{sd} , v_{sq} , and ω remain tightly regulated.

At $t = 1.2$ s, ω_{ref} is stepped up from 377 to 385 rad/s; and it is brought back to 377 rad/s at $t = 1.4$ s. Consequently, the machine shaft speed increases over the foregoing period. However, the disturbances impose insignificant impacts on v_{sd} and v_{sq} , as Fig. 2.15 shows.

2.6 Conclusion

This chapter proposes a mathematical model and a voltage/frequency regulation strategy for an islanded, electronically-coupled, Distributed Energy Resource (DER). The proposed control strategy uses the circuit configuration, dq -frame current-control scheme, and the PLL mechanism that are typically employed in modern DER systems. It therefore requires minimal software modifications to enable the islanded mode operation of the DER system, for example, for a remote electrification application. The proposed control strategy takes advantage of suitable feedforward compensation techniques to mitigate the impacts of the load dynamics, inherent inter-couplings, and nonlinearities of the control system. This facilitates the controller design process. The system performance and control robustness/effectiveness under black-start operation, load switching incidents, and bi-directional power-flow conditions are demonstrated by means of simulations conducted on a detailed switched model of the system in the PSCAD/EMTDC software environment.

Chapter 3

Islanded-Mode DER Control for Distorted Load Currents

3.1 Introduction

In this chapter, the effect of unbalanced and nonlinear load conditions, as well as sudden and random load switching incidents on the terminal voltage of a DER system in islanded mode operation of a microgrid system is addressed. The lack of connection between an islanded microgrid system and the power system, fairly limited geographical span of an islanded distribution network, presence of single-phase loads, and random switching of loads of different steady-state/dynamic properties have made the islanded-mode control of DER systems a challenging task. Ideally, an islanded-mode control strategy for a DER system must:

1. ensure stable and fast response irrespective of loads configuration, dynamic properties, and sudden switchings;
2. provide the electronic converter of the DER system with adequate protection against output shorts and external faults;
3. accommodate unbalanced and harmonically-distorted output currents;
4. enable utilization of the same power circuit and control hardware as those commonly employed for grid-connected DER systems;

5. provide black-start capability; and
6. permit the incorporation of droop-based power sharing mechanisms to enable parallel operation with other DER systems, in a multi-system environment.

In this chapter, a control strategy is proposed based on a discrete-time model which is also valid for variable-frequency operation. Adopting the proposed control strategy, a DER system preserves the circuit and control structures that are typically employed and optimized for grid-connected DER systems. In addition, a combination of repetitive and deadbeat control strategies has been employed to accommodate unbalanced and/or harmonically-distorted output currents. Moreover, the control benefits from a feedforward compensation strategy that mitigates the impact of load dynamics on the voltage and frequency regulation processes. Thus, the load dynamics are masked and the DER system dynamic performance is made, to a great extent, independent of the load characteristics and circuit configuration. Under the proposed control, the DER system offers black-start capability, is robust to load switching incidents, and can be employed for decentralized frequency and voltage regulation in a multi-system islanded network. The chapter also illustrates the extension of the proposed islanded-mode control strategy to multi-system networks. The effectiveness of the proposed control strategy has been demonstrated through simulation studies conducted on a detailed switched model of the overall system, in the PSCAD/EMTDC environment.

3.2 Structure of the Islanded Network and DER System

Fig. 3.1 illustrates a simplified schematic diagram of the study islanded network. Up to Section 3.7, full concentration is placed on a single-system case. Thus, the network of Fig. 3.1 embeds one DER system that is connected to a feeder which energizes three sets of local loads; these are (i) a three-phase linear balanced load, (ii) a three-phase linear unbalanced load, and (iii) a three-phase rectifier load. The unbalanced load represents an aggregate of unequal single-phase loads which are connected between the phases and a neutral conductor. Each set of loads is interfaced with the feeder through a corresponding transformer. Each transformer has a solidly-grounded wye winding configuration at its low-voltage side. The feeder is linked to

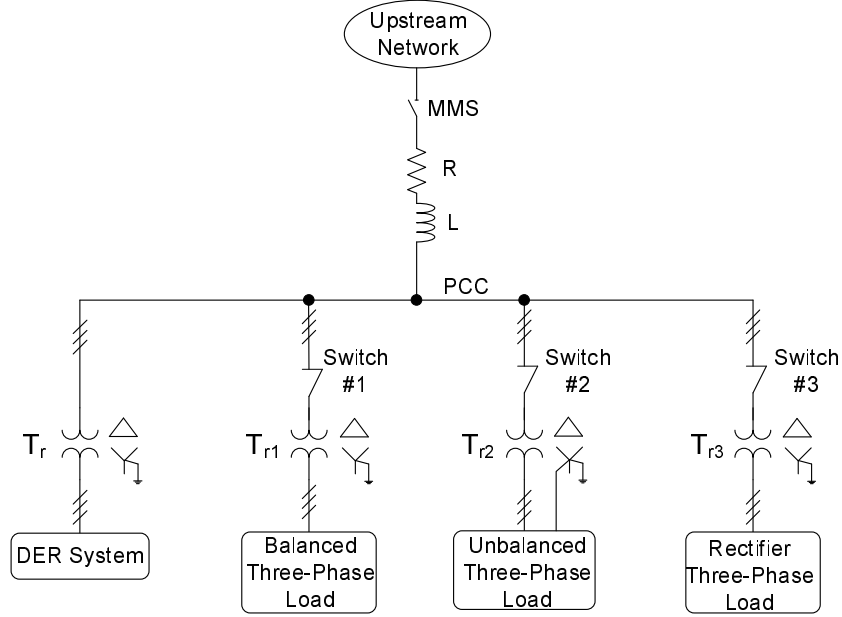


Figure 3.1: Single-line schematic diagram of the islanded network.

the upstream network via a series RL impedance and a switch denoted by the MMS. Thus, the DER system and the loads become isolated from the upstream network if the main switch breaks.

Fig. 3.2 illustrates that the power circuit of the DER system consists of a current-controlled VSC, a three-phase LC filter, and a three-phase circuit breaker. The per-phase inductance and capacitance of the filter are denoted by L and C_f , respectively. The resistance R models the ohmic loss of the filter inductor and also includes the effect of the on-state resistance of the VSC valves. The circuit breaker, Br, is controlled by the DER system synchronization scheme, and its function is to ensure that the DER system is connected to the network only if its terminal voltage is stable and in synchronism with the network voltage. The three-phase variables v_{abc} , v_{sabc} , i_{abc} , and i_{oabc} are referred, respectively, to as the *VSC ac-side terminal voltage*, *DER system terminal voltage*, *VSC ac-side current*, and *DER system output current*. The voltage at the low-voltage side of the interface transformer is labeled as v'_{sabc} and referred to as the *transformer voltage*. It is noted that the terminal voltage and the transformer voltage become identical when the circuit breaker Br is closed.

Fig. 3.2 also shows that the VSC dc side is paralleled with a dc-link capacitor, C_{dc} , and a voltage source. The voltage source represents the effect of either a dispatchable energy storage

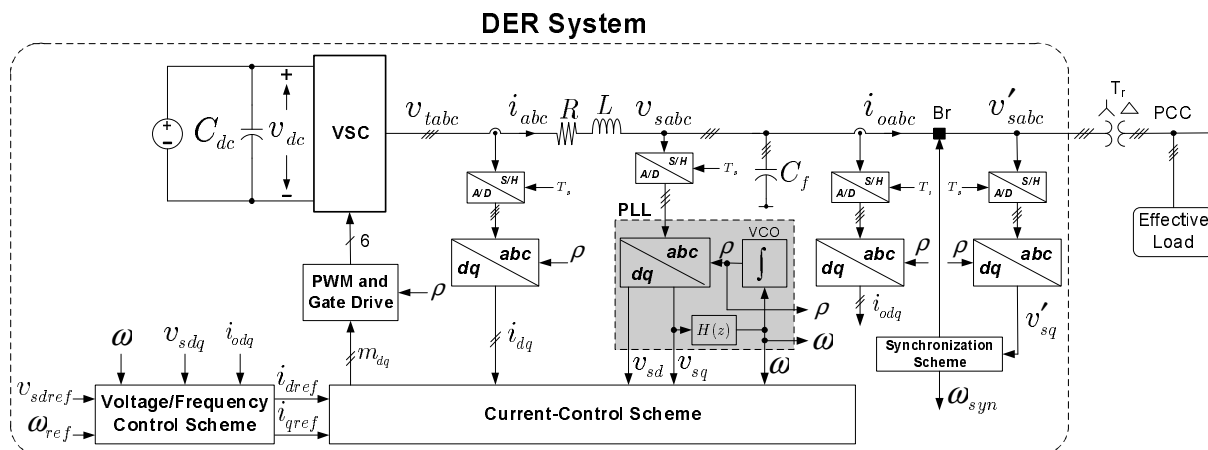


Figure 3.2: Schematic diagram of islanded DER system and loads.

device, e.g., a battery bank.

Fig. 3.2 also shows the control components of the DER system. It is noted that v_{tabc} , v_{sabc} , v'_{sabc} , i_{abc} , and i_{oabc} are sampled and digitized by the corresponding sample-and-hold (S/H) and analog-to-digital (A/D) converters. The discretized variables are then provided to the corresponding $abc - to - dq$ frame transformation blocks. Fig. 3.2 further shows that the DER system is controlled in a rotating dq frame whose d axis makes an angle, ρ , with respect to the stationary axis, i.e., the α axis. ρ is obtained from a PLL which also determines ω , i.e., the frequency of v_{sabc} . In the grid-connected mode of operation, v'_{sabc} and v_{sabc} are dominated by the power system, and ω represents the power system frequency. In the islanded mode, however, the main switch is open and the DER system of Fig. 3.2 solely supplies the loads. Thus, a control strategy is required to regulate the amplitude and frequency of the feeder (and thus the loads) voltage, under different load conditions.

3.3 Current-Control Scheme

A current-control scheme constitutes the kernel of the control scheme of the DER system of Fig. 3.2. The function of the current-control scheme is to regulate the d - and q -axis components of the VSC ac-side current, i.e., $i_{abc}(t)$, by means of the Pulse-Width Modulation (PWM) switching strategy. This section presents the structure and components of the current-control scheme.

In the continuous-time domain, the dynamic behavior of i_{abc} is described by the space-vector equation [23]:

$$L \frac{d\vec{i}}{dt} = -R\vec{i} + \vec{v}_t - \vec{v}_s, \quad (3.1)$$

where \vec{i} , \vec{v}_s , and \vec{v}_t are the space-vector representations of i_{abc} , v_{sabc} , and v_{tabc} , respectively. The VSC ac-side terminal voltage v_{tabc} is controlled by the PWM modulating signals of the VSC, i.e., $m_{abc}(t)$, based on $\vec{v}_t = (v_{dc}/2)\vec{m}$. Expressing each space vector in (3.1) in terms of its dq -frame components, based on $\vec{x}(t) = [x_d(t) + jx_q(t)]e^{j\rho(t)}$ (where \vec{x} is a generic representation of the space vector in question), one deduces

$$L \frac{d}{dt} [(i_d + ji_q)e^{j\rho}] = -R(i_d + ji_q)e^{j\rho} + \left[m_d \left(\frac{v_{dc}}{2} \right) + jm_q \left(\frac{v_{dc}}{2} \right) \right] e^{j\rho} - (v_{sd} + jv_{sq})e^{j\rho}, \quad (3.2)$$

which can be simplified to yield

$$L \frac{di_d}{dt} = -Ri_d + \underbrace{\left(L\omega i_q + m_d \frac{v_{dc}}{2} - v_{sd} \right)}_{\xi_d}, \quad (3.3)$$

$$L \frac{di_q}{dt} = -Ri_q + \underbrace{\left(-L\omega i_d + m_q \frac{v_{dc}}{2} - v_{sq} \right)}_{\xi_q}, \quad (3.4)$$

where the dummy control inputs ξ_d and ξ_q will be used to eliminate the couplings between i_d and i_q [38], and also the nonlinearity that would be introduced if ω is variable. ω is an output of the PLL and related to ρ , i.e., the other output of the PLL, as

$$\frac{d\rho}{dt} = \omega(t). \quad (3.5)$$

Taking ξ_d and ξ_q as the plant inputs, transforming (3.3) and (3.4) to discrete-time forms, one obtains

$$i_d(k+1) = ai_d(k) + b\xi_d(k), \quad (3.6)$$

$$i_q(k+1) = ai_q(k) + b\xi_q(k), \quad (3.7)$$

where the coefficients a and b are given by

$$a = e^{-\frac{RT_s}{L}}, \quad (3.8)$$

$$b = -\frac{1}{R} \left(e^{-\frac{RT_s}{L}} - 1 \right), \quad (3.9)$$

and T_s is the sampling period. It is noted that due to the definition of ξ_d and ξ_q , the sampled-data model represented by (3.6) and (3.7) is also valid for a scenario in which ω is variable.

It then follows from (3.3) and (3.4) that

$$\xi_d(k) = L\omega(k)i_q(k) + m_d(k)\frac{V_{dc}}{2} - v_{sd}(k), \quad (3.10)$$

$$\xi_q(k) = -L\omega(k)i_d(k) + m_q(k)\frac{V_{dc}}{2} - v_{sq}(k). \quad (3.11)$$

Equations (3.6)-(3.11) describe a sampled-data control plant whose block diagram is outlined by dashed lines in Fig. 3.3. For the control plant, $i_d(k)$ and $i_q(k)$ are the outputs, and $m_d(k)$ and $m_q(k)$ are the inputs. Fig. 3.3 also illustrates the controller part of the current-control scheme (outlined by solid lines), which processes the error signals $e_d(k) = i_{dref}(k) - i_d(k)$ and $e_q(k) = i_{qref}(k) - i_q(k)$, and delivers $m_d(k+1)$ and $m_q(k+1)$. These two last signals are then delayed by one sampling period to generate $m_d(k)$ and $m_q(k)$, which are required by the control plant. The delays are introduced deliberately and are necessary to permit completion of the calculations in a microprocessor-based implementation.

Fig. 3.3 further indicates that the controller constructs $m_d(k+1)$ and $m_q(k+1)$ in such a way that the effects of the signals $\omega(k)i_q(k)$ and $v_{sd}(k)$ on $i_d(k)$, and those of $\omega(k)i_d(k)$ and $v_{sq}(k)$ on $i_q(k)$, are counteracted. However, due to the intentional delay between each controller output and its corresponding plant input, the controller requires $\omega(k+1)i_q(k+1)$, $v_{sd}(k+1)$, $\omega(k+1)i_d(k+1)$, and $v_{sq}(k+1)$, in the k^{th} sampling period; each of the aforementioned variables can be estimated through a one-step-ahead prediction technique, using the sampled values in the $(k-1)^{th}$ and k^{th} sampling periods. The prediction is based on the assumption that the following linear relationship holds between the samples:

$$x(k+1) \simeq 2x(k) - x(k-1), \quad (3.12)$$

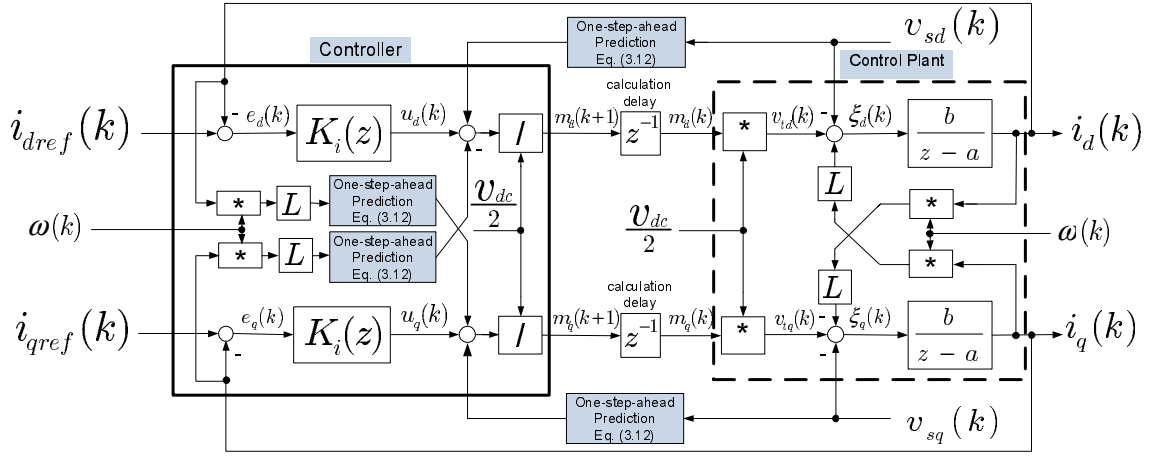


Figure 3.3: Block diagram of the current-control scheme of the DER system.

where $x(\cdot)$ is a generic representation of the signal to be predicted. It should be pointed out that a second-order prediction is also possible. However, the first-order prediction, based on (3.12), performs more satisfactorily in scenarios when sudden load changes occur [41].

Assuming that the predicted values are adequately accurate, the plant d - and q -axis dynamics are decoupled and the impacts of $v_{sd}(k)$ and $v_{sq}(k)$ on $i_d(k)$ and $i_q(k)$ are compensated. Therefore, the closed-loop system of Fig. 3.3 becomes equivalent to that of Fig. 3.4. As Fig. 3.4 indicates, the current-control scheme of Fig. 3.3 is effectively decomposed to two decoupled d - and q - axis current-control loops for which the respective control plants are $H_i(z) = b/[z(z - a)]$. Thus, the fastest possible closed-loop response is achieved if the closed-loop poles are placed at the origin of the z plane, through the following compensator:

$$K_i(z) = \frac{z(z - a)}{b(z^2 - 1)}. \quad (3.13)$$

Such a placement of poles is known in the literature as the deadbeat control strategy [41] and ensures that $i_d(k)$ and $i_q(k)$ track their corresponding reference values in two sampling periods, that is, $I_d(z)/I_{dref}(z) = I_q(z)/I_{qref}(z) = z^{-2}$.

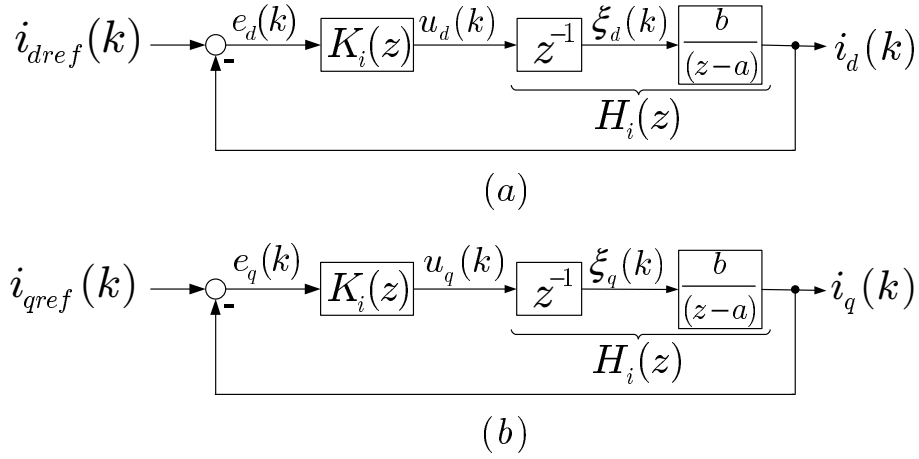


Figure 3.4: Block diagrams of two closed loops equivalent to the current-control scheme of Fig. 3.3.

3.4 Islanded Network Voltage and Frequency Regulation

In the islanded mode of operation, the network voltage and frequency regulation tasks boil down to the control of the DER system terminal voltage, $v_{sabc}(t)$. The following two subsections describe the two control tasks.

3.4.1 Amplitude Regulation Scheme

The objective of the amplitude regulation scheme is to control $v_{sd}(k)$ and $v_{sq}(k)$, i.e., the d - and q -axis components of the DER system terminal voltage, at their respective reference commands $v_{sdref}(k)$ and $v_{sqref}(k)$. This goal is, in turn, accomplished by the control of $i_{dref}(k)$ and $i_{qref}(k)$. As will be discussed in Section 3.4.2, $v_{sqref}(k)$ is indirectly employed in another control loop that regulates the frequency. The frequency regulation loop on the other hand forces v_{sq} to zero, in a steady state. Hence, the amplitude of the DER system terminal voltage, that is, $\sqrt{v_{sd}^2 + v_{sq}^2}$ is predominantly determined by v_{sd} ; the transient excursions of v_{sq} around zero do not significantly impact the amplitude and can be ignored. As such, v_{sdref} effectively serves as the set-point for the amplitude of the DER system terminal voltage. In a single-system, such as that of Fig. 3.1, v_{sdref} can be set to the (constant) network nominal voltage amplitude. However, in a multi-system v_{sdref} has to be flexible, for example, through a droop control mechanism, to enable the parallel operation of multiple DER systems. This latter option will be illustrated in

Section 3.7.

Dynamics of the DER system terminal voltage are described by the space-vector equation

$$C_f \frac{d\vec{v}_s}{dt} = \vec{i} - \vec{i}_o, \quad (3.14)$$

where \vec{i}_o is the space-vector equivalent of the output current, $i_{oabc}(t)$. Taking a similar procedure as the one followed to derive (3.6) to (3.11) from (3.1), one deduces

$$v_{sd}(k+1) = v_{sd}(k) + \frac{T_s}{C_f} \eta_d(k), \quad (3.15)$$

$$v_{sq}(k+1) = v_{sq}(k) + \frac{T_s}{C_f} \eta_q(k), \quad (3.16)$$

where

$$\eta_d(k) = i_d(k) - i_{od}(k) + C_f \omega(k) v_{sq}(k), \quad (3.17)$$

$$\eta_q(k) = i_q(k) - i_{oq}(k) - C_f \omega(k) v_{sd}(k). \quad (3.18)$$

Expressing (3.15) and (3.16) in transfer-function form results

$$\frac{V_{sd}(z)}{\eta_d(z)} = \frac{V_{sq}(z)}{\eta_q(z)} = \left(\frac{T_s}{C_f} \right) \frac{1}{z-1}. \quad (3.19)$$

Equations (3.17), (3.18), and (3.19) describe the control plant shown in the right side of Fig. 3.5. For the plant, $i_d(k)$ and $i_q(k)$ are the inputs, $v_{sd}(k)$ and $v_{sq}(k)$ are the outputs, and $i_{od}(k)$ and $i_{oq}(k)$ are the disturbance inputs. In turn, as Fig. 3.5 indicates, $i_d(k)$ and $i_q(k)$ are the responses of the d - and q -axis current-control loops of Fig. 3.4 to $i_{dref}(k)$ and $i_{qref}(k)$, respectively. The left side of Fig. 3.5 illustrates the controller part of the amplitude regulation scheme. It is noted that, measures of $i_{od}(k)$, $\omega(k)v_{sq}(k)$, $i_{oq}(k)$, and $\omega(k)v_{sd}(k)$ are employed as feedforward signals, to eliminate the impact of $i_{od}(k)$ and $i_{oq}(k)$ on $v_{sd}(k)$ and $v_{sq}(k)$, and also to mitigate the coupling between $v_{sd}(k)$ and $v_{sq}(k)$. However, due to the two-sampling-period delay between $i_{dref}(k)$ and $i_d(k)$, and between $i_{qref}(k)$ and $i_q(k)$, the feedforward compensation requires access to the signals $i_{od}(k+2)$, $\omega(k+2)v_{sq}(k+2)$, $i_{oq}(k+2)$, and $\omega(k+2)v_{sd}(k+2)$, in

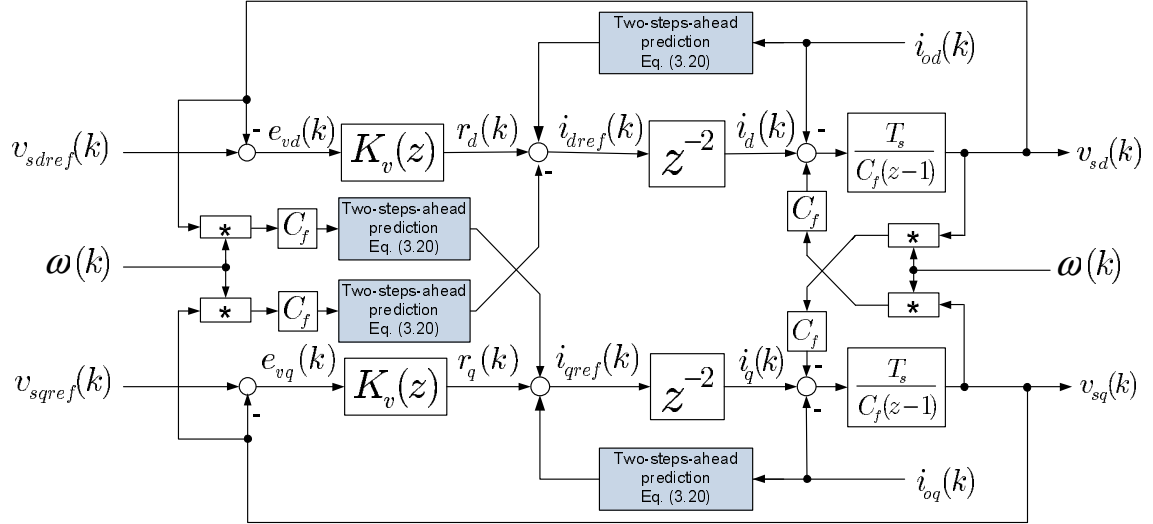


Figure 3.5: Block diagram of the amplitude regulation scheme of the DER system.

the k^{th} sampling period. Thus, an estimate of each of the aforementioned signals is constructed based on the signal samples in the $(k-1)^{\text{th}}$ and k^{th} sampling periods. The estimation is based on the assumption that the following linear relationship holds:

$$x(k+2) \simeq 3x(k) - 2x(k-1). \quad (3.20)$$

Assuming that the two-step-ahead prediction of (3.20) performs satisfactorily, the control scheme of Fig. 3.5 becomes equivalent to the two decoupled control loops shown in Fig. 3.6; in each loop, the effective control plant is $H_v(z) = T_s/[c_f z^2(z-1)]$. In Fig. 3.6, $K_v(z)$ is the transfer function of each of the d - and q -axis compensators, respectively, processing the error signals $e_{vd}(k) = v_{sdref}(k) - v_{sd}(k)$ and $e_{vq}(k) = v_{sqref}(k) - v_{sq}(k)$. In their simplest forms, these compensators can be of the PI type; this, however, results in deterioration of the control system performance under unbalanced and/or harmonically-distorted output current conditions, as will be discussed in Section 3.5.

3.4.2 Frequency Regulation Scheme

The objective of the frequency regulation scheme is to regulate the frequency of $v_{sabc}(t)$, and thus the frequency of the islanded network, at the reference command ω_{ref} . As Fig. 3.2 shows,

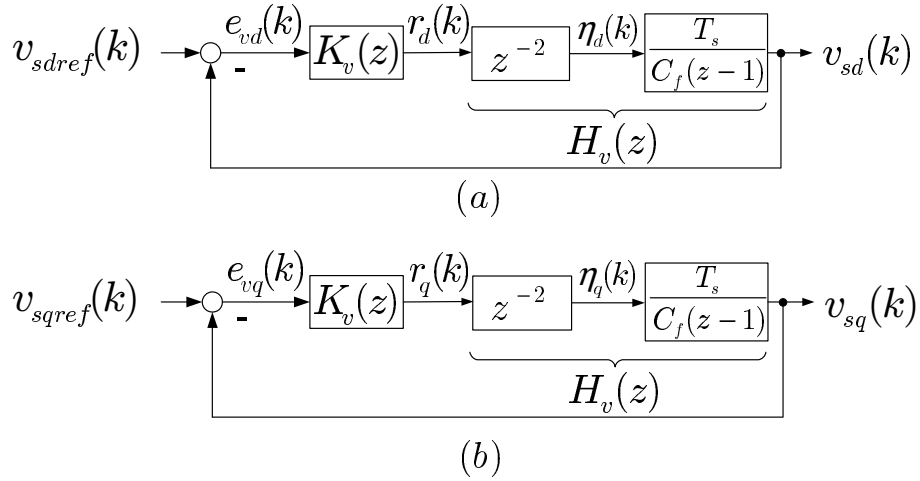


Figure 3.6: Block diagrams of the d - and q -axis closed loops equivalent to the amplitude regulation scheme of Fig. 3.5.

a PLL processes $v_{sq}(k)$ through the filter $H(z)$, and $\omega(k)$ is determined in such a way that $v_{sq}(k)$ is forced to zero [37]. In the grid-connected mode the frequency of $v_{sabc}(t)$, i.e., $\omega(k)$, is imposed by the grid and becomes equal to the power system angular frequency. However, in the islanded mode of operation, $\omega(k)$ must be regulated by $v_{sq}(k)$ through the control of $v_{sqref}(k)$.

As Fig. 3.2 indicates, the PLL affects the frequency $\omega(k)$ based on

$$\Omega(z) = H(z)V_{sq}(z), \quad (3.21)$$

where $H(z)$ is a filter of the form:

$$H(z) = \frac{k_p}{z-1}, \quad (3.22)$$

where k_p is the filter gain. Thus, a control loop, Fig. 3.7, can be formed based on (3.21) to regulate $\omega(k)$. As Fig. 3.7 shows, a compensator, i.e., $K_\omega(z)$, processes the error $e_\omega(k) = \omega_{ref}(k) - \omega(k)$ and determines $v_{sqref}(k)$ which is then tracked by $v_{sq}(k)$ through the action of the q -axis amplitude regulation loop of Fig. 3.6(b), and $\omega(k)$ is controlled. Due to the pole of $H(z)$ at $z = 1$, $v_{sq}(k)$ settles at zero in the steady state, so does $v_{sqref}(k)$. Therefore, $K_\omega(z)$ can be

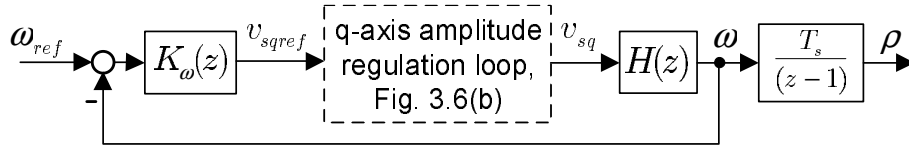


Figure 3.7: Block diagram of the frequency regulation loop.

as simple as a pure gain to ensure that $\omega(k)$ tracks $\omega_{ref}(k)$ with zero steady-state error. Thus,

$$K_{\omega}(z) = k_{\omega} , \quad (3.23)$$

where k_{ω} is the compensator gain.

3.5 Repetitive-Control-Based Compensator for Amplitude Regulation Scheme

3.5.1 Fundamentals

The use of traditional PI compensators in the amplitude regulation scheme of Fig. 3.6, i.e., for $K_v(z)$, can guarantee an adequately fast and stable closed-loop response if the output current is balanced. However, unbalanced loads cause second-order harmonic components that appear in $i_{od}(k)$ and $i_{oq}(k)$, and distort $v_{sd}(k)$ and $v_{sq}(k)$. For nonlinear loads, $i_{od}(k)$ and $i_{oq}(k)$ are even more distorted, and so are $v_{sd}(k)$ and $v_{sq}(k)$, due to higher-order harmonic components. Consequently, the effectiveness of the amplitude and frequency regulation schemes, i.e., Figs. 3.5 to 3.7, is compromised to a large extent. This calls for a more elaborate compensator structure for $K_v(z)$. In what follows, a repetitive-control-based compensator structure is introduced to address this shortcoming.

Repetitive control is an effective strategy for rejection of periodic disturbance inputs. It is based on the internal model principle, [42], which implies that the inclusion of unstable dynamic modes of the reference command or the disturbance input in a control loop ensures perfect tracking of the former or complete rejection of the latter. To better appreciate this, let us consider a hypothetical compensator of the structure shown in Fig. 3.8 where $e_{vd}(t)$ and $r_d(t)$ are the error and the compensator output, respectively. The transfer function of this compensator

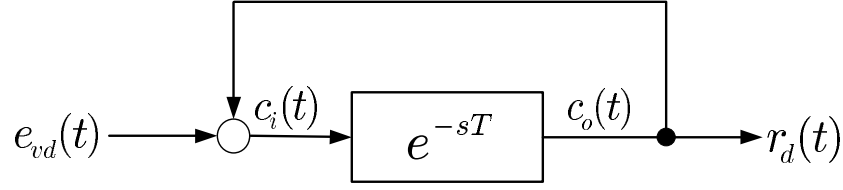


Figure 3.8: Block diagram of a hypothetical compensator based on the internal model principle to reject a periodic disturbance input.

is

$$K_v(s) = \frac{R_d(s)}{E_{vd}(s)} = \frac{e^{-sT}}{1 - e^{-sT}}, \quad (3.24)$$

where T is the period of the disturbance input. Equation (3.24) indicates that the employment of the compensator $K_v(s)$ in a negative feedback loop results in the infinity magnitude for the loop-gain at frequencies $\omega = 2\pi h/T$ (h is an integer), i.e., the fundamental and harmonic frequencies of the disturbance input, and therefore eliminates the steady-state error. Considering a discrete-time implementation and $z = e^{sT_s}$, (3.24) can be rewritten as

$$K_v(z = e^{sT_s}) = \frac{R_d(z)}{E_{vd}(z)} = \frac{z^{-D}}{1 - z^{-D}}, \quad (3.25)$$

where $D = T/T_s$ is the ratio of the disturbance input period to the sampling period. If T is an integer multiple of T_s , that is, D is an integer number, say, N , then z^{-D} corresponds to an N -step delay operation on the signal $c_i(k)$. Hence, the compensator of Fig. 3.8 can be digitally implemented by means of an array of N First-In-First-Out (FIFO) memory cells, as shown in Fig. 3.9 [43]. From a design standpoint, this also means that if the frequency of the disturbance input is constant and known, the sampling period may be chosen as an integer sub-multiple of the disturbance input period, such that D is an integer. However, the discrete-time implementation is not straightforward if D is a non-integer, for example, in variable-frequency scenarios; a solution is presented in Section 3.5.2.

A practical repetitive-control-based compensator is an extension of the kernel structure of Fig. 3.9. The outlined part of the closed-loop system of Fig. 3.10 illustrates such an extension for $K_v(z)$ in the d -axis amplitude regulation loop (of Fig. 3.6(a)). In the repetitive-control-based

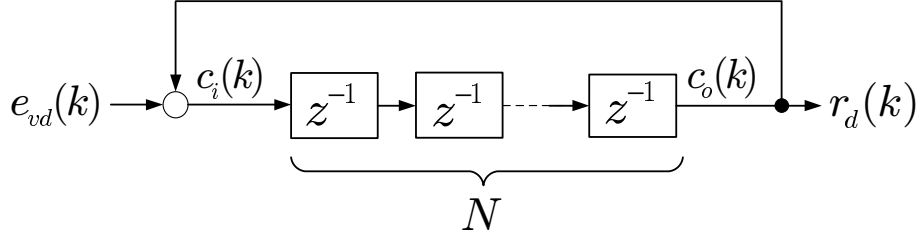


Figure 3.9: Block diagram of the discrete-time realization of the compensator of Fig. 3.8 if the disturbance input frequency is an integer sub-multiple of the sampling frequency.

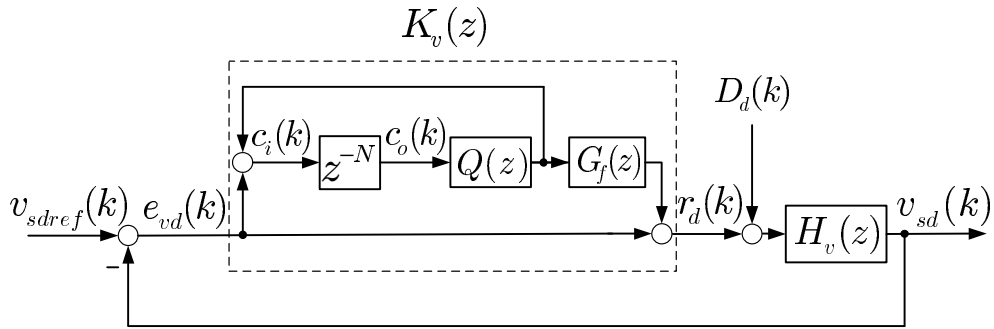


Figure 3.10: Block diagram of the proposed repetitive-control-based compensator incorporated in the d -axis amplitude regulation loop of Fig. 3.6(a).

$K_v(z)$, the filters $Q(z)$ and $G_f(z)$ are included for stabilization of the closed-loop system. $Q(z)$ also enables the discrete-time implementation of the function e^{-sT} (see (3.24), and Fig. 3.8), in the general case where T is not an integer multiple of T_s .

In the closed-loop system of Fig. 3.10, $H_v(z)$ is the effective plant model which also appeared in the closed-loop scheme of Fig. 3.6. The (harmonically-distorted) disturbance input $D_d(k)$ manifests itself if the output current is unbalanced and/or distorted. The main reason for the existence of $D_d(k)$ is the deterioration of the effectiveness of the feedforward compensations employed in the current-control and amplitude regulation schemes, due mainly to inaccuracies of (3.12) and (3.20). Fig. 3.10 only shows the d -axis control loop; the q -axis loop components are the same as their d -axis counterparts and therefore do not receive a separate treatment.

3.5.2 Extension to Variable-Frequency Systems

If the frequency of the islanded network is to be varied by the DER system(s), for example through a droop mechanism (see Section 3.7), the frequency of the disturbance input $D_d(k)$ is also subject to variations. Thus, the ratio of the disturbance input period to the pre-specified sampling period does not necessarily remain an integer. This complicates the straightforward discrete-time implementation of the compensator, shown in Fig. 3.9. To resolve this issue, as shown in Fig. 3.10, the filter $Q(z)$ in $K_v(z)$ is cascaded with the N -step delay function, such that $Q(z)z^{-N}$ exhibits a frequency response adequately similar to that of e^{-sDT_s} . This, in general, requires that $Q(z)$ be a fractional delay filter which can be realized based on a variety of techniques [44]. In this chapter, $Q(z)$ is chosen as a Finite Impulse Response (FIR) filter for its potential accuracy and ease of implementation.

To simplify the subsequent analysis, let us consider an equivalent problem in which $Q(z)$ is to approximate $e^{-sD'T_s}$, where $D' = D - N$ is the delay that needs to be introduced by $Q(z)$. Let also $Q(z)$ be of the following form

$$Q(z) = a_0 + a_1z^{-1} + a_2z^{-2} + \dots + a_Mz^{-M}, \quad (3.26)$$

where the integer M represents the filter order. Then, the coefficients a_0, a_1, \dots, a_M can be determined through minimization of the frequency-domain error between $Q(z)$ and $e^{-sD'T_s}$ which is formulated as [44]:

$$E(e^{j\Omega}) = \left(\sum_{m=0}^M a_m e^{-jm\Omega} \right) - e^{-jD'\Omega}, \quad (3.27)$$

where $\Omega = \omega T_s$ is the normalized angular frequency. Moreover, if $E(e^{j\Omega})$ is made maximally-flat at $\Omega = 0$, i.e., its derivatives are all zero at $\Omega = 0$, then $Q(z)$ faithfully approximates $e^{-sD'T_s}$ at low frequencies, but it exhibits a high-frequency roll-off; this property is desirable since modeling errors typically manifest themselves at high frequencies.

$E(e^{j\Omega})$ is made maximally-flat at $\Omega = 0$ if

$$\frac{d^l E(e^{j\Omega})}{d\Omega^l} \Big|_{\Omega=0} = 0 \quad l = 0, 1, 2, \dots, M. \quad (3.28)$$

Equation (3.28) is equivalent to the following set of $M + 1$ linear equations:

$$\sum_{m=0}^M m^l a_m = (D')^l \quad l = 0, 1, 2, \dots, M. \quad (3.29)$$

Finally, the solution to (3.29), i.e., the coefficients of $Q(z)$, is given by the classical Lagrange interpolation formula, [45], as

$$a_m = \prod_{l=0, l \neq m}^M \frac{D' - l}{m - l} \quad m = 0, 1, 2, \dots, M. \quad (3.30)$$

It should be noted that there is a trade-off between the order of $Q(z)$ and its effectiveness in approximating the frequency response of $e^{-sD'T_s}$. $Q(z)$ is picked as a 9th-order filter, i.e., $M = 9$. This corresponds to a delay, D' , whose integer part is 4. Thus,

$$D' = 4 + d, \quad (3.31)$$

where $d < 1$ is the non-integer component of D' . As Fig. 3.10 indicates, the effective delay introduced by $Q(z)z^{-N}$ is $D = N + D' = N + 4 + d$. Defining

$$D = \frac{2\pi f_s}{\omega_{ref}}, \quad (3.32)$$

one deduces

$$N = \text{int}(D) - 4, \quad (3.33)$$

and

$$D' = 4 + \underbrace{D - \text{int}(D)}_d, \quad (3.34)$$

where $\text{int}(\cdot)$ denotes the “integer part of”. D' is used to determine the parameters of $Q(z)$, based on (3.30).

Fig. 3.11 illustrates the frequency response of the designed $Q(z)$, indicating that the filter

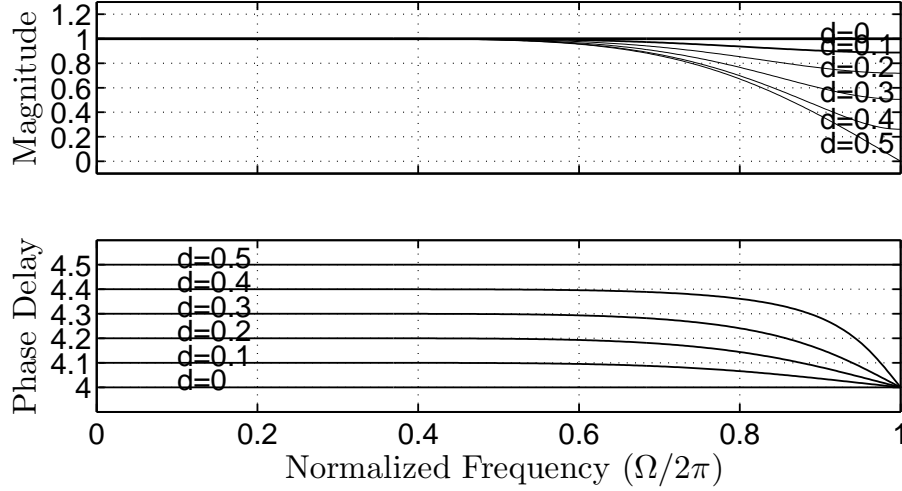


Figure 3.11: Frequency response of the FIR fractional delay filter $Q(z)$.

approximates $e^{-sD'T_s}$ with a reasonable fidelity, up to about $\Omega = 3\pi/2$ rad.

3.5.3 Closed-Loop Stability

The stability of a repetitive-control-based feedback loop is extensively discussed in the technical literature, [46]- [48]. In particular, [48] deals with the stability problem through the “regeneration spectrum”, defined as

$$R(\omega) = \left. \frac{C_i(z)}{C_o(z)} \right|_{z=e^{j\omega T_s}}, \quad (3.35)$$

where $C_i(z)/C_o(z)$ is calculated when z^{-N} is taken out of the control scheme of Fig. 3.10, and the reference command and the disturbance input are set to zero. As discussed in [48], the closed-loop system is stable if

- the filters $Q(z)$ and $G_f(z)$ are stable;
- the transfer function $H_v(z)/(1 + H_v(z))$ is stable; and
- $R(\omega)$ is less than unity at all frequencies.

Let us assume that the first aforementioned stability requirement is met. Also, one can readily verify that $H_v(z)/(1 + H_v(z))$ is stable for the system of Fig 3.10. To assess the third stability

requirement, $C_i(z)/C_o(z)$ is calculated for the feedback loop of Fig 3.10 as

$$\frac{C_i(z)}{C_o(z)} = Q(z) \left(1 - G_f(z) \frac{H_v(z)}{1 + H_v(z)} \right). \quad (3.36)$$

Thus, to guarantee the closed-loop stability, one must ensure

$$R(\omega) = \left| Q(z) \left(1 - G_f(z) \frac{H_v(z)}{1 + H_v(z)} \right) \right|_{z=e^{j\omega T_s}} < 1. \quad (3.37)$$

One can prove that the constraint (3.37) is satisfied if $G_f(z) = z^3$ (which is a stable filter) and $|Q(e^{j\omega T_s})| < 1$. It can also be verified that the FIR fractional delay filter $Q(z)$, selected as discussed in Section 3.5.2, satisfies the condition $|Q(e^{j\omega T_s})| < 1$.

3.6 Study Cases and Simulation Results

To demonstrate the effectiveness of the proposed control strategy, a detailed switched model of the system of Fig. 3.1 has been simulated in the PSCAD/EMTDC software environment [40]; the simulation time step is $6.7096 \mu\text{s}$. The parameters of the loads and system are given in Appendix B.

In the case studies, the system is black-started with $v_{sdref} = 0$ and $\omega_{ref} = 377$ rad/s, while only the balanced load is connected, i.e., only Switch #1 is closed. Subsequently, v_{sdref} is ramped up to 450 V and kept constant from $t = 0.02$ s onwards. At $t = 0.5$ s, the balanced load is switched off while either the unbalanced load or the rectifier load is switched on, depending on the case study. At $t = 1.0$ s, v_{sdref} is changed stepwise from 450 V to 550 V. At $t = 1.5$ s, ω_{dref} is subjected to a step change from 377 rad/s to 400 rad/s. It should be noted that, with respect to the sampling frequency of $f_s = 6480$ Hz, while $\omega = 377$ rad/s corresponds to $D = 108$ (see Section 3.5.2, equation (3.32)), $\omega = 400$ rad/s results in the non-integer value 101.78 for D .

In the graphs, the voltages are expressed in V, currents in A, and frequencies in rad/s.

3.6.1 Response to Output Current Imbalance

This case study demonstrates the system response to the sequence of events described in Section 3.6 and when the unbalanced load replaces the balanced load, at $t = 0.5$ s. Figs. 3.12 and 3.13 illustrate the system response when $K_v(z)$ is a PI compensator with the transfer function $K_v(z) = 0.9(z - 0.95)(z - 1)^{-1}$ [Ω^{-1}]. The system response under the repetitive-control-based compensator is illustrated in Figs. 3.14 and 3.15.

Figs. 3.12(a) and (b) show that for both the balanced and unbalanced loads, the voltage and frequency track their respective reference commands with stable and fast responses, although due to the unbalanced load switching, from $t = 0.5$ s on they are superimposed by ripples.

Fig. 3.12(c) illustrates the ratio of the negative-sequence to the positive-sequence components of the output current, i.e., i_{on}/i_{op} . It is observed that, after $t = 0.5$ s the ratio i_{on}/i_{op} increases to about 94%, which corresponds to a highly unbalanced load whose imbalance degree is only a few percent lower than the maximum possible value, i.e., unity. The discrepancy is due to the (balanced) magnetization current of the interface transformer Tr. Thus, the negative-sequence component of the output current manifests itself as second-order harmonics in i_{od} and i_{oq} . The harmonic components are not rejected and result in severe distortions in v_{sd} , v_{sq} , and ω , after $t = 0.5$ s, as Figs. 3.12(a) and (b) indicate. Consequently, as Fig. 3.12(d) indicates, v_{sabc} develops an appreciable negative-sequence component of 18% of its positive-sequence component, once the output current becomes unbalanced. Fig. 3.13 provides a zoomed view of Fig. 3.12, over a period around $t = 0.5$ s, illustrating the waveforms of the output current, the DER system terminal voltage, and the PCC voltage, subsequent to the energization of the unbalanced load. Fig. 3.13(b) shows that, although the closed-loop control system has mitigated to some extent the impact of load current imbalance, the DER system terminal voltage is remarkably unbalanced. Fig. 3.13(c) indicates that the PCC voltage imbalance is more severe than that in v_{sabc} . The reason is the leakage reactance of the interface transformer Tr.

Figs. 3.14 and 3.15 illustrate the system response to the same sequence of events as in Figs. 3.12 and 3.13, however, using the proposed repetitive-control-based compensator for $K_v(z)$. Figs. 3.14(a) and (b) show that, unlike the PI compensator case, v_{sd} , v_{sq} , and ω are of considerably lower distortions. Fig. 3.14(d) indicates that the ratio of the negative-sequence to

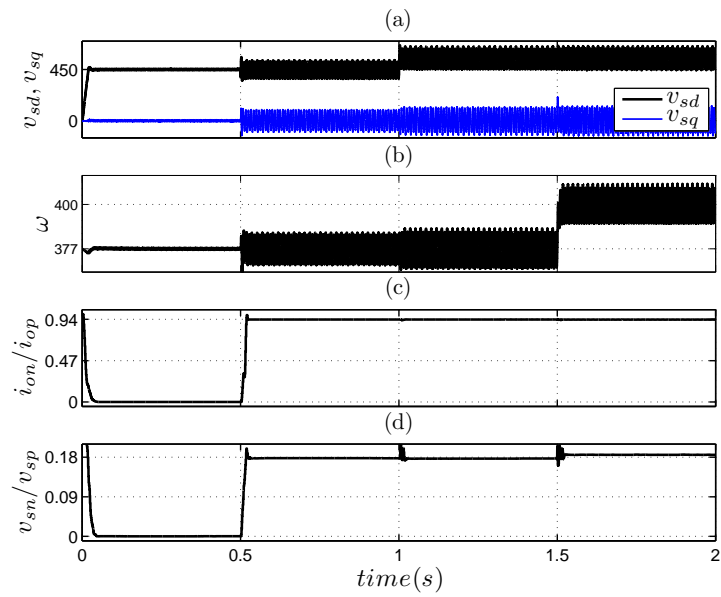


Figure 3.12: Overall system response to switching from a balanced load to an unbalanced load when PI compensators are employed.

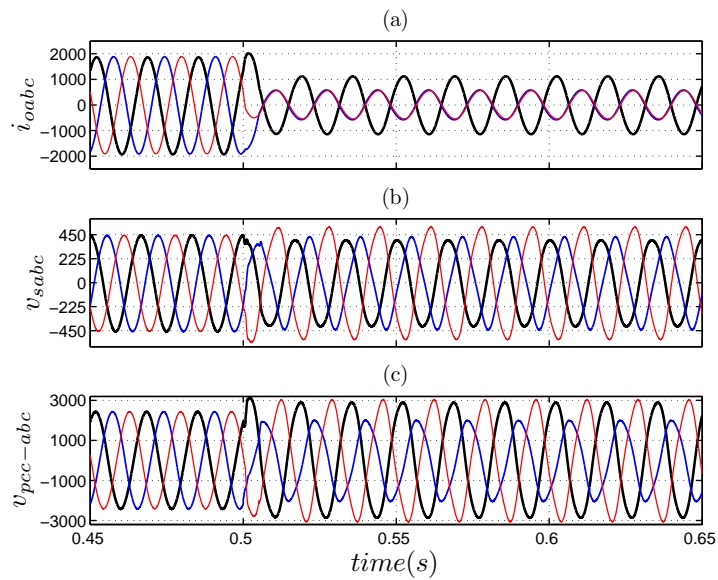


Figure 3.13: Zoomed view of (a) i_{oabc} , (b) v_{sabc} , and (c) PCC voltage, under unbalanced output current and PI compensators.

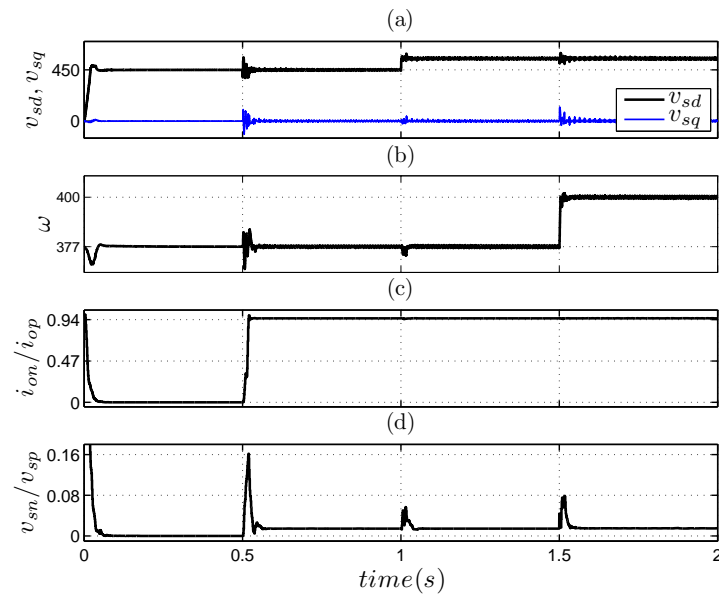


Figure 3.14: Overall system response to switching from a balanced load to an unbalanced load, when repetitive-control-based compensators are employed.

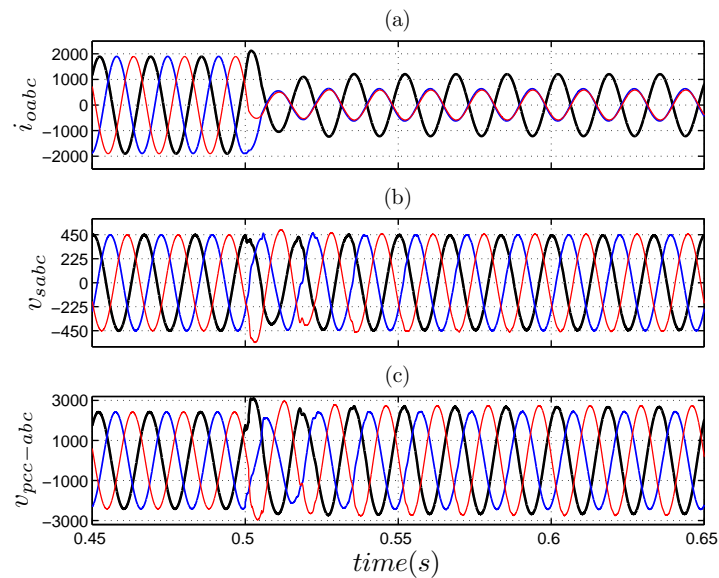


Figure 3.15: Zoomed view of (a) i_{oabc} , (b) v_{sabc} , and (c) PCC voltage, under unbalanced output current and repetitive-control-based compensators.

the positive-sequence components of v_{sabc} is restricted to the steady-state value of about 1.5%, which indicates a 12-time improvement as compared to the system with the PI compensator, for the same output current imbalance (Fig. 3.14(c)). Fig. 3.15 shows a zoomed view of the waveforms of i_{oabc} , v_{sabc} , and $v_{pcc-abc}$, for a period about $t = 0.5$ s. Fig. 3.15(b) shows that the proposed repetitive-control-based compensator almost completely eliminates the imbalance of v_{sabc} , in about four 60-Hz cycles. Fig. 3.15(c) indicates that the PCC voltage still exhibits some imbalance due to the leakage reactance of Tr. However, the imbalance is significantly smaller than the one observed in the PI compensator case, i.e., Fig. 3.13(c).

It should be pointed out that in a grid-connected network, typically the voltage imbalance of a three-phase service is less than 3% [49], while it should not exceed 2% for some more sensitive equipment [50] [51]. Thus, the proposed repetitive-control-based compensator has provided a degree of voltage stiffness for an islanded network that is comparable to those offered by traditional grid-connected networks.

3.6.2 Response to Output Current Distortion

In this case study, the balanced load is switched to the rectifier load, at $t = 0.5$ s. Otherwise, the sequence of events is the same as those explained in Section 3.6.

Figs. 3.16 and 3.17 illustrate the system response when $K_v(z)$ is of the PI type. Figs. 3.16(a) and (b) indicate that v_{sd} , v_{sq} , and ω become distorted subsequent to the energization of the rectifier load, although the responses of the average values of the aforementioned variables to their respective commands is still stable and fast. Figs. 3.16(c) and (d) show that, subsequent to the rectifier load energization, the Total Harmonic Distortion (THD) of the i_{oabc} and v_{sabc} increase from zero to about 13%. The distortion of v_{sabc} , in turn, results in the distortion of ω shown in Fig. 3.16(b). Fig. 3.17 provides a close-up of the waveforms of i_{oabc} , v_{sabc} , and $v_{pcc-abc}$, for a period about $t = 0.5$ s; it is observed that the waveforms develop substantial harmonic distortions once the rectifier load is switched on. It is apparent from this case that PI compensators have insignificant effectiveness in mitigation of the voltage distortion.

Figs. 3.18 and 3.19 illustrate the system response to the same sequence of events as in Figs. 3.16 and 3.17, however, with the proposed repetitive-control-based compensator in effect. It is

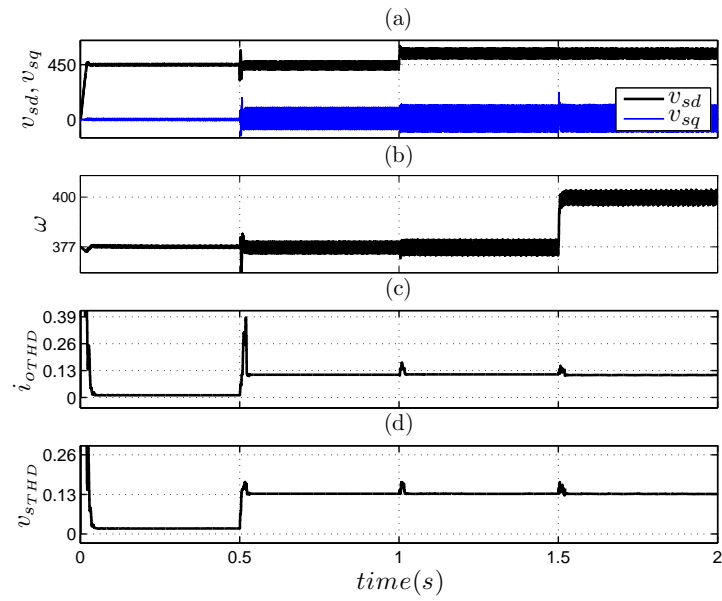


Figure 3.16: Overall system response to switching from a balanced load to a rectifier load, when PI compensators are employed.

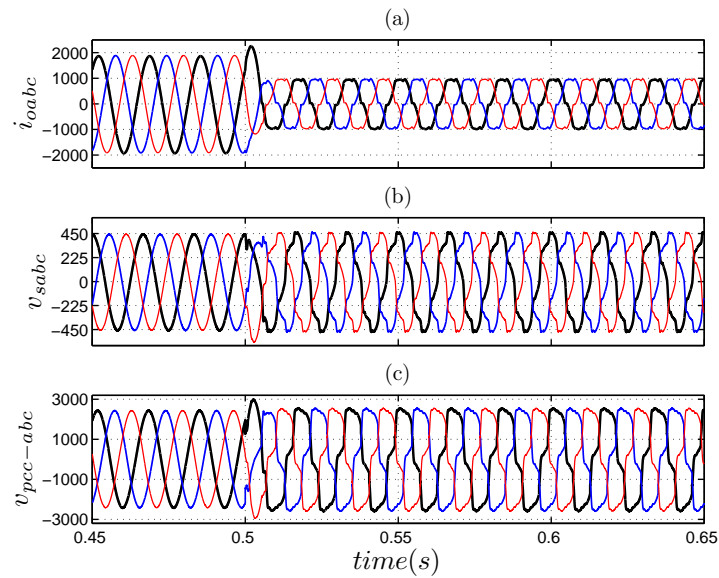


Figure 3.17: Zoomed view of (a) i_{oabc} , (b) v_{sabc} , and (c) PCC voltage, under distorted output current and PI compensators.

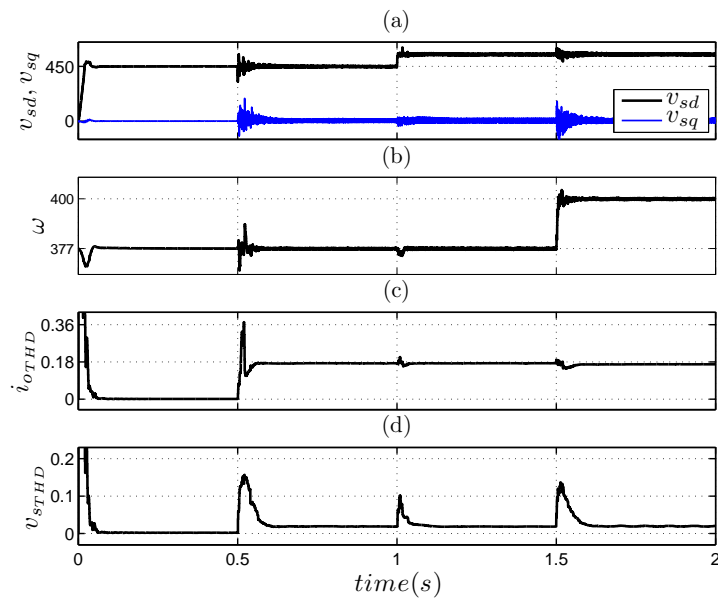


Figure 3.18: Overall system response to switching from a balanced load to a rectifier load, when repetitive-control-based compensators are employed.

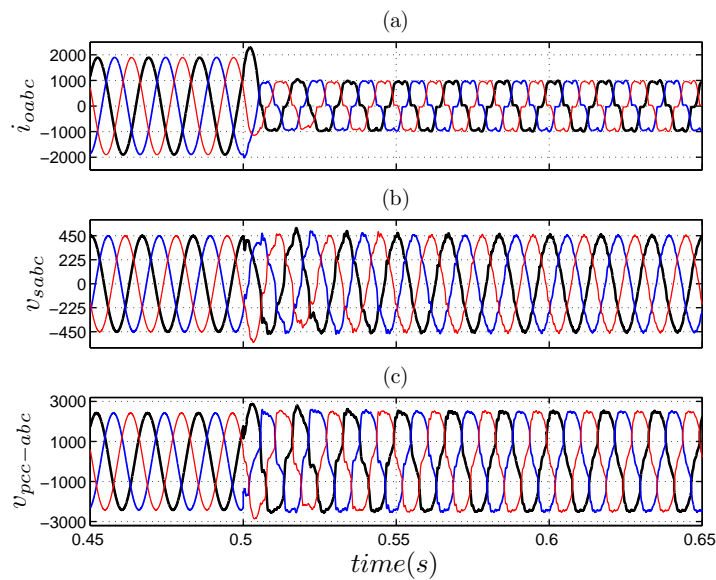


Figure 3.19: Zoomed view of (a) i_{abc} , (b) v_{sabc} , and (c) PCC voltage, under distorted output current and repetitive-control-based compensators.

observed from Figs. 3.18(a) and (b) that v_{sd} , v_{sq} , and ω remain distortion-free in spite of the harmonic distortion of i_{oabc} . Thus, the THD of v_{sabc} reduces to about 1.8% in the steady state [Fig. 3.18(c)]; these improvements can be better seen in the zoomed waveforms of Fig. 3.19, while it is remembered that due to the leakage reactance of Tr some distortion is inevitable for $v_{pcc-abc}$ [Fig. 3.19(c)]. The distortion is, however, considerably lower than that shown in 3.17(c) for the PI compensator case.

It is interesting to note that, compared to the response under a PI compensator, i.e., Fig. 3.16(a), the system response under the repetitive-control-based compensator exhibits a longer settling time subsequent to the switching of the balanced load to the rectifier load, at $t = 0.5$ s [Fig. 3.18(a)]. This can be explained based on the fact that the poles of $K_v(z)$ appear as the zeros of the transfer function from the disturbance input to the output, Fig. 3.10. The existence of so many zeros in a repetitive-control-based compensator results in a naturally more complex transient response to a disturbance input, typically taking longer to settle.

3.7 Extension to Multi-System Networks

As pointed out in the introduction, an islanded-mode control strategy must also enable operation in a multi-system environment. The control strategy proposed in this chapter ensures tight and fast regulation over both the frequency and the magnitude of the DER system terminal voltage. Therefore, the classical approaches of *frequency versus real-power droop* and *voltage versus reactive-power droop* can be directly employed for co-operation of multiple DER systems, in a multi-system network. This is shown in Fig. 3.20 for an example two-system network.

3.7.1 Power Sharing and Decentralized Frequency Control

As Fig. 3.20 indicates, in a multi-system application the set-points ω_{ref} and v_{sdref} of each DER system are drooped, respectively, against the real power and the reactive power which leave the DER system. These power components are calculated from the output current and the DER system terminal voltage, using $S = (3/2)\vec{v}_s\vec{i}_o^*$ (S is the instantaneous complex power). Since the output power components are distorted due to output current imbalance and/or dis-

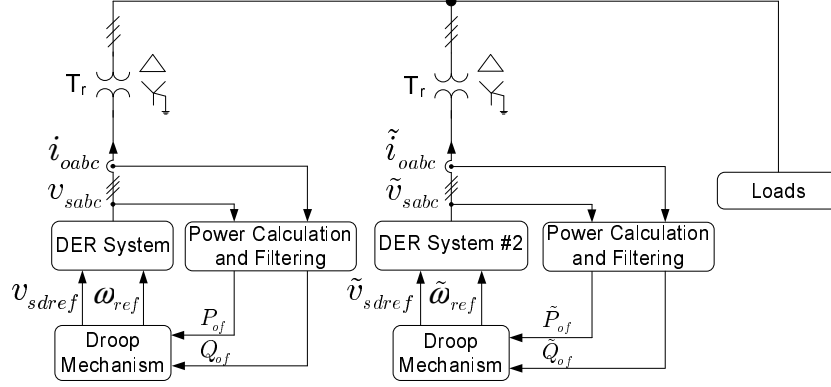


Figure 3.20: An example two-system network illustrating the application of the proposed islanded-mode control strategy in a multi-system microgrid.

tortion, their calculated values are low-pass filtered to determine the set-points for frequency and magnitude. Thus, ω_{ref} is determined as

$$\omega_{ref}(k) = \omega_0 - mP_{of}(k) + \omega_{syn}(k), \quad (3.38)$$

where ω_0 is the nominal network frequency, $P_{of}(k)$ is the filtered value of the output real power, and m is the real-power droop coefficient. ω_{syn} is a controllable component of ω_{ref} that is used to synchronize the DER system terminal voltage to the transformer voltage. The synchronization scheme and the way ω_{syn} is generated are explained in Section 3.7.2.

$P_{of}(k)$ is calculated as

$$P_{of}(k) = \alpha P_{of}(k-1) + (1-\alpha) \underbrace{\left(\frac{3}{2} \right) [v_{sd}(k-1)i_{od}(k-1) + v_{sq}(k-1)i_{oq}(k-1)]}_{Re\{(3/2)\vec{v}_s^* \vec{i}_o^*\}}, \quad (3.39)$$

where α is the low-pass filter pole, and $Re\{\cdot\}$ denotes the real part. Similarly, v_{sdref} is determined as

$$v_{sdref}(k) = V_0 - nQ_{of}(k), \quad (3.40)$$

where V_0 is the nominal network voltage magnitude, $Q_{of}(k)$ is the filtered value of the output

reactive power, and n is the reactive-power droop coefficient. $Q_{of}(k)$ is calculated as

$$Q_{of}(k) = \alpha Q_{of}(k-1) + (1-\alpha) \underbrace{\left(\frac{3}{2} \right) \left[-v_{sd}(k-1)i_{oq}(k-1) + v_{sq}(k-1)i_{od}(k-1) \right]}_{Im\left\{ (3/2) \vec{v}_s \vec{i}_o^* \right\}}, \quad (3.41)$$

where $Im\{\cdot\}$ denotes the imaginary part.

It should be pointed out that, although not necessary or recommended, also in a single-system islanded network the frequency and amplitude set-points of the DER system can be determined based on the droop mechanism, i.e., (3.38) and (3.40). Such determination of the set-points, however, ensures plug-and-play, stable operation of the DER systems should the network be expanded to a multi-system network.

3.7.2 Synchronization to the Network

As briefly mentioned in Section 3.7.1, in a multi-system network ω_{ref} is fine-tuned through the variable ω_{syn} (see Equation (3.38)). The synchronization scheme is shown in Fig. 3.21. The synchronization is exercised based on the fact that a nonzero value of ω_{syn} is reflected in ω_{ref} and thus changes the rotational speed of the DER system terminal voltage vector, with respect to ω_0 , such that the vector catches up with the transformer voltage vector and the two vectors are aligned. This ensures that the off-state voltage of the circuit breaker Br, Fig. 3.2, drops to a reasonably low value before the closure. ω_{syn} is delivered by a PI compensator that slowly integrates the q -axis component of the transformer voltage, i.e., v'_{sq} , until it falls within a small pre-specified neighborhood of zero. Once this condition is fulfilled, a straightforward logic mechanism within the synchronization scheme commands Br to close and also resets $\omega_{syn}(k)$ to zero. Thereafter, the DER system continues to operate as such, until it is restarted. To avoid multiple switching commands as a result of transients, v'_{sq} is low-pass filtered, and is accompanied by a hysteresis characteristic which is shown in Fig. 3.21 by Schmitt Trigger. The start-up process of the DER system begins at start time. Before the start time, the controllers of DER system are inactive and its gating pulses are blocked. When the clock time reaches to the start time the controllers are activated and the gating pulses are released by the activation of the enable signal and the synchronization timer is triggered. The synchronization process is

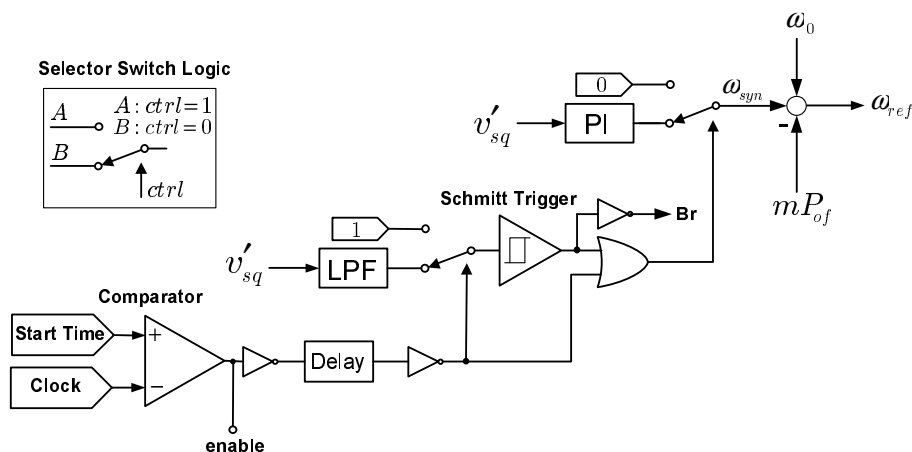


Figure 3.21: Synchronization scheme.

activated by a time delay, subsequent to the DER system start-up, to ensure the settlement of the DER system terminal voltage. When the time delay expires, the synchronization scheme starts to take effect. By completing the synchronization process the DER system comes on line through the closure of its corresponding circuit breaker, Br. It should be pointed out that the aforementioned synchronization process is also effective for a single-system network that starts from the black state. In such a scenario, the transformer voltage is already zero, so is its q -axis component v'_{sq} , as long as Br is open. Hence, the synchronization scheme closes Br once the time delay between the DER system start-up and the activation of the synchronization process is elapsed.

3.7.3 Simulation Results for a Two-System Example Network

The performance of the proposed islanded-mode control strategy in the example two-system network of Fig. 3.20 is demonstrated by Figs. 3.22 to 3.24. Thus, as Fig. 3.20 shows, in addition to the original DER system, another DER system of the same capacity and parameters, that is, DER System #2, has been interfaced with the PCC through an interface transformer; the electrical variables of DER System #2 are denoted by “~”. For compactness, the aggregate of the three loads in Fig. 3.1 has been identified as the “Loads”, here. The system is subjected to the following sequence of events: Initially, only the first DER system and the rectifier load are on line (i.e., Switch #3 is closed, Fig. 3.1). Moreover, the controllers of DER System #2 are inactive and its gating pulses are blocked. At $t = 0.35$ s the controllers are activated, the gating

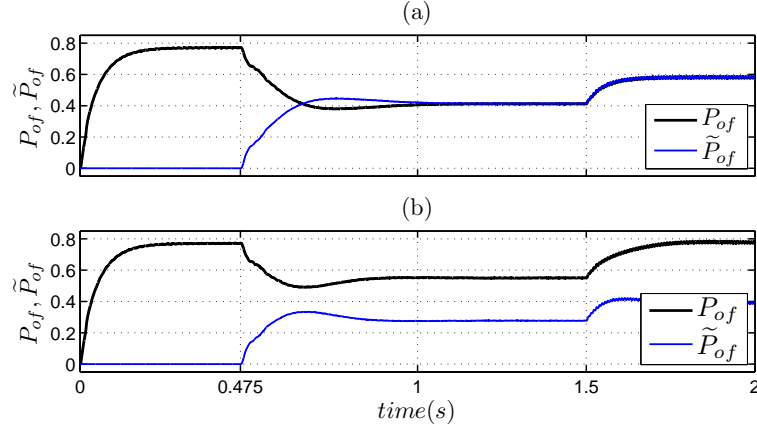


Figure 3.22: Power sharing between the two DER systems; (a) $m = \tilde{m} = 1.0$ (rad/s)/MW, and (b) $m = 1.0$ (rad/s)/MW, $\tilde{m} = 2.0$ (rad/s)/MW.

pulses are released, and the synchronization timer is triggered. At $t = 0.4$ s the time delay expires and the synchronization scheme starts to take effect. At $t = 0.475$ s the synchronization process is completed and DER System #2 comes on line through the closure of its corresponding circuit breaker. Therefore, the two DER systems operate in parallel, share the load real and reactive power, and jointly regulate the network voltage and frequency. Subsequently, at $t = 1.5$ s, the unbalanced load is also switched on, through the closure of Switch #2.

Figs. 3.22(a) and 3.22(b) illustrate the waveforms of the output real powers of the DER systems, in MW. It is observed that in both cases, until $t = 0.475$ s, i.e., until the time when DER System #2 is connected to the network, the load power is entirely supplied by the first DER system. Thereafter, the two DER systems share the load power based on their droop coefficients; the share of a DER system increases as the corresponding droop coefficient becomes smaller. The response plotted in Fig. 3.22(a) is obtained for the case where the droop coefficients of the two DER systems are equal (to 1.0 (rad/s)/MW) and, therefore, result in an equal power sharing after $t = 0.475$ s. By contrast, the response illustrated in Fig. 3.22(b) corresponds to the droop coefficients of $m = 1.0$ (rad/s)/MW and $\tilde{m} = 2.0$ (rad/s)/MW, resulting in the share of the first DER system being two times that of DER System #2.

Figs. 3.23 and 3.24 demonstrate the control performance in the two-system network, corresponding to case with the droop coefficients $m = 1.0$ (rad/s)/MW and $\tilde{m} = 2.0$ (rad/s)/MW, concentrating on the waveforms of the first DER system which takes a higher burden; the

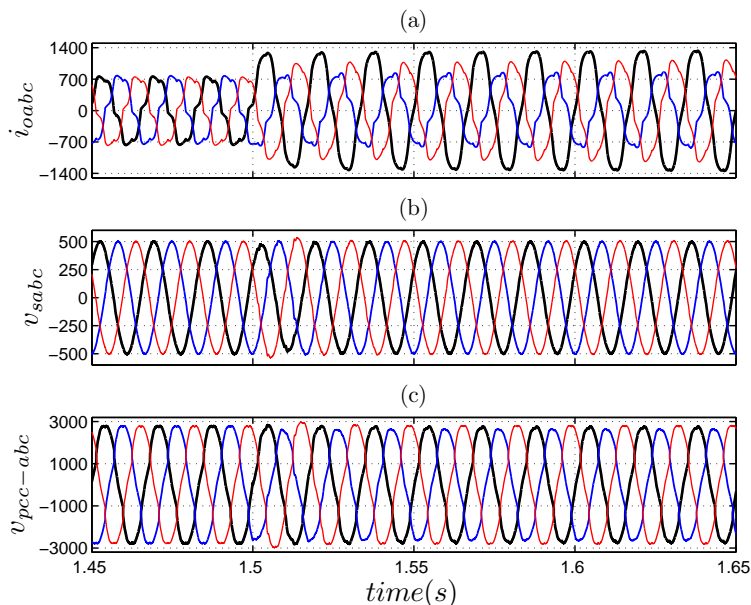


Figure 3.23: Zoomed view of (a) i_{oabc} , (b) v_{sabc} , and (c) PCC voltage, under distorted and unbalanced load currents.

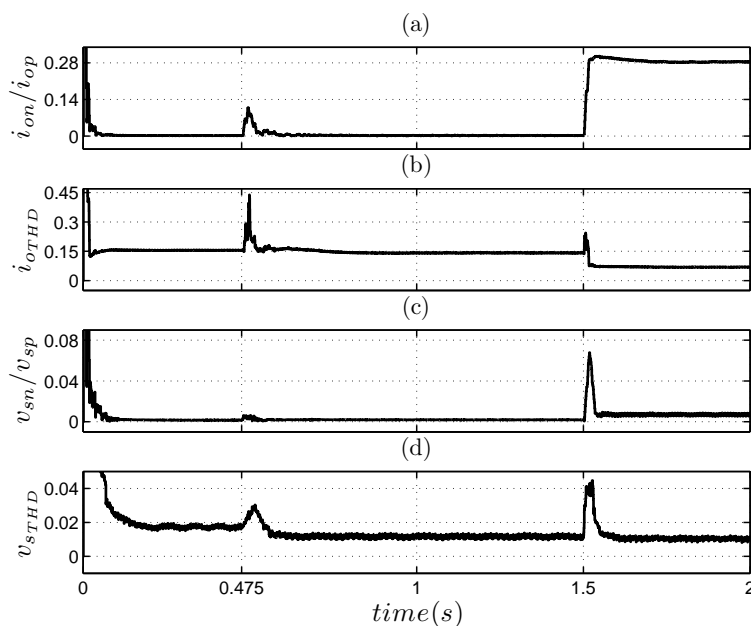


Figure 3.24: Overall response of the two-system microgrid.

waveforms of DER System #2 are very similar and thus not repeated, here. Fig. 3.23(a) shows that the DER system output current is distorted all along, due to the rectifier load, and also unbalanced from $t = 1.5$ s on, due to the intervention of the unbalanced load. Under this condition, the THD of the output current is about 7.5%, and its ratio of the negative-sequence

component to the positive-sequence component is 28% (Figs. 3.24(a) and (b)). However, due to the repetitive-based controller, both these two variables in the DER system terminal voltage are about 1% (Figs. 3.24(c) and (d)). Thus, the DER system terminal voltage shown in Fig. 3.23(b) is noticeably balanced and distortion-free. Although due to the leakage reactance of the interface transformer some imbalance and distortion remain, the PCC voltage is of a reasonably high quality, as Fig. 3.23(c) indicates.

3.8 Conclusion

This chapter proposes a voltage and frequency control strategy for dispatchable islanded electronically coupled DERs, based on a discrete-time mathematical model which is also valid for variable-frequency operation. To enhance the robustness of the proposed control strategy to unbalanced and/or distorted load currents, a combination of repetitive and deadbeat control is utilized. Moreover, the repetitive-control-based compensator is enhanced through a new control approach that ensures the rejection of periodic disturbance inputs, regardless of their frequency. This, in turn, enables quality and accurate voltage/frequency regulation in variable-frequency scenarios. In addition, the proposed control employs feedforward compensation to decouple the load dynamics from those of the DER system, and enables the parallel operation of multiple DER systems in a multi-system islanded network. Simulation studies conducted on a detailed switched model of the overall system demonstrate the performance and effectiveness of the proposed control strategy under the black-start condition, load switching incidents, unbalanced/distorted output currents, and parallel operation.

Chapter 4

Stability Enhancement in Droop-Controlled Microgrids

4.1 Introduction

The microgrid concept involves co-existence of multiple distributed energy resource units within a pre-specified part of an electrical network. One critical control task within the microgrid framework is the regulation of the network frequency and voltage magnitude, in the islanded (off-grid) mode of operation. Fundamentally, this objective is fulfilled through a shared contribution of real and reactive power by a multitude of dispatchable embedded DER systems. The most widely adopted technique to ensure power sharing and coordinated voltage/frequency regulation is to droop the frequency and magnitude of the point-of-coupling voltage of each DER system, versus the real and reactive powers that the DER system delivers to the network. The droop control method is easy to implement and enables decentralized control of the microgrid system by local measurement of powers and control of the amplitude and frequency of each DER system. It provides a power sharing mechanism between the DER systems in islanded mode and a power control mechanism for each DER system in the grid-connected mode. Both islanded and grid connected power control strategies are controllable by adjusting the droop coefficients.

The prime issue with respect to the conventional droop-based control is that, it is, in essence, a steady-state measure that is taken to prevent the DER systems from competing

against each other, for individually imposing the network frequency and voltage; any such competition would inevitably result in a network collapse. Consequently, the transient performance and stability of the droop-based decentralized control highly depend on the droop coefficients, and also on dynamic properties of the network, DER systems, and embedded loads. Even in terms of steady-state performance, the droop technique is effective the most for highly inductive networks, such as high-voltage transmission networks, but performs rather poorly when adopted for distribution networks. These dependencies, give rise to the likelihood of unsatisfactory transient performances, or even instabilities, in the islanded mode of operation.

This chapter is focused on the stability problems of the conventional droop control strategy and proposes an adaptive feedforward compensation that alters the dynamic coupling between a DER system and the host network, such that the system stability is desensitized to the droop coefficients and network dynamics. The proposed feedforward strategy preserves the steady-state effect that the conventional droop mechanism exhibits and therefore does not compromise the steady-state power sharing amongst the DER systems or the voltage/frequency regulation. Rather, it reshapes the contribution of the load dynamics in the control process, such that the system stability is enhanced. The proposed feedforward compensation is adaptive since it is periodically modified based on the system steady-state operating point, which, in turn, is estimated through the Recursive Least-Square (RLS) technique. The effectiveness of the proposed droop strategy is demonstrated through time-domain simulation studies, in the PSCAD/EMTDC software environment, conducted on a detailed switched model of a sample two-system microgrid.

4.2 Structure of the DER System

In this chapter, it is assumed that the DERs are all dispatchable and of the electronically-coupled type, and adopt the proposed adaptive feedforward strategy (not necessarily with identical parameters). Thus, hereafter, a DER system under study is referred to as the “*DER system*”, and the microgrid without the DER system is referred to as the “*rest of the microgrid*”, irrespective of whether or not it embeds any other DER system.

Fig. 4.1 shows a schematic diagram of the DER system. The power circuit of the DER

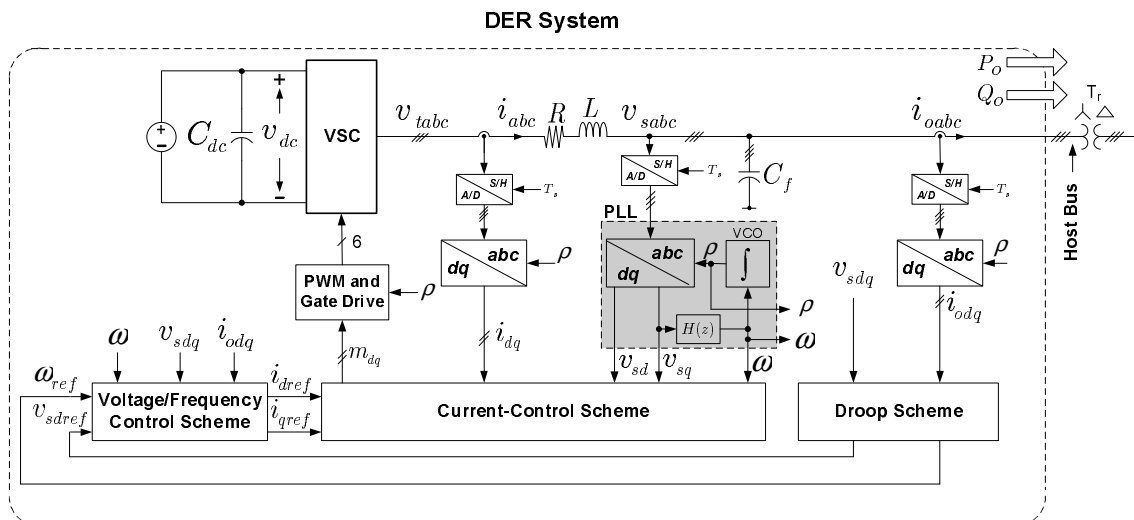


Figure 4.1: Schematic diagram of the DER system.

system consists of a conditioned prime energy source, a current-controlled VSC, and a three-phase LC filter. The per-phase resistance, inductance, and capacitance of the filter are denoted by R , L , and C_f , respectively. The resistance represents the ohmic loss of the filter inductor and also includes the effect of the on-state resistance of the VSC valves. The three-phase variables v_{sabc} , i_{abc} , and i_{oabc} are referred to as the “DER system terminal voltage”, “VSC ac-side current”, and “DER system output current”, respectively. The VSC dc side is paralleled with a dc-link capacitor, C_{dc} , and a voltage source. The latter represents the effect of a dispatchable energy storage device, e.g., a battery bank.

Fig. 4.1 also shows the control components of the DER system. It is noted that v_{sabc} , i_{abc} , and i_{oabc} are sampled and digitized by corresponding sample-and-hold (S/H) and analog-to-digital (A/D) converters. The sampled variables are then provided to respective $abc - to - dq$ frame transformation blocks. Fig. 4.1 further indicates that the DER system is controlled in a rotating dq frame whose d axis makes an angle, ρ , with respect to the stationary axis, i.e., the α axis. ρ is obtained from a PLL which also determines ω , that is, the frequency of the DER system terminal voltage. In the grid-connected mode of operation, the DER system terminal voltage is dictated by the rest of the microgrid, and ω represents the power system frequency. In the islanded mode, however, the DER system, in conjunction with the other DER systems, must contribute to the regulation of the network voltage and frequency, based on the proper commands given to the amplitude and frequency setpoints of the DER system terminal

voltage; the setpoints are, in turn, determined by a droop-based power sharing mechanism, which enables decentralized control of the network voltage and frequency, and ensures proper power sharing amongst the DER systems.

4.3 Basic Control

4.3.1 Current-Control Scheme

The function of the current-control scheme is to regulate the d - and q -axis components of the VSC ac-side current $i_{abc}(t)$, by means of the PWM switching strategy. This is primarily to ensure that the DER system is protected against network faults, but also enables the regulation of the amplitude and frequency of the DER system terminal voltage v_{sabc} .

Fig. 4.2 shows a block diagram of the current-control scheme and illustrates that two respective compensators, $K_i(z)$, process the error signals $e_d(k) = i_{dref}(k) - i_d(k)$ and $e_q(k) = i_{qref}(k) - i_q(k)$ and, based on the method described in Chapter 3, deliver the signals $m_d(k + 1)$ and $m_q(k + 1)$. These two last signals are then delayed by one sampling period and generate the signals $m_d(k)$ and $m_q(k)$ for the PWM scheme of the VSC; the delays are essential in a microprocessor-based implementation, due to the fact that the control signals, which are calculated based on the feedbacks at the k^{th} sampling instant, are practically computed during the time interval between the k^{th} and $(k + 1)^{th}$ sampling instants and, consequently, cannot be released earlier than the $(k + 1)^{th}$ sampling instant. Finally, the modulating signals $m_a(k)$, $m_b(k)$, and $m_c(k)$ are calculated from $m_d(k)$, $m_q(k)$, and $\rho(k)$, and determine the switching instants of the VSC valves. The task is achieved based on the symmetrical regular sampled PWM technique, [52], which renders the VSC switching frequency equal to the control system sampling frequency. As explained in Chapter 3, proper design of $K_i(z)$ ensures that $i_d(k)$ and $i_q(k)$ track their corresponding reference commands in two sampling periods, that is, $I_d(z)/I_{dref}(z) = I_q(z)/I_{qref}(z) = z^{-2}$.

4.3.2 Amplitude Regulation Scheme

Fig. 4.3 shows a block diagram of the amplitude regulation scheme whose function is to regulate $v_{sd}(k)$ and $v_{sq}(k)$, i.e., the d - and q -axis components of the DER system terminal voltage,

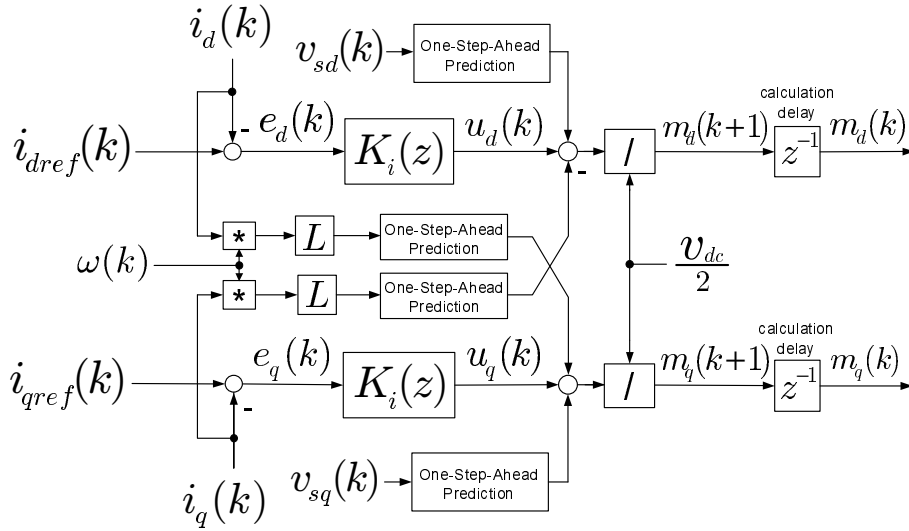


Figure 4.2: Block diagram of the current-control scheme of the DER system.

at their respective setpoints, $v_{sdref}(k)$ and $v_{sqref}(k)$. This objective goal is accomplished by the control of $i_d(k)$ and $i_q(k)$. In the scheme of Fig. 4.3, the d - and q -axis compensators, $K_v(z)$, process the error signals $e_{vd}(k) = v_{sdref}(k) - v_{sd}(k)$ and $e_{vq}(k) = v_{sqref}(k) - v_{sq}(k)$, respectively, and generate the setpoints $i_{dref}(k)$ and $i_{qref}(k)$ for the current-control scheme. As will be discussed in Section 4.3.3, $v_{sqref}(k)$ is indirectly employed in the frequency regulation scheme and has zero steady-state value. Hence, the amplitude of v_{sabc} , that is, $\sqrt{v_{sd}^2 + v_{sq}^2}$, is predominantly determined by v_{sd} , and, as such, v_{sdref} effectively serves as the setpoint for the amplitude of the DER system terminal voltage. As explained in Chapter 3, the control scheme of Fig. 4.3 transforms the closed-loop system to the two decoupled control loops of Fig. 4.4 in which the effective control plant is $H_v(z) = T_s/[c_f z^2(z-1)]$ (T_s is the sampling period).

4.3.3 Frequency Regulation Scheme

The objective of the frequency regulation scheme is to regulate ω , that is, the frequency of the DER system terminal voltage, at its setpoint ω_{ref} . As Fig. 4.1 shows, a PLL processes $v_{sq}(k)$ by the filter $H(z)$ and determines $\omega(k)$ in such a way that $v_{sq}(k)$ is forced to zero [37]. In the grid-connected mode, $\omega(k)$ is imposed by the rest of the microgrid and becomes equal to the power system angular frequency. However, in the islanded mode of operation, $\omega(k)$ is regulated

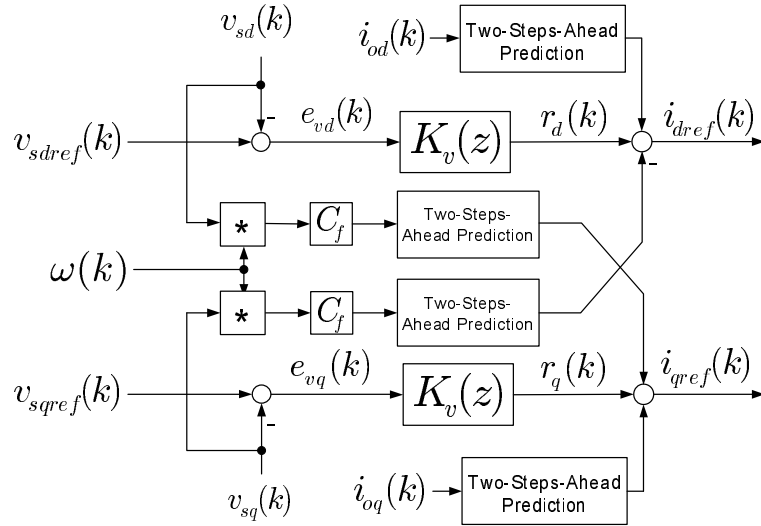


Figure 4.3: Block diagram of the amplitude regulation scheme.

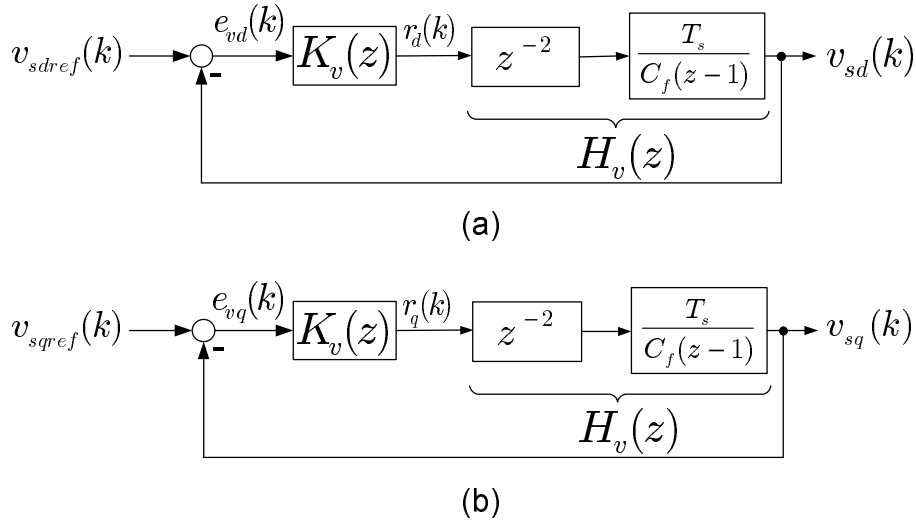


Figure 4.4: Block diagrams of the d - and q -axis closed loops equivalent to the amplitude regulation scheme of Fig. 4.3.

by $v_{sq}(k)$, through the control of $v_{sqref}(k)$. As explained in Chapter 3, $H(z)$ is of the form

$$H(z) = \frac{k_p}{z-1}, \quad (4.1)$$

for which k_p is the gain.

Fig. 4.5 shows a block diagram of the frequency regulation closed loop including the frequency regulation scheme. As Fig. 4.5 shows, a compensator, $K_\omega(z)$, processes the error $e_\omega(k) = \omega_{ref}(k) - \omega(k)$ and determines one component of $v_{sqref}(k)$; the other component of

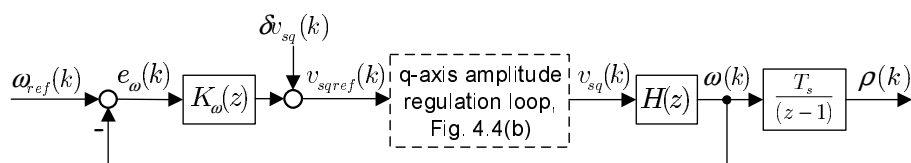


Figure 4.5: Block diagram of the frequency regulation loop.

$v_{sqref}(k)$, that is, δv_{sq} , is an auxiliary signal of zero steady-state value which plays an important role in the proposed adaptive feedforward strategy, as will be discussed in Section 4.4. The setpoint $v_{sqref}(k)$ is then tracked by $v_{sq}(k)$ through the action of the q -axis amplitude regulation loop of Fig. 4.4(b), and $\omega(k)$ is regulated at $\omega_{ref}(k)$. It should be noted that due to the pole of $H(z)$ at $z = 1$, $v_{sq}(k)$ (and therefore $v_{sqref}(k)$) settles at zero in a steady state. Therefore, in order for $\omega(k)$ to track $\omega_{ref}(k)$ with no steady-state error, $K_{\omega}(z)$ is sufficient to be a pure gain, k_{ω} .

4.4 Proposed Adaptive Feedforward Compensation

Fig. 4.6 illustrates a generic block diagram of a microgrid, whether in the islanded mode or in the grid-connected mode, in which a DER system is interfaced with the rest of the microgrid. As Fig. 4.6 indicates, $i_{od}(k)$ and $i_{oq}(k)$ are the responses of the rest of the microgrid to the DER system outputs, i.e., $v_{sd}(k)$, $v_{sq}(k)$, and $\omega(k)$. In turn, $v_{sd}(k)$ and $\omega(k)$ are the responses of the DER system to the setpoints $v_{sdref}(k)$ and $\omega_{ref}(k)$, respectively, while $v_{sq}(k)$ is an internal variable of the DER system control (see Section 4.3.3). It is noted that (filtered measures of) the DER system real and reactive powers determine the setpoints $v_{sdref}(k)$ and $\omega_{ref}(k)$, based on two respective droop characteristics.

Fig. 4.6 also illustrates the proposed feedforward compensation. As the figure indicates, the proposed feedforward compensation augments $v_{sdref}(k)$ with a signal, $\delta v_{sd}(k)$, and also determines the signal $\delta v_{sq}(k)$ for the frequency regulation scheme of the DER system (see Section 4.3.3), based on measures of $i_{od}(k)$ and $i_{oq}(k)$. As such, the feedforward compensation alters the dynamic coupling between the DER system and the rest of the microgrid, by manipulating $v_{sd}(k)$ and $\omega(k)$, based on $i_{od}(k)$ and $i_{oq}(k)$. The calculated values of the real- and reactive-power

and Q_{of} , as

$$\omega_{ref}(k) = \omega_0 - mP_{of}(k) \quad (4.6)$$

$$v_{sdref}(k) = V_0 - nQ_{of}(k) + \delta v_{sd}(k) , \quad (4.7)$$

where m and n are the real- and reactive-power droop coefficients, respectively, and $\delta v_{sd}(k)$ is an auxiliary signal with zero steady-state value, similar to the signal $\delta v_{sq}(k)$ which was introduced in Section 4.3.3; ω_0 and V_0 are the no-load frequency and amplitude of the DER system terminal voltage, respectively.

Substituting for $P_o(k)$ and $Q_o(k)$ in (4.4) and (4.5), from (4.2) and (4.3), one deduces

$$P_{of}(k+1) = \alpha_1 P_{of}(k) + 1.5(1 - \alpha_1)[v_{sd}(k)i_{od}(k) + v_{sq}(k)i_{oq}(k)] , \quad (4.8)$$

$$Q_{of}(k+1) = \alpha_1 Q_{of}(k) + 1.5(1 - \alpha_1)[-v_{sd}(k)i_{oq}(k) + v_{sq}(k)i_{od}(k)] . \quad (4.9)$$

To enhance system stability, the dynamic coupling between the DER system and rest of the microgrid [see Fig. 4.6] should be weakened as much as possible, but must exist in steady and quasi-steady states for real- and reactive-power sharing (i.e., conventional droop strategy). Thus, a small-signal model of the system is developed, such that the steady-state and dynamic characteristics can be treated separately. To that end, (4.8) and (4.9) are linearized about a steady-state operating point, to yield

$$\begin{aligned} \tilde{P}_{of}(k+1) &= \alpha_1 \tilde{P}_{of}(k) + 1.5(1 - \alpha_1)V_{sd0}\tilde{i}_{od}(k) \\ &+ 1.5(1 - \alpha_1)I_{od0}\tilde{v}_{sd}(k) + 1.5(1 - \alpha_1)I_{oq0}\tilde{v}_{sq}(k) , \end{aligned} \quad (4.10)$$

$$\begin{aligned} \tilde{Q}_{of}(k+1) &= \alpha_1 \tilde{Q}_{of}(k) - 1.5(1 - \alpha_1)V_{sd0}\tilde{i}_{oq}(k) \\ &- 1.5(1 - \alpha_1)I_{oq0}\tilde{v}_{sd}(k) + 1.5(1 - \alpha_1)I_{od0}\tilde{v}_{sq}(k) , \end{aligned} \quad (4.11)$$

where “ $\tilde{\cdot}$ ” and the subscript “0” denote the small-signal perturbation and the steady-state value, of a variable, respectively. It should be noted that the steady-state value of v_{sq} is zero, as explained in Section 4.3.3, and therefore does not appear in (4.10) or (4.11). It is also recalled

that $\delta v_{sd}(k)$ and $\delta v_{sq}(k)$ have zero steady-state values.

Defining

$$\beta_1 = \alpha_1 \quad (4.12)$$

$$\beta_2 = 1.5(1 - \alpha_1)V_{sd0} \quad (4.13)$$

$$\beta_3 = 1.5(1 - \alpha_1)I_{od0} \quad (4.14)$$

$$\beta_4 = 1.5(1 - \alpha_1)I_{oq0} , \quad (4.15)$$

one can rewrite (4.10) and (4.11) as

$$\tilde{P}_{of}(k+1) = \beta_1 \tilde{P}_{of}(k) + \beta_2 \tilde{i}_{od}(k) + \beta_3 \tilde{v}_{sd}(k) + \beta_4 \tilde{v}_{sq}(k) , \quad (4.16)$$

$$\tilde{Q}_{of}(k+1) = \beta_1 \tilde{Q}_{of}(k) - \beta_2 \tilde{i}_{oq}(k) - \beta_4 \tilde{v}_{sd}(k) + \beta_3 \tilde{v}_{sq}(k) . \quad (4.17)$$

The DER system amplitude regulation scheme (Section 4.3.2) ensures rapid regulation of $v_{sd}(k)$ and $v_{sq}(k)$ at their respective setpoints. Thus, replacing $v_{sdref}(k)$ by $v_{sd}(k)$ in (4.7), and linearizing the resultant equation, one deduces

$$\tilde{v}_{sd}(k) \approx -n\tilde{Q}_{of}(k) + \delta v_{sd}(k) . \quad (4.18)$$

Additionally, as Fig. 4.5 shows, $v_{sqref} = \delta v_{sq} + k_\omega(\omega_{ref} - \omega)$. On the other hand, the frequency regulation loop ensures that $\omega_{ref} - \omega \approx 0$ (Section 4.3.3), the amplitude regulation scheme ensures that $v_{sqref} \approx v_{sq}$ (Section 4.3.2), and the steady-state value of v_{sq} is zero (Section 4.3.3). Hence, one finds

$$\tilde{v}_{sq}(k) \approx \delta v_{sq}(k) . \quad (4.19)$$

Substituting for $\tilde{v}_{sd}(k)$ and $\tilde{v}_{sq}(k)$ in (4.16) and (4.17), based on (4.18) and (4.19), one finds

$$\tilde{P}_{of}(k+1) = \beta_1 \tilde{P}_{of}(k) - n\beta_3 \tilde{Q}_{of}(k) + \beta_2 \tilde{i}_{od}(k) + \beta_3 \delta v_{sd}(k) + \beta_4 \delta v_{sq}(k) , \quad (4.20)$$

$$\tilde{Q}_{of}(k+1) = (\beta_1 + n\beta_4) \tilde{Q}_{of}(k) - \beta_2 \tilde{i}_{oq}(k) - \beta_4 \delta v_{sd}(k) + \beta_3 \delta v_{sq}(k) . \quad (4.21)$$

Let $\delta v_{sd}(k)$ and $\delta v_{sq}(k)$ be determined in such a way that

$$\beta_3 \delta v_{sd}(k) + \beta_4 \delta v_{sq}(k) = \beta_2 \tilde{i}_{oq}(k) + n\beta_3 \tilde{Q}_{of}(k), \quad (4.22)$$

$$-\beta_4 \delta v_{sd}(k) + \beta_3 \delta v_{sq}(k) = -\beta_2 \tilde{i}_{od}(k) - n\beta_4 \tilde{Q}_{of}(k). \quad (4.23)$$

Then, (4.20) and (4.21) assume the following forms:

$$\tilde{P}_{of}(k+1) = \beta_1 \tilde{P}_{of}(k) + \beta_2 \tilde{i}_{od}(k) + \beta_2 \tilde{i}_{oq}(k), \quad (4.24)$$

$$\tilde{Q}_{of}(k+1) = \beta_1 \tilde{Q}_{of}(k) - \beta_2 \tilde{i}_{od}(k) - \beta_2 \tilde{i}_{oq}(k). \quad (4.25)$$

Equations (4.24) and (4.25) govern the small-signal dynamics of the real and reactive powers that the DER system delivers to the rest of the microgrid. The stability of the system described by (4.24) and (4.25) can be established by means of Lyapunov's direct method of stability [53]. To that end, consider the following positive semidefinite function, as a candidate Lyapunov function:

$$V(k) = [\tilde{Q}_{of}(k) + \tilde{P}_{of}(k)]^2 \quad (4.26)$$

Then

$$\Delta V(k) = V(k+1) - V(k) = (\beta_1^2 - 1)[\tilde{Q}_{of}(k) + \tilde{P}_{of}(k)]^2. \quad (4.27)$$

Since $0 < \beta_1 < 1$ (note that $\beta_1 = \alpha_1$, based on (4.12), and $\alpha_1 = e^{-T_s \omega_c} < 1$), then $\Delta V(k) \leq -\varepsilon_0 V(k)$, where $\varepsilon_0 = 1 - \beta_1^2 > 0$. This implies that the system is asymptotically stable [53]. Therefore, the transient response of the system is bound to decay to zero, and, in other words, the large-signal system response is bound to settle, in a steady state. It should be emphasized that the stability does not depend on the droop coefficients or on any network properties.

Expressing (4.22) and (4.23) in the matrix form

$$\begin{bmatrix} \beta_3 & \beta_4 \\ -\beta_4 & \beta_3 \end{bmatrix} \begin{bmatrix} \delta v_{sd}(k) \\ \delta v_{sq}(k) \end{bmatrix} = \begin{bmatrix} \beta_2 \tilde{i}_{oq} + n\beta_3 \tilde{Q}_{of}(k) \\ -\beta_2 \tilde{i}_{od} - n\beta_4 \tilde{Q}_{of}(k) \end{bmatrix}, \quad (4.28)$$

one can calculate $\delta v_{sd}(k)$ and $\delta v_{sq}(k)$ as

$$\begin{bmatrix} \delta v_{sd}(k) \\ \delta v_{sq}(k) \end{bmatrix} = \begin{bmatrix} g_1 & g_2 \\ g_2 & -g_1 \end{bmatrix} \begin{bmatrix} \tilde{i}_{oq}(k) \\ \tilde{i}_{od}(k) \end{bmatrix} + \begin{bmatrix} n\tilde{Q}_{of}(k) \\ 0 \end{bmatrix} \quad (4.29)$$

where

$$g_1 = \frac{\beta_2\beta_3}{\beta_3^2 + \beta_4^2} \quad (4.30)$$

$$g_2 = \frac{\beta_2\beta_4}{\beta_3^2 + \beta_4^2}. \quad (4.31)$$

One difficulty that arises in implementing the proposed feedforward compensation is that, to determine δv_{sd} and δv_{sq} , one needs knowledge about the steady-state values of the DER system terminal voltage and output current. On the other hand, in practice, the system operating point changes constantly as the loads shed back and forth, the power flow within the microgrid changes, etc. Consequently, the operating point needs to be estimated, for example, by means of an identification algorithm. This is explained next.

4.5 Recursive Least-Square Identification Scheme

Online estimation of system parameters, that is, online system identification, plays a crucial role in most adaptive control schemes [54]. For the adaptive feedforward compensation of Section 4.4, the parameters to be estimated are the steady-state values of the DER system terminal voltage and DER system output current (see (4.13)-(4.15)). It should be pointed out that these parameters do not bear a rigorous physical meaning; rather, they are the byproducts of the mathematical formulation, i.e., the linearization process.

In this chapter, the RLS identification method with an exponential forgetting algorithm [54] has been employed for estimating the required parameters; the estimates of parameters are updated at every sampling instant.

Equations (4.29)-(4.31) indicate that the proposed adaptive feedforward compensation re-

quires the parameters β_2, β_3 and β_4 . These parameters can be estimated if the RLS algorithm is applied to (4.16). Let us rewrite (4.16) as

$$\tilde{P}_{of}(k) = \beta_1 \tilde{P}_{of}(k-1) + \beta_2 \tilde{i}_{od}(k-1) + \beta_3 \tilde{v}_{sd}(k-1) + \beta_4 \tilde{v}_{sq}(k-1). \quad (4.32)$$

Defining the vector of parameters

$$\theta^T = [\beta_1, \beta_2, \beta_3, \beta_4], \quad (4.33)$$

and the regression vector

$$\phi^T(k) = [\tilde{P}_{of}(k), \tilde{i}_{od}(k), \tilde{v}_{sd}(k), \tilde{v}_{sq}(k)], \quad (4.34)$$

equation (4.32) can be rewritten as

$$\tilde{P}_{of}(k) = \phi^T(k-1)\theta. \quad (4.35)$$

The estimated parameters of the plant, denoted by $\hat{\theta}(k)$, are then calculated in the k^{th} sampling period, as [54]:

$$\varepsilon(k) = \tilde{P}_{of}(k) - \phi^T(k-1)\hat{\theta}(k-1) \quad (4.36)$$

$$K(k) = P(k-1)\phi(k-1)[\lambda + \phi^T(k-1)P(k-1)\phi(k-1)]^{-1} \quad (4.37)$$

$$\hat{\theta}(k) = \hat{\theta}(k-1) + K(k)\varepsilon(k) \quad (4.38)$$

$$P(k) = \frac{1}{\lambda}[I - K(k)\phi^T(k-1)]P(k-1), \quad (4.39)$$

where $\hat{\theta}^T = [\hat{\beta}_1, \hat{\beta}_2, \hat{\beta}_3, \hat{\beta}_4]$ is the vector of estimated parameters, $\varepsilon(k)$ is the error vector, $K(k)$ is known as Kalman gain, $P(k)$ is referred to as the error covariance, and λ is known as the forgetting factor and determines the speed of adaptation. The estimation algorithm is executed at every sampling period, through the following steps:

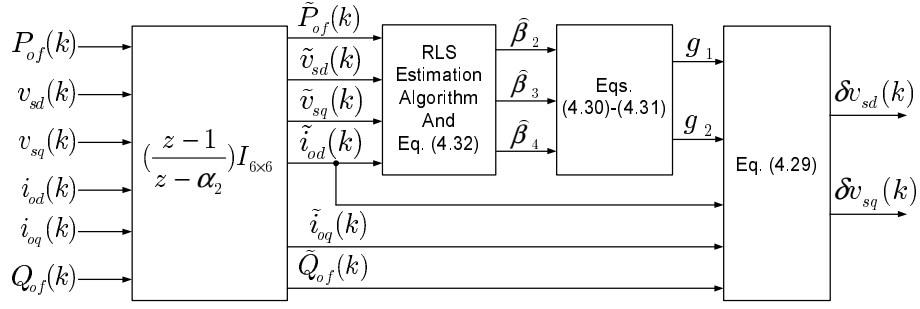


Figure 4.7: Block diagram of the scheme for calculation of feedforward coefficients based on the estimated parameters.

- a new set of data is acquired and the prediction error is computed, based on (4.36), using the old estimated parameters;
- Kalman gain is updated based on (4.37);
- estimated parameters vector, $\hat{\theta}(k)$, is calculated based on (4.38); and
- $P(k)$ is updated for the next sampling period, based on (4.39).

Once the parameters β_2 , β_3 and β_4 are estimated, g_1 and g_2 are calculated, based on (4.30) and (4.31), and $\delta v_{sd}(k)$ and $\delta v_{sq}(k)$ are generated based on (4.29). The small-signal perturbations of the variables involved (see Fig. 4.7) are extracted by high-pass filtering of the variables, to eliminate their steady-state components. Each high-pass filter has the following transfer function:

$$F(z) = \frac{z-1}{z-\alpha_2}, \quad (4.40)$$

where α_2 is the filter pole.

The process is illustrated by the block diagram of Fig. 4.7.

4.6 Study Cases and Results

To demonstrate the effectiveness of the proposed control strategy, a detailed switched model of a two-system test microgrid has been simulated in the PSCAD/EMTDC software environment; the simulation time step is $6.7096 \mu\text{s}$. The test microgrid is based on a typical 12.47-kV North

American distribution network [55], of which a simplified schematic diagram is illustrated in Fig. 4.8.

As Fig. 4.8 shows, the microgrid is divided into two subnetworks, Subnetwork 1 and Subnetwork 2, each embedding three-phase (residential and industrial) loads, as well as smaller single-phase networks. The two subnetworks are interfaced, respectively, with Bus 1 and Bus 12 of the upstream network, through the corresponding switches S3 and S4. The subnetworks can also be interconnected by the switch S5. In turn, Bus 1 and Bus 12 are energized through the corresponding transformers Tr3 and Tr4, from a 115-kV transmission system. When S5 is open, the two subnetworks demand the real and reactive powers of (3.1 MW, 2.4 MVar) and (1.2 MW, 0.8 MVar), respectively. As shown in Fig. 4.8, the part of the system that is outside of the microgrid boundaries is referred to as the “*grid*”.

Fig. 4.8 also shows that the microgrid embeds a 4-MVA DER system, DER1, and a 2-MVA DER system, DER2, which are connected to Bus 2 and Bus 13, respectively. Each DER system is interfaced with the host bus through a corresponding isolation transformer and a disconnect switch (S1 and S2, respectively, for DER1 and DER2); the transformers have a solidly-grounded wye winding configuration at their low-voltage sides. The control algorithm of each DER system (which includes the PWM, signal transformation and conditioning, phase-angle extraction, current control, amplitude and frequency regulation, power calculation and droop, adaptive feedforward compensation, and on-line parameter estimation schemes) is implemented by a Fortran code that is linked to the PSCAD/EMTDC model of the DER system. Parameters of the loads and transmission lines and other system parameters are given in Appendix C.

The case studies demonstrate the DER system performances in response to the connection of their corresponding host subnetworks to the grid, despite (intentional) inaccurate synchronization, and in response to the interconnection of the two subnetworks, when both of them are isolated from the grid. More importantly, two study cases are dedicated to highlighting the fact that the proposed feedforward compensation makes the dynamic performance and stability of the DER systems insensitive to the droop coefficients and load/network dynamic properties. For each study case, the response under the proposed control is compared with its counterpart under the conventional droop-based control; the latter control strategy is invoked by setting the

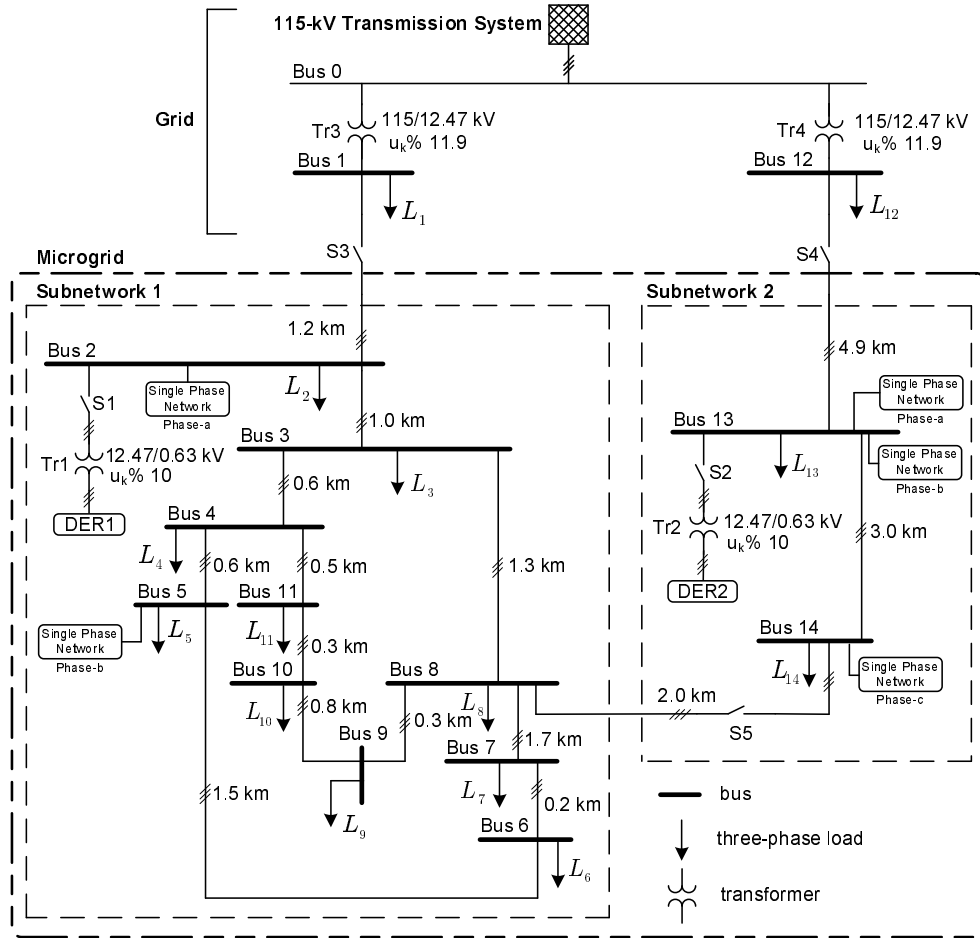


Figure 4.8: Schematic diagram of the test microgrid.

auxiliary signals $\delta v_{sd}(k)$ and $\delta v_{sq}(k)$ to zero. In the graphs to follow, the real powers, reactive powers, and currents are expressed in MW, MVar, and kA, respectively.

4.6.1 Case 1: Transition to the Grid-Connected Mode Following Inaccurate Synchronization

In this case, the switches S3, S4, and S5 are initially open (but, S1 and S2 are closed), the DER systems are disabled, and, therefore, Subnetwork 1 and Subnetwork 2 are de-energized. At $t = 0$, the DER systems are turned on, and their respective values of V_0 (see (4.7), Section 4.4) are ramped up from zero to 0.52 kV, in about 35 ms; hence, the (islanded) subnetworks get energized by their respective DER systems. Subsequently, S3 and S4 are closed, at $t = 0.75$ s, and the subnetworks are connected to the grid, while, right before the closure of S3 and

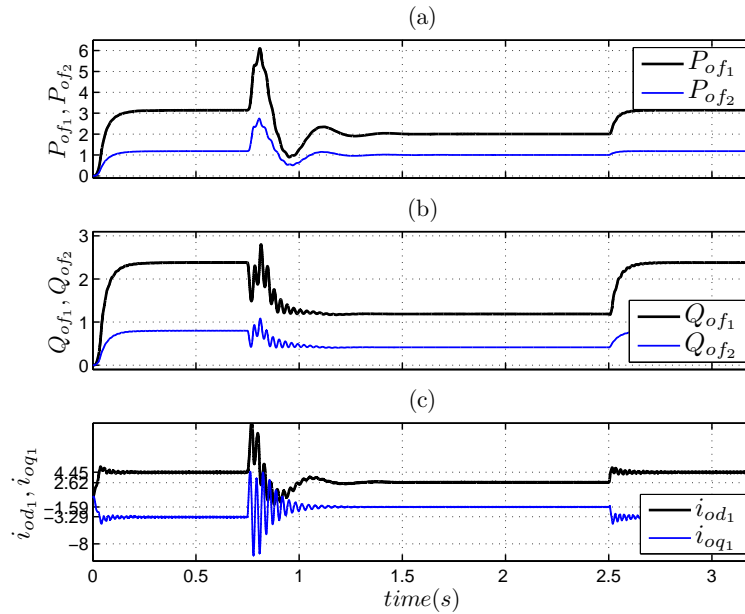


Figure 4.9: Sample responses of the DER systems to the connection of their host subnetworks to the grid, under the conventional control (Case 1).

S4, the voltages of Bus 2 and Bus 13 have phase displacements of about 24 degrees relative to the voltages of Bus 1 and Bus 12, respectively; the phase shifts are introduced intentionally to subject the DER systems to a rather severe disturbance. At $t = 2.5$ s, S3 and S4 are opened again and isolate the subnetworks from the grid. Thus, from $t = 2.5$ s onwards, the two subnetworks and DER systems operate under the same conditions that prevailed from $t = 0$ to $t = 0.75$ s. Figs. 4.9 and 4.10 illustrate the system response to the aforementioned sequence of events.

Fig. 4.9 illustrates the waveforms of the real- and reactive-power outputs of the DER systems, in addition to those of the d - and q -axis components of the output current of DER1, under the conventional droop-based control (hereafter, the conventional control). Similarly, Fig. 4.10 illustrates the waveforms of the same variables, but under the proposed feedforward compensation (hereafter, the proposed control). A comparison between Fig. 4.9 and Fig. 4.10 reveals that, while the responses of the DER systems to the switching incidents exhibit remarkable transient excursions and ringings under the conventional control, they are remarkably smooth and damped under the proposed control, despite the severity of the disturbances.

Fig. 4.11 illustrates the waveforms of the estimated parameters of DER1 (for instance), and indicates that, subsequent to each disturbance incident, they smoothly converge to their

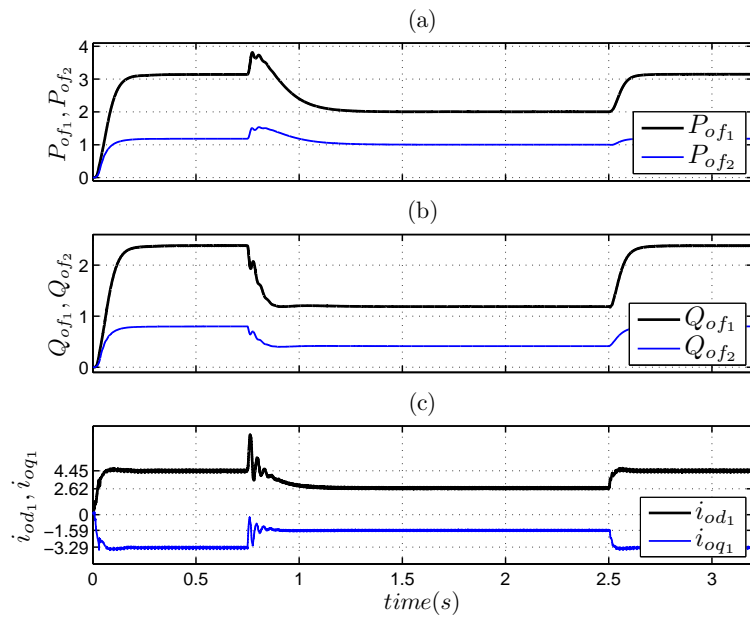


Figure 4.10: Sample responses of the DER systems to the connection of their host subnetworks to the grid, under the proposed control (Case 1).

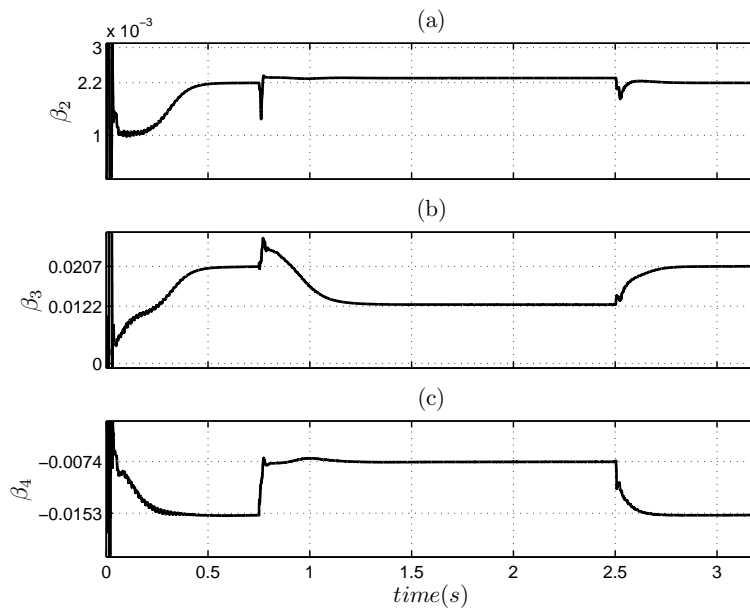


Figure 4.11: Estimated parameters of DER1 under the proposed control (Case 1).

steady-state values. As the figure shows, the settling values of β_2 , β_3 , and β_4 are, respectively, 0.0022, 0.0207, and -0.0153 , at the end of the time intervals over which Subnetwork 1 is isolated from the grid. On the other hand, under the off-grid condition, the settling values of i_{od1} and i_{oq1} are 4.45 kA and -3.29 kA, respectively (see Fig. 4.10), and the steady-state value of v_{sd1} is 0.475 kV (not shown in the graphs). Substituting for these three steady-state values in (4.13) through (4.15), one calculates β_2 , β_3 , and β_4 as 0.00221, 0.02069, and -0.01529 , respectively. It is noted that the calculated values are very close to the values estimated by the RLS identification scheme of DER1. It should be emphasized that β_2 , β_3 , and β_4 do not bear clear physical meanings, but are the byproducts of the mathematical formulation set forth in Section 4.4.

4.6.2 Case 2: Network Topological Change in the Islanded Mode

This case study demonstrates the responses of the DER systems to a network topological change, resulting in a power-flow change, in the islanded mode of operation. In this case, the system continues from the same steady state as that under the operating conditions of Case 1, that is, Subnetwork 1 and Subnetwork 2 are isolated from the grid (switches S3 and S4 are open) and independently energized by their respective DER systems. At $t = 4.0$ s, the switch S5 is closed (see Fig. 4.8), while, right before the switching incident, the voltages of Bus 8 and Bus 14 are phase-displaced by about 43 degrees; subsequent to the closure of S5, the aggregate of the loads of Subnetwork 1 and Subnetwork 2 is shared by the two DER systems. Figs. 4.12 and 4.13 illustrate the system response to the disturbance, under the conventional and proposed controls, respectively.

As Fig. 4.12 indicates, subsequent to the switching incident, the variables plotted in the figure experience remarkable fluctuations under the conventional control. By contrast, in spite of the disturbance severity, the system response is well damped under the proposed control, as Fig. 4.13 shows. A comparison between Figs. 4.12 and 4.13 confirms that the proposed control does not alter the steady-state power sharing regime that would exist under the conventional control.

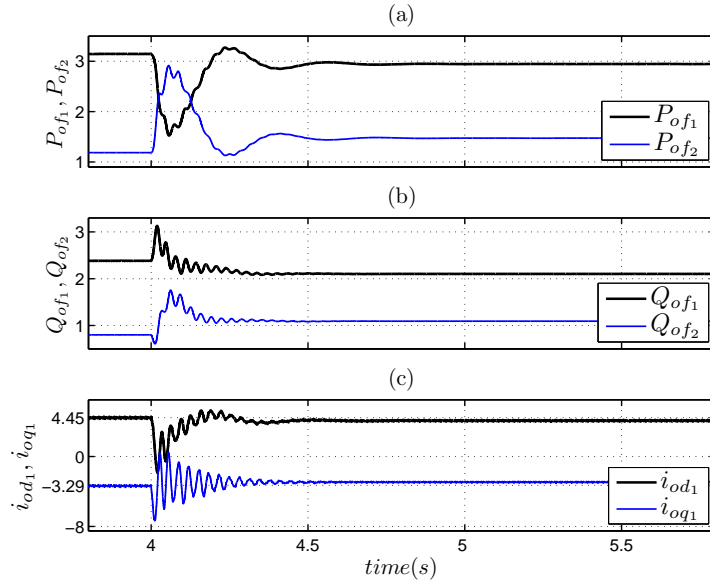


Figure 4.12: Sample responses of the DER systems to the interconnection of the two subnetworks, under the conventional control (Case 2).

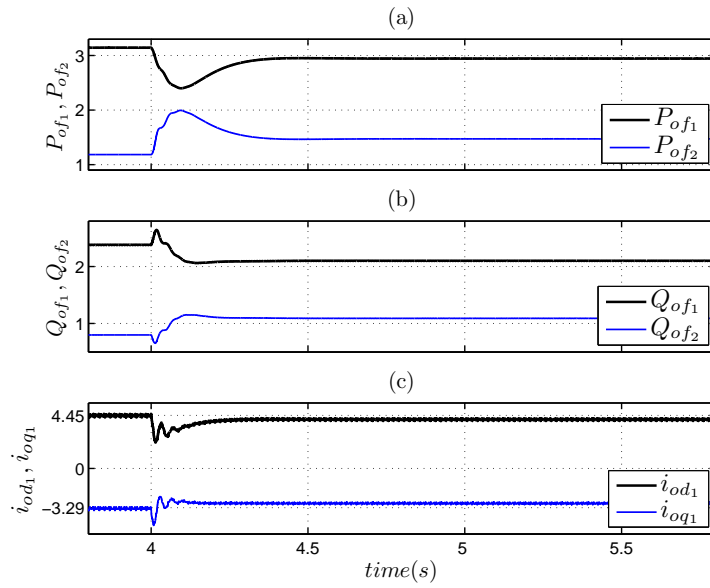


Figure 4.13: Sample responses of the DER systems to the interconnection of the two subnetworks, under the proposed control (Case 2).

4.6.3 Case 3: Stepwise Increase in Droop Coefficients

As has been analytically shown in [26], a sufficient increase in the droop coefficients has a destabilizing effect on the conventional control. This case study confirms the conclusion of [26], and also demonstrates the effectiveness of the proposed control in maintaining the system

stability in spite of an increase in the droop coefficients.

In this case, the system continues from the same steady state as that under the operating conditions of Case 2, that is, Subnetwork 1 and Subnetwork 2 are isolated from the grid, but the switch S5 is closed; therefore, the two DER systems share the aggregate of the two subnetwork loads. At $t = 6.5$ s, the frequency/real-power droop coefficients of DER1 and DER2 are stepped up, from $m_1 = 2.0$ to 12.0 (rad/s)/MW, and from $m_2 = 4.0$ to 24.0 (rad/s)/MW, respectively.

Fig. 4.14 depicts the responses of the DER systems under the conventional control and indicates that the system becomes oscillatory after $t = 6.5$ s. By contrast, as Fig. 4.15 shows, the system remains stable under the proposed control, in spite of the disturbance.

4.6.4 Case 4: Change in Load/Network Properties

As pointed out in the introduction of this chapter, the performance and stability of the conventional control depend on the load/network dynamic properties. This case study supports the claim and, further, demonstrates that the proposed control is robust to load/network characteristic variations.

In this case study, the system continues from the same steady state as that under the operating conditions of Case 2, that is, Subnetwork 1 and Subnetwork 2 are isolated from the grid, but connected to each other through S5, and the two DER systems share the aggregate load of the two subnetworks. At $t = 6.5$ s, an asynchronous machine, spun by a mechanical torque of -1.0 per-unit at angular speed close to 377 rad/s, gets connected to Bus 6 of Subnetwork 1; the connection is enabled by a circuit breaker and a voltage-matching transformer (none of these components are shown in Fig. 4.8). Parameters of the asynchronous machine are given in Appendix C. Figs. 4.16 and 4.17 illustrate the responses of the DER systems, under the conventional and proposed controls, respectively.

Fig. 4.16 shows that under the conventional control, the connection of the asynchronous machine to the subnetwork results in oscillations and instability. However, under the proposed control, the microgrid remains stable, as Fig. 4.17 indicates. Fig. 4.17 also shows that, from $t = 6.5$ s onwards, the two DER systems deliver comparatively smaller (real) powers, due to the power contribution of the asynchronous machine.

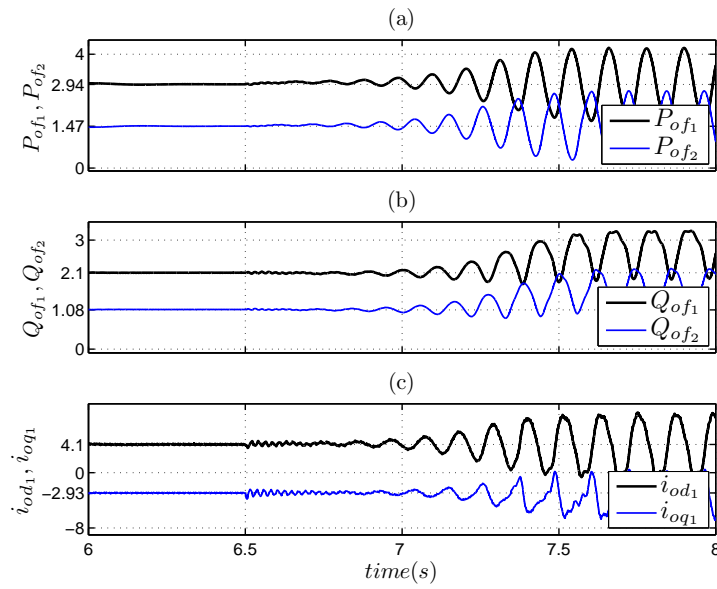


Figure 4.14: Sample responses of the DER systems to stepwise increase in their droop coefficients, under the conventional control (Case 3).

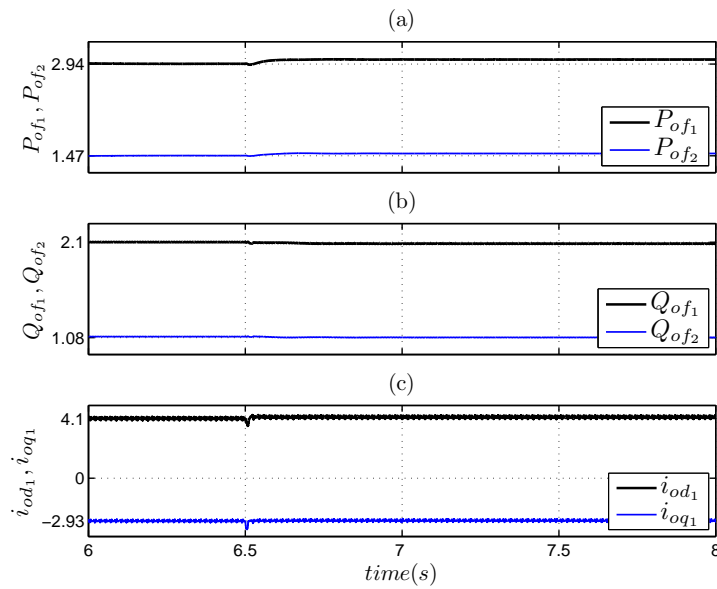


Figure 4.15: Sample responses of the DER systems to stepwise increase in their droop coefficients, under the proposed control (Case 3).

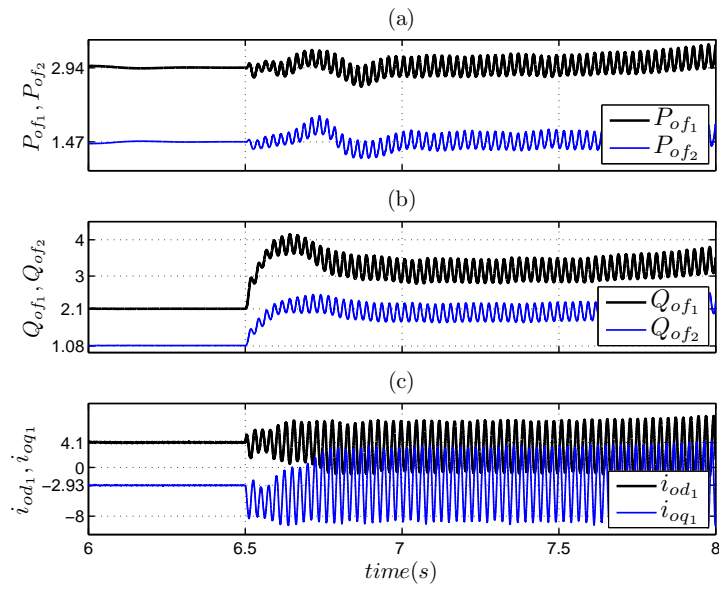


Figure 4.16: Sample responses of the DER systems to the introduction of an asynchronous machine to Subnetwork1, under the conventional control (Case 4).

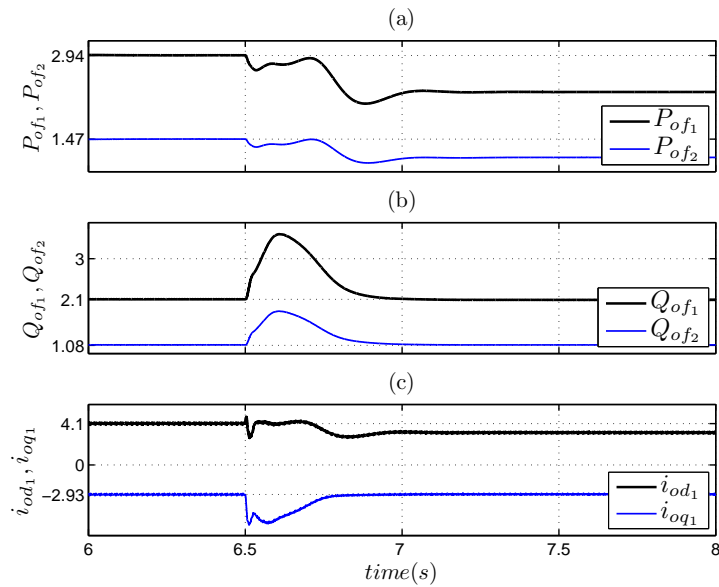


Figure 4.17: Sample responses of the DER systems to the introduction of an asynchronous machine to Subnetwork1, under the proposed control (Case 4).

4.7 Conclusion

This chapter proposed an adaptive feedforward compensation strategy that alters the dynamic coupling between a DER system and the host microgrid such that the system stability is made insensitive to droop coefficients and load/network dynamic characteristics. The proposed feedforward compensation preserves the steady-state effect that the conventional droop mechanism exhibits and, therefore, does not compromise the steady-state power sharing regime and voltage/frequency regulation offered by the conventional droop-based control. The feedforward compensation is adaptive since it is periodically modified according to the system steady-state operating point which, in turn, is estimated through an on-line RLS estimation technique. The chapter presented a discrete-time mathematical model and analytical framework, for the proposed feedforward compensation. The effectiveness of the proposed control was demonstrated through time-domain simulation studies, in the PSCAD/EMTDC software environment, conducted on a detailed switched model of a sample two-system microgrid.

Chapter 5

Unified DER Control

5.1 Introduction

One of the requirements of a microgrid is the capability of operation in both the islanded and grid-connected modes of operation. In the present microgrid control schemes, there is a distinction between the two modes of operation. In the grid-connected mode, the output voltage and frequency of the DER systems are dictated by the utility grid; the DER systems commonly utilize a current-mode or voltage-mode strategy for the control of their output real and reactive powers and/or dc-link voltages. However, when the microgrid operates in the islanded mode, the controllers must be replaced by an alternative control strategy, for instance, based on drooped characteristics, to ensure power sharing and coordinated voltage and frequency regulation. This necessitates an identification scheme for detecting the prevailing operating mode of the microgrid, and for changing the control strategy of the microgrid system, which adds to the complexity of the microgrid intelligence and should be avoided.

This chapter proposes a unified control scheme which can operate in both islanded and grid-connected modes of operation, to simplify the microgrid control system. The proposed control strategy benefits from both active feedback compensation and drooped characteristics; it enables the control of the real and reactive powers that the power-electronic interface of the DER exchanges with the host microgrid in the grid-connected mode of operation. In the islanded mode of operation, however, the compensators are saturated naturally and the droop-based control takes over to regulate the microgrid voltage and frequency, along with the other DERs.

The proposed control strategy can be directly adopted for dispatchable DERs, e.g., batteries, or, alternatively, it can be employed as a part of a nested control loop for non-dispatchable DERs, e.g., a photovoltaic array. Another merit of the proposed control strategy is that it assumes the same power circuit, current-control structure, and synchronization mechanism that are typically employed for grid-connected three-phase power-electronic interfaces. The chapter also presents the mathematical model and two sample applications of the proposed control strategy. Further, the effectiveness of the proposed control strategy is demonstrated through time-domain simulation of a two-system test microgrid, in the PSCAD/EMTDC software environment.

5.2 Structure of the DER System

Fig. 5.1 shows a schematic diagram of the DER system. The figure shows that the power circuit of the DER system consists of a DER, a current-controlled VSC, and a three-phase LC filter. The per-phase inductance and capacitance of the filter are denoted by L and C_f , respectively, and the resistance R represents the effective per-phase resistance of the filter inductor and VSC valves. As Fig. 5.1 shows, the connection between the DER system and the host network takes place through a circuit breaker, Br, which is controlled by the DER system intelligence for synchronization, start-up/shut-down, service/maintenance, or emergency isolation. Fig. 5.1 also shows that, the VSC dc-side is connected in parallel with a dc-link capacitor, C_{dc} , and the DER. The output power and current of the DER are denoted by P_{DER} and i_{DER} , respectively.

Fig. 5.1 also illustrates the control architecture of the DER system and indicates that the DER system is controlled in a rotating dq frame whose d axis makes an angle ρ against the stationary α axis. The angle ρ is obtained from a PLL which also provides the frequency of $v_{sabc}(t)$, denoted by ω . The overall control of the DER system is realized through four control schemes: (1) the current-control scheme, (2) the amplitude-control scheme, (3) the frequency-control scheme, and (4) the power-control scheme; these schemes will be introduced in more detail in the next section.

Fig. 5.1 further shows that the DER system receives output real- and reactive-power setpoints P_{oref} and Q_{oref} which are tracked in the grid-connected mode by the DER system output powers P_o and Q_o . In the islanded mode, however, the power setpoints become ineffective due

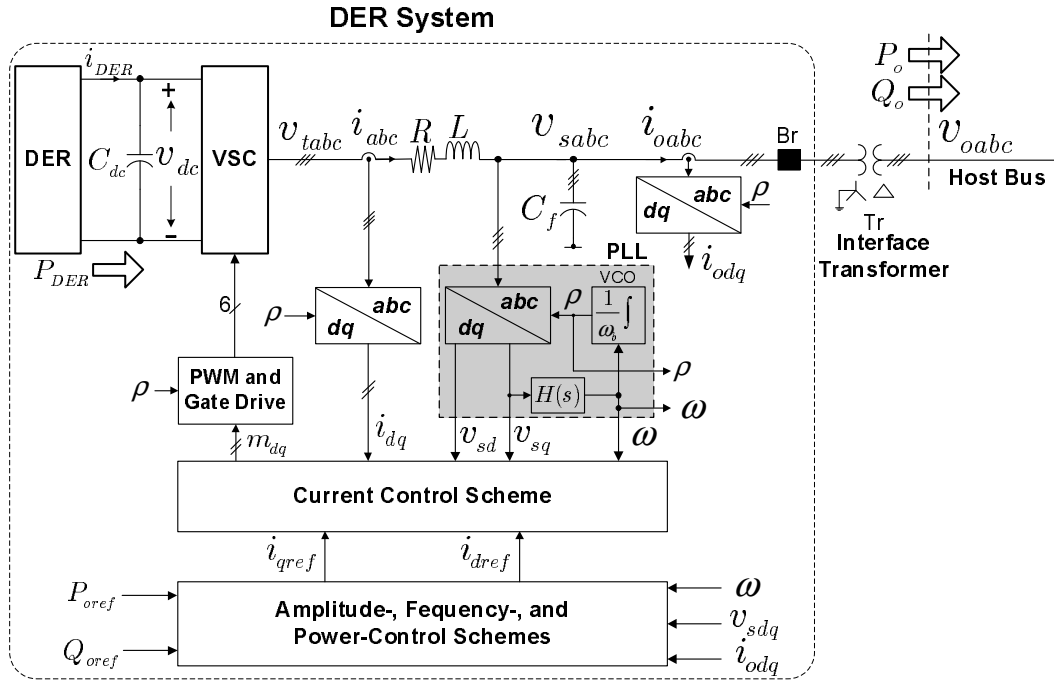


Figure 5.1: Schematic diagram of a DER system.

to the saturation of compensators, and a droop-based control strategy takes over automatically. This relieves the need for switching between different control strategies and also enables power sharing among the DER systems to regulate the voltage and frequency of the host microgrid.

In the forthcoming developments, except in the cases of the time and angles, all variables are expressed in per-unit (pu) terms with their base values denoted by the subscript **b**. The time and phase angles are expressed in second and radian, respectively. The base values are introduced in Appendix D.

5.3 Mathematical Model and Control Schemes

5.3.1 Current-Control Scheme

The current-control scheme constitutes the most basic block of the DER system control. The function of the current-control scheme is to regulate i_d and i_q , i.e., the d - and q -axis components of the VSC ac-side current $i_{abc}(t)$, by means of the PWM switching strategy. Thus, the current components i_d and i_q are independently controlled through their respective setpoints

such that

$$I_d(s) = G_i(s)I_{dref}(s) = \frac{1}{\tau_i s + 1} I_{dref}(s) \quad (5.1)$$

$$I_q(s) = G_i(s)I_{qref}(s) = \frac{1}{\tau_i s + 1} I_{qref}(s), \quad (5.2)$$

where the time-constant τ_i is a design choice. The setpoints i_{dref} and i_{qref} are limited by saturation blocks (not shown) to ensure protection of the VSC against network faults. The current-control scheme and its design procedures are discussed in Chapter 2.

5.3.2 Amplitude Regulation Scheme

The objective of the amplitude-control scheme is to regulate v_{sd} and v_{sq} , i.e., the d - and q -axis components of the DER system terminal voltage $v_{sabc}(t)$, at their respective setpoints v_{sdref} and v_{sqref} . In turn, this goal is accomplished by the control of i_{dref} and i_{qref} through the current-control scheme of Section 5.3.1. As will be discussed in Section 5.3.3, the setpoints v_{sqref} is determined by another control loop that regulates the frequency of $v_{sabc}(t)$. It will be discussed that the frequency regulation loop attempts to force v_{sq} to zero and, thus, the amplitude of the DER system terminal voltage, that is, $v_s = \sqrt{v_{sd}^2 + v_{sq}^2}$, is predominantly determined by v_{sd} . Therefore, v_{sdref} effectively serves as the setpoint for the amplitude of the DER system terminal voltage.

Fig. 5.2 illustrates a block diagram of the amplitude-control scheme for which the filters $K_v(s)$ are the compensators of the d - and q -axis control channels, and feedforward compensation is utilized to eliminate the coupling between v_{sd} and v_{sq} . Fig. 5.2 also shows that the measures of i_{od} and i_{oq} are included in the control process as two other feedforward signals to mitigate the impact of the DER system terminal current on v_{sd} and v_{sq} . The objective is that the compensated system behave under all network conditions in, approximately, the same way as the uncompensated system would behave under a no-load condition.

As explained below, the control scheme of Fig. 5.2 enables independent control of v_{sd} and v_{sq} , respectively, by i_{dref} and i_{qref} .

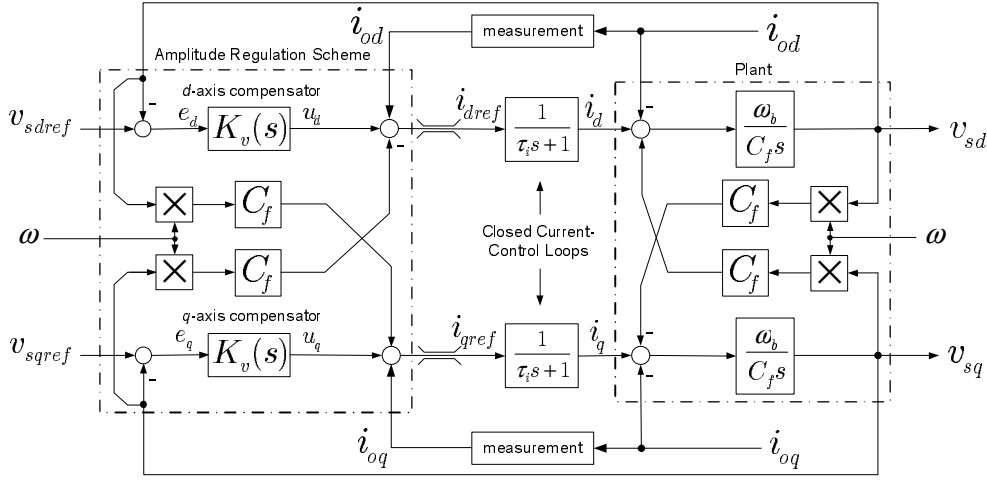


Figure 5.2: Block diagram of the amplitude-control scheme.

As discussed in Chapter 2, dynamics of v_{sd} and v_{sq} are governed by

$$\left(\frac{C_f}{\omega_b}\right) \frac{dv_{sd}}{dt} = (C_f\omega)v_{sq} + i_d - i_{od} \quad (5.3)$$

$$\left(\frac{C_f}{\omega_b}\right) \frac{dv_{sq}}{dt} = -(C_f\omega)v_{sd} + i_q - i_{oq}, \quad (5.4)$$

where ω is an output of the PLL (see Fig. 5.1) and related to the angle ρ as

$$\left(\frac{1}{\omega_b}\right) \frac{d\rho}{dt} = \omega(t) \quad (5.5)$$

It can also be seen from Fig. 5.2 that

$$i_{dref} = u_d - (C_f\omega)v_{sq} + i_{od} \quad (5.6)$$

$$i_{qref} = u_q + (C_f\omega)v_{sd} + i_{oq}, \quad (5.7)$$

where u_d and u_q are the outputs of the compensators $K_v(s)$ for the d - and q -axis channels, respectively. Substituting for i_{dref} and i_{qref} , from (5.6) and (5.7), in (5.1) and (5.2), one obtains

$$I_d = G_i(s)U_d - C_f G_i(s)\mathcal{L}\{\omega v_{sq}\} + G_i(s)I_{od} \quad (5.8)$$

$$I_q = G_i(s)U_q + C_f G_i(s)\mathcal{L}\{\omega v_{sd}\} + G_i(s)I_{oq}, \quad (5.9)$$

where $\mathcal{L}\{\cdot\}$ denote the Laplace transform operator. It then follows from applying Laplace transform to both sides of (5.3) and (5.4), and substituting in the resultants for $I_d(s)$ and $I_q(s)$ from (5.8) and (5.9), that

$$\left(\frac{C_f}{\omega_b}\right) sV_{sd} = G_i(s)U_d + \underbrace{C_f[1 - G_i(s)]\mathcal{L}\{\omega v_{sq}\} - [1 - G_i(s)]I_{od}}_{\text{transient terms}} \quad (5.10)$$

$$\left(\frac{C_f}{\omega_b}\right) sV_{sq} = G_i(s)U_q - \underbrace{C_f[1 - G_i(s)]\mathcal{L}\{\omega v_{sd}\} - [1 - G_i(s)]I_{oq}}_{\text{transient terms}}. \quad (5.11)$$

It is then noted that the transfer function $G_i(s) = 1/(\tau_i s + 1)$ has a unity dc gain, and therefore $[1 - G_i(s)] = \tau_i s/(\tau_i s + 1)$ has a zero dc gain. Hence, if τ_i is adequately small, those terms of (5.10) and (5.11) which are labeled as “*transient terms*” assume negligible values over a fairly wide range of frequencies and, thus, (5.10) and (5.11) can be approximated as

$$\frac{V_{sd}(s)}{U_d(s)} = \frac{V_{sq}(s)}{U_q(s)} \approx \left(\frac{\omega_b}{C_f}\right) \frac{G_i(s)}{s}. \quad (5.12)$$

Equation (5.12) indicates that v_{sd} and v_{sq} can be independently controlled by u_d and u_q , respectively, that is, the control scheme of Fig. 5.2 is equivalent to the two decoupled Single-Input-Single-Output (SISO) control loops shown in Fig. 5.3.

The use of PI compensators for $K_v(s)$ in the amplitude-control scheme of Fig. 5.2 could guarantee an adequately fast and stable closed-loop response as discussed in Chapter 2. However, network imbalance results in second-order harmonic components in i_{od} and i_{oq} that distort v_{sd} and v_{sq} . The impact of the second-order components of i_{od} and i_{oq} can be mitigated if $K_v(s)$ includes a pair of complex-conjugate poles at the double power system frequency. For example, if $K_v(s)$ is

$$K_v(s) = \frac{k_2 s^2 + k_1 s + k_0}{s^2 + (2\omega_b)^2}, \quad (5.13)$$

where k_0 , k_1 , and k_2 are the compensator parameters, then, the transfer function of each closed amplitude-control loop, $H_v(s) = V_{sd}(s)/V_{sdref}(s)$, and $H_v(s) = V_{sq}(s)/V_{sqref}(s)$, is

$$H_v(s) = \frac{\alpha(k_2 s^2 + k_1 s + k_0)}{s(s + \omega_i)(s^2 + (2\omega_b)^2) + \alpha(k_2 s^2 + k_1 s + k_0)} \quad (5.14)$$

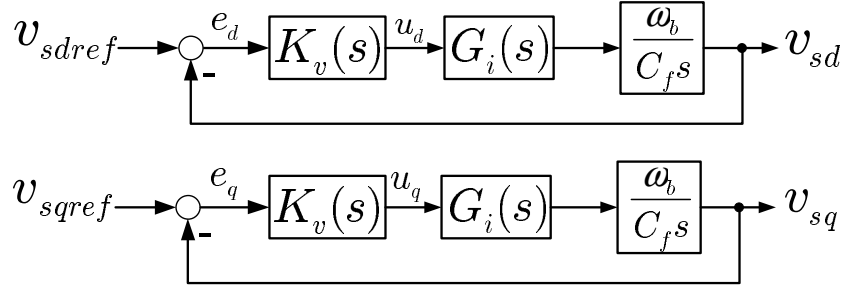


Figure 5.3: Equivalent block diagrams for the closed amplitude-control loops.

The poles of $H_v(s)$ can be placed arbitrarily by proper selection of the parameters k_0 , k_1 , and k_2 . For example, if the desired poles should have the negative real value $-p_1$, $-p_2$, $-p_3$, and $-p_4 = -\omega_i + p_1 + p_2 + p_3$, then, k_0 , k_1 , and k_2 are computed as

$$k_2 = [p_1 p_2 + p_1 p_3 + p_1 p_4 + p_2 p_3 + p_2 p_4 + p_3 p_4 - (2\omega_b)^2] / \alpha, \quad (5.15)$$

$$k_1 = [p_1 p_2 p_3 + p_1 p_2 p_4 + p_2 p_3 p_4 + p_1 p_3 p_4 - \omega_i (2\omega_b)^2] / \alpha, \quad (5.16)$$

$$k_0 = (p_1 p_2 p_3 p_4) / \alpha, \quad (5.17)$$

where

$$\omega_i = 1 / \tau_i, \quad (5.18)$$

$$\alpha = \omega_b / (\tau_i C_f). \quad (5.19)$$

5.3.3 Frequency Regulation Scheme

The objective of the frequency-control scheme is to regulate ω (i.e., the frequency of $v_{sabc}(t)$) at the setpoint ω_{ref} . The objective is fulfilled by the closed-loop structure illustrated in Fig. 5.4. As Fig. 5.4 shows, a compensator $K_\omega(s)$ processes the error signal $e_\omega = \omega_{ref} - \omega$ and determines the setpoint v_{sqref} ; the feed-back signal ω is obtained from the PLL [see Fig. 5.1]. Then, v_{sq} tracks v_{sqref} through the action of the q -axis amplitude-control loop of Fig. 5.3 and affects ω , as explained below.

As Fig. 5.1 shows, the PLL filter $H(s)$ processes v_{sq} and determines ω . The process is

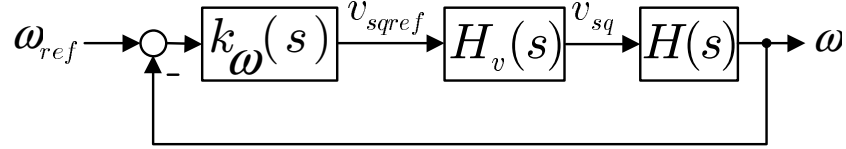


Figure 5.4: Block diagram of the frequency-control loop.

governed by the equation

$$\Omega(s) = H(s)V_{sq}(s), \quad (5.20)$$

in which $H(s)$ has the following transfer function

$$H(s) = \frac{\beta}{s}, \quad (5.21)$$

where β is a constant parameter. Due to the pole of $H(s)$ at $s = 0$, both v_{sq} and v_{sqref} settle at zero in a steady state. Therefore, the compensator $K_\omega(s)$ can be selected to be a pure gain, that is

$$K_\omega(s) = k_\omega. \quad (5.22)$$

As Fig. 5.4 indicates, the transfer function of the closed frequency-control loop can be formulated as

$$H_\omega(s) = \frac{\Omega(s)}{\Omega_{ref}(s)} = \frac{k_\omega\beta H_v(s)}{s + k_\omega\beta H_v(s)}, \quad (5.23)$$

where $H_v(s)$ is given by (5.14).

5.3.4 Power Control Scheme

The function of the power-control scheme is to regulate the real- and reactive-power outputs of the DER system in the grid-connected mode, at their respective setpoints P_{oref} and Q_{oref} , and to ensure proper power sharing between the DER systems in the islanded mode. The objective is fulfilled by a real-power-control scheme and a reactive-power-control scheme, as described

below.

Real-Power Control Scheme

Fig. 5.5 illustrates a block diagram of the real-power-control scheme. As Fig. 5.5 shows, a compensator $K_p(s)$ processes the error signal $P_{oref} - P_o$ and determines for the frequency-control scheme the first component of the setpoint ω_{ref} , denoted by ω_p . The other component of ω_{ref} consists of a constant term, ω_0 , minus a signal proportional to a filtered measure of P_o ; ω_0 is typically assigned the value 1.0 pu corresponding to the nominal power system frequency. This component of ω_{ref} grants the real-power-control loop a $P-\omega$ droop characteristic enabling real-power sharing between the DER system and other DER systems, in the islanded mode of operation. As shown in Fig. 5.5, the proportionality constant and the filter time constant are denoted by m and τ_f , respectively.

Fig. 5.5 also indicates that P_o is controlled by ω (and, therefore, by ω_{ref}) based on an integral relationship. To confirm this relationship, let us consider the circuit model of Fig. 5.6 in which the DER system is represented by a three-phase voltage source with controllable amplitude and frequency, the interface transformer is approximated by its leakage inductance L_T , and the host bus voltage v_{oabc} is expressed as $\widehat{v}_o e^{j(\omega_b \omega_n t + \theta_n)}$, where ω_n is the frequency of all voltages and currents of the host network, and θ_n is the initial phase angle of the host bus voltage. Then, assuming a quasi steady-state condition, the complex power $S = P_o + jQ_o$ delivered by the DER system to the network can be formulated as

$$S = P_o + jQ_o = \left\{ \widehat{v}_o e^{j(\omega_b \omega_n t + \theta_n)} \overline{\left(\frac{\widehat{v}_s e^{j\rho} - \widehat{v}_o e^{j(\omega_b \omega_n t + \theta_n)}}{jX_T} \right)} \right\}, \quad (5.24)$$

where the overline denotes the complex conjugate of the expression inside the brackets, and $X_T = L_T \omega_n$. Equating the real parts of the two sides of (5.24), one finds

$$P_o = \frac{\widehat{v}_s \widehat{v}_o}{X_T} \sin(\rho - \theta_n - \omega_b \omega_n t) \quad (5.25)$$

Then, in view of the fact that the typical value of X_T is small, one finds $\sin(\rho - \theta_n - \omega_b \omega_n t)$ to

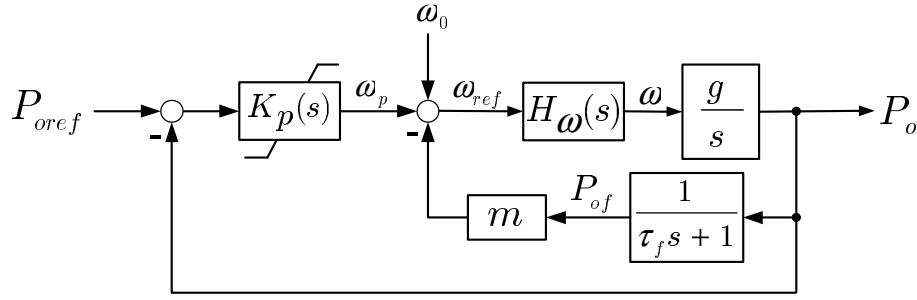


Figure 5.5: Block diagram of the real-power control scheme.

be fairly small and, as such, approximately equal to its argument, $\rho - \theta_n - \omega_b \omega_n t$. Hence,

$$P_o \approx \frac{\widehat{v}_s \widehat{v}_o}{X_T} (\rho - \theta_n - \omega_b \omega_n t). \quad (5.26)$$

Equation (5.26) indicates that P_o can be controlled by ρ which, based on (5.5), is the integral of ω . It also follows from (5.26) that the gain of the integration block in Fig. 5.5 is

$$g = \frac{\widehat{v}_s \widehat{v}_o}{X_T}, \quad (5.27)$$

which can be assumed to be fairly constant since, typically, \widehat{v}_s and \widehat{v}_o change only slightly about their nominal values (of 1.0 pu). It should be pointed out that the assumption of steady-state condition also implies that ρ has a component equal to $\omega_n \omega_b t$, meaning that ω and ω_{ref} each have a constant component equal to ω_n . To ensure that the assumption is plausible, the open-loop gain and phase crossover frequencies of the loop of Fig. 5.5 must be selected to be sufficiently smaller than the closed-loop bandwidths of the frequency-control loop, such that $|H_\omega(j\omega)| \approx 1$ over a wide frequency band. This can be ensured through judicious selection of the filter time constant τ_f and proper design of the compensator $K_p(s)$.

Based on Fig. 5.5, one finds that

$$\frac{P_o(s)}{\Omega_p(s)} = \frac{g(s + \omega_f)}{s^2 + \omega_f s + mg\omega_f}, \quad (5.28)$$

where $\omega_f = 1/\tau_f$. Then, the compensator $K_p(s)$ can be designed based on a variety of methods.

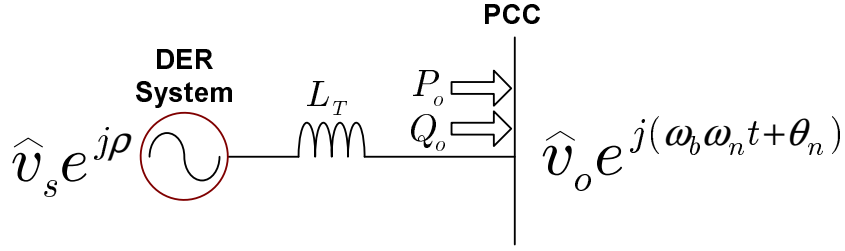


Figure 5.6: Simplified model of a grid-connected DER system.

For example, let $K_p(s)$ be the following filter which includes an integral term, has the gain k_p , and also cancels the poles and zero of (5.28):

$$K_p(s) = \frac{s^2 + \omega_f s + mg\omega_f}{g(s + \omega_f)} \left(\frac{k_p}{s} \right) \quad (5.29)$$

Then, the transfer function of the closed real-power-control loop takes the form

$$H_p(s) = \frac{P_o(s)}{P_{oref}(s)} = \frac{k_p}{s + k_p}, \quad (5.30)$$

which is a first-order transfer function whose pole can be arbitrarily set to a negative value far enough into the left-half plane by k_p .

In the grid-connected mode of operation the host bus voltage is more or less dictated by the host network, that is, its amplitude and frequency are imposed. Thus, any slight change in the angle ρ results in a considerable change in P_o . This property enables the imposition of relatively small saturation limits on ω_p , i.e., on the output of $K_p(s)$. Imposing such limits on ω_p is desirable for the islanded mode of operation, as explained below.

In the islanded mode of operation, to regulate P_o at P_{oref} may and typically will require a considerable shift in the network frequency. However, this cannot happen (and should not happen due to the codes and standards) since ω_p is limited to fairly small values about zero. Once $K_p(s)$ is saturated, the power regulation mechanism becomes ineffective and ω_{ref} is adjusted exclusively by the droop mechanism. Under this condition, P_o no longer tracks P_{oref} , but is determined based on the network power demand and droop coefficients (that is, the gains m) of the DER systems.

Reactive-Power Control Scheme

Fig. 5.7 shows a block diagram of the reactive-power-control scheme. A comparison between Figs. 5.5 and 5.7 reveals that the structure and principles of operation of the reactive-power-control scheme are very similar to those of the real-power-control scheme. The main difference is that the reactive-power output of the DER system is controlled by \widehat{v}_s , that is, the amplitude of the DER system terminal voltage. As discussed in Section 5.3.2, \widehat{v}_s is approximately equal to v_{sd} which, in turn, tracks the setpoint v_{sdref} based on the closed-loop transfer function $H_v(s)$, formulated by (5.14). The transfer function from \widehat{v}_s to Q_o can be derived based on (5.24).

Equating the imaginary parts of the both sides of (5.24), one finds

$$Q_o = \frac{\widehat{v}_o \cos(\rho - \theta_n - \omega_b \omega_n t)}{X_T} \widehat{v}_s - \frac{\widehat{v}_o^2}{X_T} \quad (5.31)$$

As discussed earlier, $\sin(\rho - \theta_n - \omega_b \omega_n t)$ has a typically small value. Hence, $\cos(\rho - \theta_n - \omega_b \omega_n t) \approx 1$, and (5.31) can be rewritten as

$$Q_o = \left(\frac{\widehat{v}_o}{X_T} \right) \widehat{v}_s - \frac{\widehat{v}_o^2}{X_T} = \left(\frac{\widehat{v}_o}{X_T} \right) v_{sd} - \frac{\widehat{v}_o^2}{X_T} \quad (5.32)$$

It then follows from (5.32) that the gain h in the plant block of Fig. 5.7 is

$$h = \frac{\widehat{v}_o}{X_T}, \quad (5.33)$$

which can be assumed to be fairly constant due to the fact that \widehat{v}_o typically lies in a small neighborhood about its steady-state value (of about 1.0 pu). The term \widehat{v}_o^2/X_T in (5.32) can be regarded as a disturbance input to the control loop, as Fig. 5.7 illustrates.

As Fig. 5.7 shows, in the reactive-power-control loop, a compensator $K_q(s)$ processes the error signal $Q_{oref} - Q_o$ and determines the signal v_q , that is, the first component of the setpoint v_{sdref} for the amplitude-control scheme. The other component of v_{sdref} consists of a constant term V_0 minus a signal proportional to a filtered measure of Q_o ; as shown in Fig. 5.7, the proportionality constant and the filter time constant are denoted by n and τ_f , respectively. This latter component of v_{sdref} grants the reactive-power-control loop a $Q - V$ droop characteristic enabling reactive-power sharing between the DER system and other DER systems in the is-

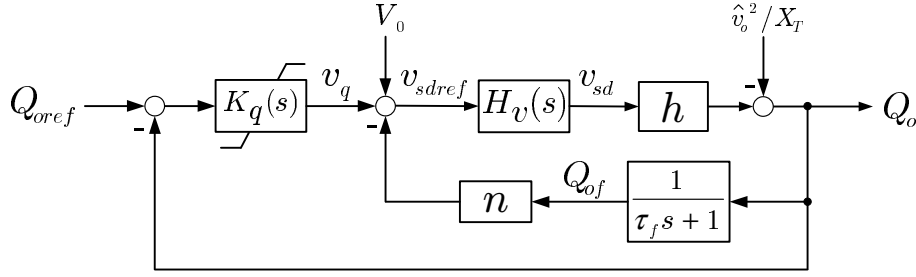


Figure 5.7: Block diagram of the reactive-power control scheme.

landed mode of operation. Similar to the real-power-control case, in the grid-connected mode the compensator $K_q(s)$ adjusts v_q and regulates Q_o at Q_{oref} , but it is saturated in the islanded mode of operation and thus leaves the control task to the $Q - V$ droop mechanism. Once $K_q(s)$ is saturated, v_q is limited to a fairly small value about zero and, therefore, \hat{v}_s assumes a value fairly close to that of V_0 which, typically, is set to about 1.0 pu. The exact value of \hat{v}_s depends on the value of Q_o which, in turn, depends on the network aggregate reactive-power demand and the droop coefficients (i.e., the gains n) of the DER systems of the microgrid.

Assuming that $|H_v(j\omega)| \approx 1$ due to large bandwidth of the amplitude-control loop, based on Fig. 5.7 the transfer function from v_q to Q_o is given by

$$\frac{Q_o(s)}{V_q(s)} = \frac{h(s + \omega_f)}{s + (1 + nh)\omega_f}, \quad (5.34)$$

where $\omega_f = 1/\tau_f$. The compensator $K_q(s)$ can then be designed for desired closed-loop bandwidth, gain margin, and phase margin. A PI compensator has been considered in this chapter.

5.4 Application Examples

The proposed unified control strategy can be adopted for both dispatchable and non-dispatchable DER systems in a microgrid setting. This section demonstrates the application of the method for two example DER systems: a PV system and a battery energy storage system.

5.4.1 PV System

For the first application, let us assume that in Fig. 5.1 the DER is a PV generator, and thus the DER system represent a three-phase PV energy system. Thus, P_{DER} and i_{DER} in Fig. 5.1

represent P_{pv} and i_{pv} , respectively. The control objective in this case is to regulate the dc-link voltage v_{dc} at its respective setpoint v_{dcref} which, in turn, is determined by a MPPT scheme [12].

Fig. 5.8 illustrates a feedback mechanism that can regulate v_{dc} at v_{dcref} . As the figure shows, a compensator $K_{dc}(s)$ processes the error signal $v_{dc}^2 - v_{dcref}^2$ and issues the setpoint P_{oref} for the real-power-control scheme. Thus, P_o tracks P_{oref} based on the transfer function $H_p(s)$ (Equation (5.30)) and controls v_{dc}^2 . The control from P_o to v_{dc}^2 can be characterized by the power balance equation

$$\left(\frac{C_{dc}}{2\omega_b}\right) \frac{dv_{dc}^2}{dt} \approx P_{DER} - P_o = P_{pv} - P_o, \quad (5.35)$$

which has been represented in Fig. 5.8 by an integrator whose input is $-P_o + P_{pv}$. Since P_{pv} is a nonlinear function of v_{dc} , its effect on the control is eliminated by the addition of a measure of it to the output of $K_{dc}(s)$; the effectiveness of this feedforward compensation is based on the fact that the real-power-control scheme is fast (i.e., $|H_p(j\omega)| \approx 1$). For the loop of Fig. 5.8, $K_{dc}(s)$ can be a pure gain as the control plant possesses a pole at $s = 0$, and since the disturbance P_{pv} has been counteracted by means of a feedforward strategy.

5.4.2 Battery Energy Storage System (BESS)

In the second application, a Battery Energy Storage System (BESS) is considered. Thus, the DER (of the DER system of Fig. 5.1) is assumed to be a battery bank of appropriate voltage level, and P_{DER} and i_{DER} in Fig. 5.1 correspond to P_{bat} and i_{bat} , respectively, where P_{bat} and i_{bat} denote the power and current that the battery bank delivers to the dc-link. The control objective here is to regulate the battery current i_{bat} at its respective setpoint.

Fig. 5.9 illustrates a feedback loop to regulate i_{bat} . As the figure shows, a compensator, $K_{bat}(s)$, processes the error signal $i_{batref} - i_{bat}$ and determines the setpoint P_{oref} for the real-power-control scheme. Then, P_o tracks P_{oref} based on the transfer function $H_p(s)$ and controls i_{bat} . The control from P_o to i_{bat} is characterized by the static relationship

$$i_{bat}v_{dc} = P_{bat} \approx P_o, \quad (5.36)$$

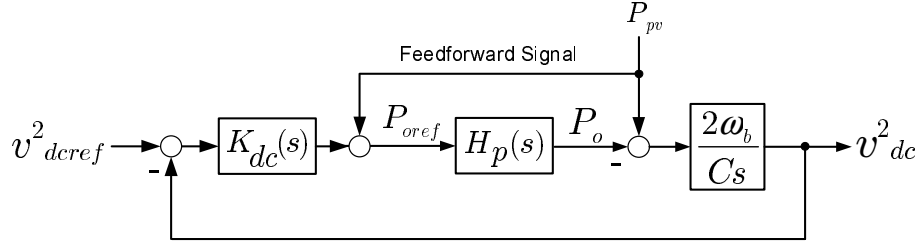


Figure 5.8: Block diagram of the dc-link voltage control scheme for a PV system.

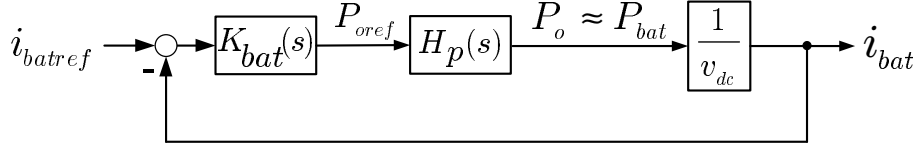


Figure 5.9: Block diagram of the current-control scheme for a battery energy storage system.

which is represented in Fig. 5.9 by a constant gain v_{dc} . The approximation in (5.36) is due to the power losses of the power-electronic interface. Even though the gain $1/v_{dc}$ is not strictly constant, it varies very slowly. To ensure tracking with zero steady-state error, the compensator $K_{bat}(s)$ must have at least one pole at $s = 0$. Such a compensator also compensates for the discrepancy between P_o and P_{bat} that is the result of the power losses.

5.5 Study Cases and Simulation Results

To demonstrate the effectiveness of the proposed unified control strategy, a detailed switched model of a two-system test microgrid has been simulated in the PSCAD/EMTDC software environment [40]; the simulation time step is $10 \mu s$. Fig. 5.10 shows a single-line schematic diagram of the test system and indicates that the microgrid is based on a 12.47-kV radial distribution network which, in turn, consists of two subnetworks: Subnetwork #1 which is energized from the upstream substation through a 1.2-km feeder and the switch S1; and Subnetwork #2 which is energized by Subnetwork #1 through the inter-tie switch S2. In turn, the substation, consisting of the busses Bus #0 and Bus #1 and the transformer Tr3, is energized by a sub-transmission grid which is represented by a 115-kV three-phase voltage source and three (one per phase) 0.1-mH series inductors.

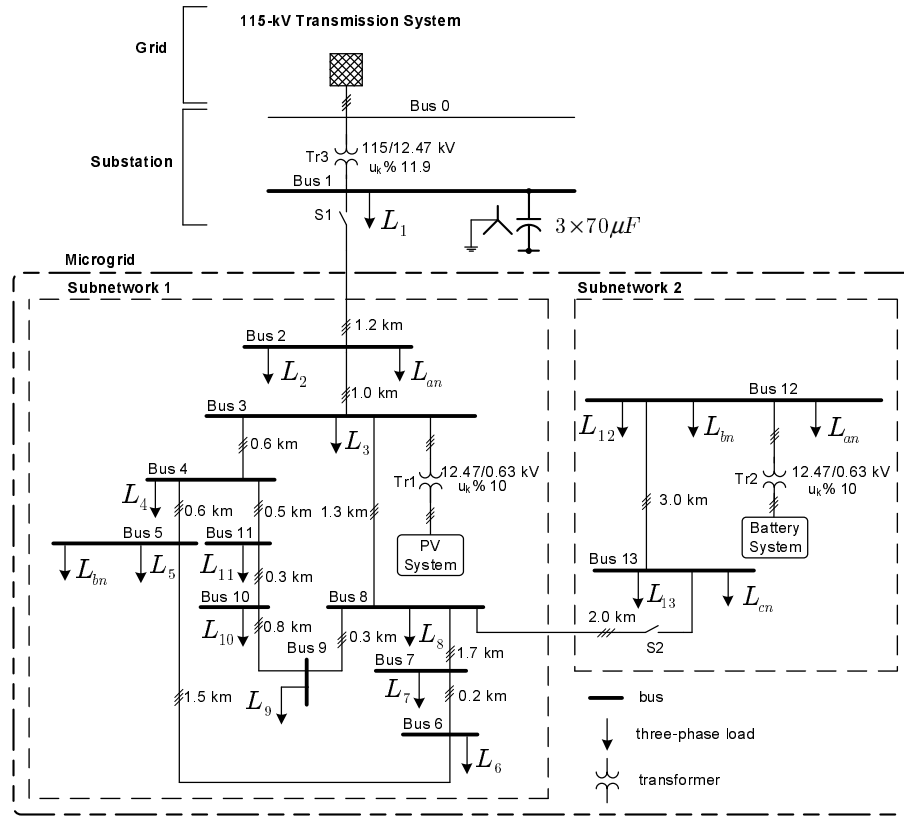


Figure 5.10: Single-line schematic diagram of the test microgrid.

As Fig. 5.10 shows, the distribution network embeds three-phase residential and industrial loads, single-phase loads, and distribution lines. The three-phase loads are denoted by L_i ($i = 1, 2, \dots, 13$), and single-phase loads are denoted by L_{kn} , where the subscript k (being a, b , or c) specifies the phase to which the load is connected (with reference to the neutral conductor). The loads are represented by frequency-invariant constant-impedance static characteristics [56].

Fig. 5.10 further shows that the microgrid embeds two DER systems: a PV system and a BESS. The DER systems are, respectively, interfaced with Bus #3 and Bus #12 of the microgrid through the corresponding interface transformers Tr1 and Tr2. The transformers have a solidly-grounded wye winding configuration at their low-voltage sides. The PV system is a 1.4-MW DER system, whereas the capacity of the BESS is 0.5 MW. In both DER systems, $\tau_i = 0.1$ ms, $\tau_f = 9.0$ ms, and the VSCs are switched at $f_s = 6480$ Hz. Other parameters of the DER systems, the parameters of the loads, and the parameters of the distribution lines are given in Tables D.2–D.4, Appendix D. The length of lines are specified in Fig. 5.10.

5.5.1 Case 1: Response in the Grid-Connected Mode

This case study demonstrates performances of the PV system and BESS under the proposed control strategy, when the microgrid is in the grid-connected mode of operation. In this case the switches S1 and S2 are closed and the microgrid is energized by the grid. At $t = 0$, the PV system and the BESS are turned on with their respective values of V_0 [see Fig. 5.7] ramped up from zero to 1.0 pu. Then, at $t = 0.05$ s, the two DER systems are connected to their respective host busses, subsequent to the synchronization of their output voltages to the grid voltage, through the closure of their corresponding circuit breakers [see Fig. 5.1]. For the PV system, the solar irradiation is assumed to be initially 1.0 kW/m^2 , to step subsequently down to 0.8 kW/m^2 at $t = 0.75$ s, and to step up to 1.0 kW/m^2 at $t = 1.25$ s. For the BESS, i_{batref} is initially set to 0.4 kA (0.208 pu), is stepped down to zero at $t = 0.5$ s, and is stepped further down to -0.3 kA (-0.156 pu) at $t = 1.0$ s; the setpoint is stepped back up to 0.4 kA at $t = 1.5$ s. The reactive-power setpoints of both DER systems are set at zero. Fig. 5.11 illustrates the responses of the two DER systems to the aforementioned sequence of events.

As Fig. 5.11(a) shows, the pre-charged dc-link voltage of the PV system (at no load condition) is equal to 1.57 pu. However, subsequent to the connection of the PV system to the network, the dc-link voltage is changed by the MPPT and dc-link voltage control schemes of the PV system, so that it finally settles at 1.17 pu. Fig. 5.11(b) shows that the PV system starts to deliver real power to the network soon after its start-up at $t = 0.05$ s. Fig. 5.11(b) also shows that the real-power output of the PV system varies in response to the changes in solar irradiation at $t = 0.75$ s and $t = 1.25$ s. Fig. 5.11(c) shows that the reactive-power output of the PV system is regulated at zero while exhibiting excursions when a disturbance impacts the microgrid.

Figs. 5.11(d) and (e) indicate that the battery current tracks its setpoint, and the real-power output of the BESS varies accordingly. The figures also show that the battery current and the real-power output of the BESS can be regulated to be positive, zero, or negative, depending on the desired charging regime. Fig. 5.11(f) shows that the reactive-power output of the BESS is regulated at zero while it is transiently disturbed subsequent to each disturbance incident.

A closer look at the waveforms of the two DER systems reveals that any disturbance im-

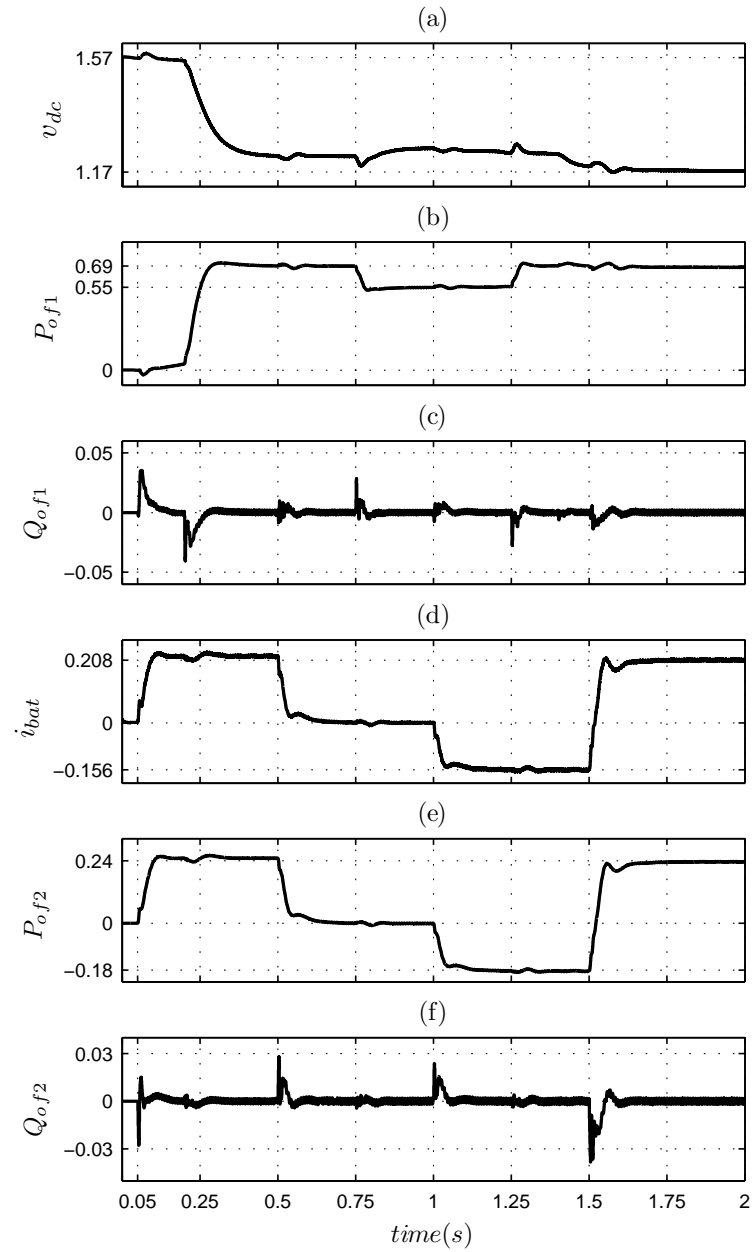


Figure 5.11: System responses in the grid-connected mode (Case 1).

pacting one of the DER systems also disturbs the other DER system. This is mainly due to the fact that the disturbance of a DER system disturbs the amplitude and frequency of the DER system terminal voltage and, thus, also disturbs the terminal voltage amplitude and frequency of the other DER system.

5.5.2 Case 2: Response in the Islanded Mode

This case study demonstrates the responses of the DER systems to a network topological change which results in a power-flow change in the islanded mode of operation, as well as the responses of the DER systems to a three-phase to ground network fault. In this case, the system is initially at the same steady state as the one that it had at the end of Case 1. At $t = 2.5$ s, the switch S1 is opened and, consequently, the aggregate load of Subnetwork #1 and Subnetwork #2 is shared by the two DER systems. At $t = 3.0$ s, a three-phase to ground fault strikes Bus #4, of the network; the fault lasts for 0.1 s during which all three phases of the bus are shorted to the ground through three corresponding 1.0-mH inductors. Figs. 5.12 and 5.13 illustrate the responses of the PV system and BESS to the aforementioned sequence of events.

As Figs. 5.12(a) and 5.12(d) show, subsequent to the islanding incident, the dc-link voltage of the PV system and the battery current stop tracking their respective setpoints, and their values are determined based on the real-power outputs of the two DER systems which, in turn, are determined through the droop strategy and the load demand. Similarly, as Figs. 5.12(b), (c), (e), and (f) indicate, the real and reactive-power outputs of the DER systems no longer track their respective setpoints as they are determined through the droop mechanism enabling power sharing between the two DER systems.

Fig. 5.12 also illustrates the responses of the DER systems to the three-phase to ground fault. As Fig. 5.12 shows, subsequent to the fault incident the real-power outputs of the DER systems drop to almost zero; as Fig. 5.12(a) shows, the PV system dc-link voltage rises to about 1.56 pu which is close to the no-load dc-link voltage of the PV system (i.e., 1.57 pu), and the battery current drops to zero [Fig. 5.12(d)]. Fig. 5.12 further shows that the variables revert to their pre-disturbance values once the fault is cleared. Fig. 5.13 illustrates the waveforms of the VSC ac-side currents of the two DER systems and also the waveform of the voltage of

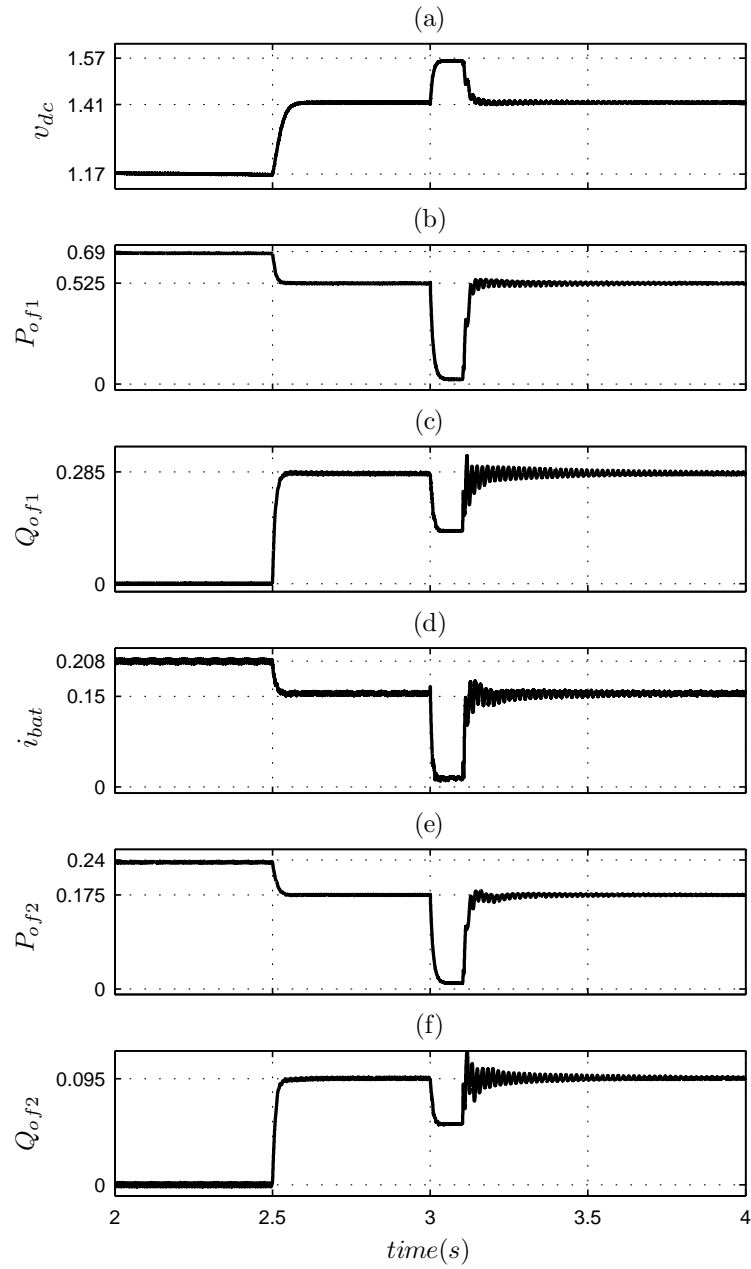


Figure 5.12: System responses in the islanded mode (Case 2).

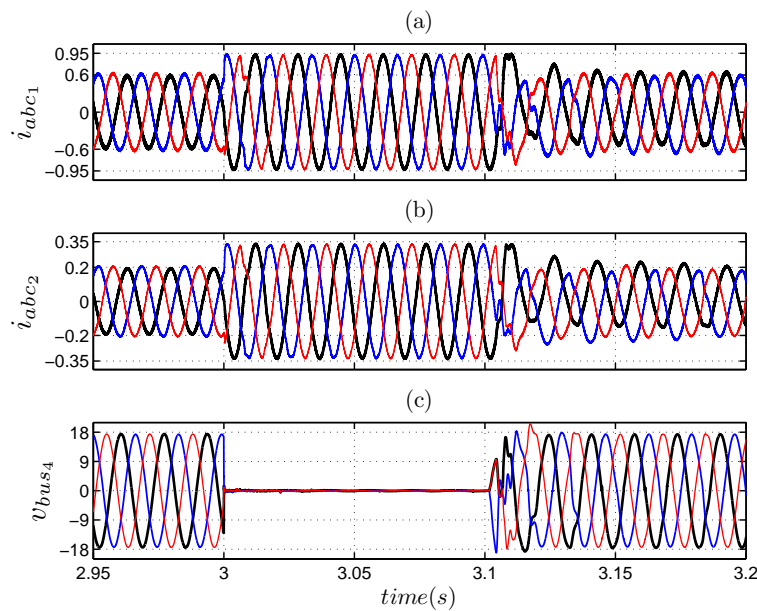


Figure 5.13: Responses of DER systems to a three-phase to ground fault (Case 2).

Bus #4. It is observed that the currents are limited by the current-control schemes of the DER systems despite the fact that Bus #4 voltage has dropped to almost zero. As Fig. 5.13 indicates, under the proposed control strategy the microgrid is able to ride through the fault, and the bus voltage smoothly reclaims its pre-disturbance form and quality once the fault is cleared.

5.6 Conclusion

In this chapter, a unified control strategy is proposed for three-phase electronically-interfaced DERs, to enable them to operate in a microgrid setting with no need for knowing the microgrid mode of operation or switching between different controllers. The proposed control strategy benefits from both active feedback compensation and the droop method, and can be directly adopted for dispatchable systems, e.g., battery energy storage systems, or, alternatively, it can be employed as a part of a nested control loop for non-dispatchable systems. The effectiveness of the proposed strategy under normal conditions and also its capability to ride through network faults were demonstrated through time-domain simulation of a two-system test microgrid in the PSCAD/EMTDC software environment.

Chapter 6

Summary, Conclusions, and Future Work

6.1 Summary and Conclusions

The conclusions of this thesis are as follows:

- The control of amplitude and frequency of DER terminal voltage is an essential requirement in the control of microgrids. The thesis showed that, under balanced load conditions, a control strategy based on multiple control loops (inner current and outer voltage control loops) and augmented with feedforward compensation can effectively regulate the terminal voltage amplitude and mitigate the impacts of load dynamics, inherent inter-coupling, and nonlinearities on the control system. The thesis further discussed that the frequency can be controlled by the q-axis component of the terminal voltage, and that a built-in PLL can be employed to measure the frequency of the terminal voltage.
- It was discussed that the terminal voltage of a DER system can be affected by unbalanced and nonlinear loads, as well as by load switching incidents. The effect of a distorted load current appears as an undesirable harmonic distortion in the terminal voltage. The thesis demonstrated that the repetitive control strategy can effectively mitigate the effect of unbalanced and nonlinear loads and can enhance the performance of the control system. Moreover, a new approach was proposed to maintain the effectiveness of the repetitive control under variable-frequency operational scenarios.
- In the conventional droop-based control method, the dynamics of the DER systems and

those of the overall microgrid, as well as the closed-loop stability are sensitive to the droop coefficients and load characteristics. The thesis proposed an adaptive feedforward compensation strategy that reshapes the dynamic coupling between a DER system and the host microgrid in such a way that the robustness of the microgrid control to droop coefficients and to network dynamic uncertainties is enhanced. It was further shown that the proposed feedforward strategy preserves the steady-state effect that the conventional droop-based control exhibits and, therefore, does not compromise the voltage/frequency regulation or the steady-state power sharing regime within the microgrid. The feedforward compensation is adaptive and, thus, modified periodically according to the system steady-state operating point which, in turn, is estimated through an on-line Recursive Least-Square (RLS) estimation algorithm.

- Finally, The thesis proposed a unified control strategy that enables islanded as well as grid-connected operation of a DER system, with no need to detect the mode of operation or to switch between different controllers. The proposed control strategy enables the control of the real and reactive powers that the power-electronic interface of the DER system exchanges with the host network, and benefits from both active feedback compensation and the droop-based control method. The proposed strategy can be directly adopted for dispatchable systems, e.g., battery energy storage systems, or, alternatively, it can constitute a part of a nested control loop for non-dispatchable systems.

6.2 Future Work

The following topics are suggested for a future work:

- The investigation of the stability of the angle droop method (see [57]). The angle droop method offers a lower frequency drift in comparison with the frequency droop strategy, but its dynamic characteristics are not fully investigated or understood. The combination of the feedforward compensation strategy of Chapter 4 and the angle droop method merits an analytical, comprehensive study.
- The application of decentralized robust control techniques based on frequency response

methods, for eliminating the need for an on-line system identification, can be investigated. In general, adaptive control systems are highly nonlinear and time-varying, and their stability requires the satisfaction of conservative constraints.

- The investigation of centralized control techniques to improve the transient performance of microgrids, and the characterization of bandwidth requirements for wireless communication channels that could be employed for a centralized control architecture. Also, reliability and fault tolerance aspects of a centralized control system based on wireless communications can be investigated.

Appendix A

Load Model and System Parameters for Chapter 2

A.1 Mathematical Model of the Load of Fig. 2.6

To derive the load mathematical equations, let us consider the load RL branch with the following equation

$$L_1 \frac{d\vec{i}_1}{dt} = -R_1 \vec{i}_1 + \vec{v}_s. \quad (\text{A.1})$$

Substituting for $\vec{f} = (f_d + jf_q)e^{j\rho(t)}$ in (A.1), performing the derivatives, and decomposing the resultant into real and imaginary parts, one obtains

$$\begin{aligned} \frac{di_{1d}}{dt} &= -\frac{R_1}{L_1}i_{1d} + \omega i_{1q} + \frac{1}{L_1}v_{sd} \\ \frac{di_{1q}}{dt} &= -\omega i_{1d} - \frac{R_1}{L_1}i_{1q} + \frac{1}{L_1}v_{sq}. \end{aligned} \quad (\text{A.2})$$

Therefore, the RL branch of the load has two state variables, receives the inputs v_{sd} , v_{sq} , and ω , and provides the outputs i_{1d} and i_{1q} .

Similarly, the *RLC* branch of the load is described by

$$\begin{aligned}\frac{di_{2d}}{dt} &= -\frac{R_2}{L_2}i_{2d} + \omega i_{2q} + \frac{1}{L_2}v_{sd} - \frac{1}{L_2}v_d \\ \frac{di_{2q}}{dt} &= -\omega i_{2d} - \frac{R_2}{L_2}i_{2q} + \frac{1}{L_2}v_{sq} - \frac{1}{L_2}v_q,\end{aligned}\quad (\text{A.3})$$

and

$$\begin{aligned}\frac{dv_d}{dt} &= \omega v_q + \frac{1}{C_2}i_{2d} \\ \frac{dv_q}{dt} &= -\omega v_d + \frac{1}{C_2}i_{2q}.\end{aligned}\quad (\text{A.4})$$

Thus, the *RLC* branch of the load has four state variables, receives the inputs v_{sd} , v_{sq} , and ω , and provides the outputs i_{2d} and i_{2q} .

Since, $i_{Labc} = i_{1abc} + i_{2abc}$, then and

$$\begin{aligned}i_{Ld} &= g_1(i_{1d}, i_{1q}, i_{2d}, i_{2q}, v_{sd}, v_{sq}, \omega) \\ i_{Lq} &= g_2(i_{1d}, i_{1q}, i_{2d}, i_{2q}, v_{sd}, v_{sq}, \omega).\end{aligned}\quad (\text{A.5})$$

Equations (A.2) to (A.5) describe the dynamics of the load of Fig. 2.6 and include six state variables, the three inputs v_{sd} , v_{sq} , and ω , and the two outputs i_{Ld} and i_{Lq} . It is noted that the equations are nonlinear.

A.2 System Parameters

The DER system parameters are $L = 100 \mu\text{H}$, $C_f = 500 \mu\text{F}$, $R = 1.5 \text{ m}\Omega$, $v_{dc} = 1.6 \text{ kV}$, and the switching frequency $f_s = 3420 \text{ Hz}$.

The compensator of the current control scheme has the transfer function

$$K_i(s) = \frac{s + 15}{s} \quad [\Omega]$$

corresponding to $\tau_i = 0.1 \text{ ms}$.

The compensators of the voltage and frequency control loops have the transfer functions

$$K_v(s) = \frac{1.66s + 1844}{s} \quad [\Omega^{-1}]$$

$$K_\omega(s) = 0.01[\text{kVs}]$$

The transfer function of the PLL filter is

$$H(s) = 4.7 \frac{s + 133.85}{s(s + 1195)} \quad [\text{kVs}]^{-1}$$

The parameters of the passive load of Fig. 2.6 are $R_1 = 83 \text{ m}\Omega$, $L_1 = 137 \text{ }\mu\text{H}$, $R_2 = 50 \text{ m}\Omega$, $L_2 = 68 \text{ }\mu\text{H}$, and $C_2 = 13.55 \text{ mF}$.

The parameters of the induction machine are $R_r = 0.0132 \text{ pu}$, $R_s = 0.0184 \text{ pu}$, $L_m = 3.8 \text{ pu}$, $L_{lr} = 0.0223 \text{ pu}$, and $L_{ls} = 0.0223 \text{ pu}$. The machine has two poles, and its rated power, voltage, and frequency are 0.8 MVA, 0.868 kV (line-to-line, rms), and 377 rad/s, respectively.

Appendix B

Load and System Parameters for Chapter 3

In the case studies of Chapter 3, the balanced load consists of three star-connected series RL circuits, with the per-phase resistance and inductance of $170\text{ m}\Omega$ and $218\text{ }\mu\text{H}$, respectively. The unbalanced load consist of a series RL circuit between phase-a and the neutral conductor; the load resistance and inductance are $17\text{ m}\Omega$ and $21.8\text{ }\mu\text{H}$, respectively, and its two other phases are open. The nonlinear load is a three-phase six-pulse diode-bridge rectifier whose dc side supplies a series RL branch with a resistance of $700\text{ m}\Omega$ and an inductance of $20\text{ }\mu\text{H}$. Schematic diagram of the rectifier three phase load and its interfacing transformer, Tr3, are shown in Fig. B.1. The circuit and system parameters of the DER system are given in Table B.1.

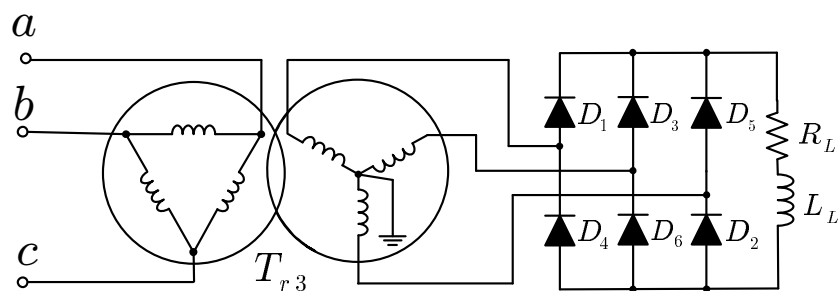


Figure B.1: Schematic diagram of the rectifier three-phase load.

Table B.1: DER System Circuit and Control Parameters

Parameter	Value	Remark
L	300 [μH]	
C_f	500 [μF]	
R	3.0 [$m\Omega$]	
v_{dc}	1.8 [kV]	
f_s	6480 [Hz]	switching & sampling frequency
k_p	10 [kVs] ⁻¹	
k_ω	0.005 [kVs]	
α	0.9969	
V_0	0.5 [kV]	
ω_0	377 [rad/s]	
n & \bar{n}	0.02 [kV/MVAr]	
Tr	4.16/0.69 [kV(rms)]	leakage reactance 8%
Tr1, Tr3	4.16/0.69 [kV(rms)]	leakage reactance 10%
Tr2	4.16/0.208 [kV(rms)]	leakage reactance 10%

Appendix C

Load, System, and Asynchronous Machine Parameters for Chapter 4

C.1 System Parameters

The system parameters are given in Table C.1. The transfer functions $K_i(z)$ and $K_v(z)$ are given by (C.1) to (C.4).

$$K_i(z) = 0.973z(z - 0.998)/(z^2 - 1) [\Omega], \text{ for DER1} \quad (\text{C.1})$$

$$K_v(z) = 1.5(z - 0.995)/(z - 1) [\Omega^{-1}], \text{ for DER1} \quad (\text{C.2})$$

$$K_i(z) = 1.945z(z - 0.998)/(z^2 - 1) [\Omega], \text{ for DER2} \quad (\text{C.3})$$

$$K_v(z) = 0.950z(z - 0.995)/(z - 1) [\Omega^{-1}], \text{ for DER2.} \quad (\text{C.4})$$

C.2 Asynchronous Machine Parameters

Asynchronous machine parameters are given in Table C.2.

Table C.1: DER Systems Circuit and Control Parameters

Parameter	Value	Remark
L_1	150 [μ H]	DER1
C_{f1}	1000 [μ F]	DER1
R_1	1.5 [m Ω]	DER1
L_2	300 [μ H]	DER2
C_{f2}	500 [μ F]	DER2
R_2	3.0 [m Ω]	DER2
v_{dc}	1.8 [kV]	DER1 and DER2
f_s	6480 [Hz]	switch. & sampl. freq.
k_p	10 [(kVs) $^{-1}$]	DER1 and DER2
k_ω	0.005 [kVs]	DER1 and DER2
λ	0.997	forgetting factor
α_1	0.9969	
α_2	0.98	
ω_0	381 [rad/s]	
V_0	0.52 [kV]	
m_1	2.0 [(rad/s)/MW]	DER1
n_1	0.02 [kV/MVAr]	DER1
m_2	4.0 [(rad/s)/MW]	DER2
n_2	0.04 [kV/MVAr]	DER2

Table C.2: Asynchronous Machine Parameters (Case 4)

Parameter	Value	Remark
nominal power	0.75 [MVA]	
nominal voltage	0.69 [kV]	line-to-line, rms
nominal frequency	377 [rad/s]	
rotor/stator turns ratio	2.6376	
stator resistance, R_s	0.0034	per-unit
rotor resistance, R_r	0.00607	per-unit
magnetizing inductance, L_m	3.9	per-unit
stator inductance, L_s	3.9102	per-unit
rotor inductance, L_r	3.911	per-unit

C.3 Load and Distribution Line Parameters

The three-phase load parameters and distribution line parameters of the test microgrid of Fig. 4.8 are given in Tables C.3 and C.4. The schematic diagram of the single phase network is shown in Fig. C.1 and its load parameters are given in Table C.5. In Tables C.3 and C.5 the real and reactive powers of the loads are expressed in MW and MVA.

Table C.3: Three-Phase Load Parameters

Load	Phase A	Phase B	Phase C
L_1	$7.3302 + j3.3555$	$6.8022 + j3.0722$	$6.6522 + j3.1546$
L_2	$0.2650 + j0.1366$	$0.3025 + j0.1736$	$0.4450 + j0.2205$
L_3	$0.0640 + j0.0480$	$0.2440 + j0.1352$	$0.1090 + j0.0698$
L_4	$0.1800 + j0.0872$	$0.0900 + j0.0436$	$0.0900 + j0.0436$
L_5	$0.2325 + j0.0888$	$0.1700 + j0.0536$	$0.0425 + j0.0263$
L_6	$0.0475 + j0.0156$	$0.0950 + j0.0312$	$0.2582 + j0.0933$
L_7	$0.0950 + j0.0312$	$0.1900 + j0.0624$	$0.0950 + j0.0312$
L_8	$0.0900 + j0.0436$	$0.1350 + j0.0654$	$0.1800 + j0.0872$
L_9	$0.0950 + j0.0312$	$0.1425 + j0.0468$	$0.0950 + j0.0312$
L_{10}	$0.1350 + j0.0654$	$0.0900 + j0.0436$	$0.2250 + j0.1090$
L_{11}	$0.1750 + j0.0946$	$0.1750 + j0.0946$	$0.1275 + j0.0790$
L_{12}	$2.0502 + j1.0834$	$2.0502 + j1.0834$	$2.0502 + j1.0834$
L_{13}	$0.1912 + j0.1343$	$0.1912 + j0.1343$	$0.1912 + j0.1343$
L_{14}	$0.0810 + j0.0392$	$0.0810 + j0.0392$	$0.0810 + j0.0392$

Table C.4: Distribution Line Parameters [1/km]

Parameter	Value
Positive-Sequence Series Resistance	173 [mΩ]
Positive-Sequence Series Reactance	432 [mΩ]
Positive-Sequence Shunt Susceptance	3.831×10^{-6} [1/Ω]
Zero-Sequence Series Resistance	351 [mΩ]
Zero-Sequence Series Reactance	1800 [mΩ]
Zero-Sequence Shunt Susceptance	1.57×10^{-6} [1/Ω]

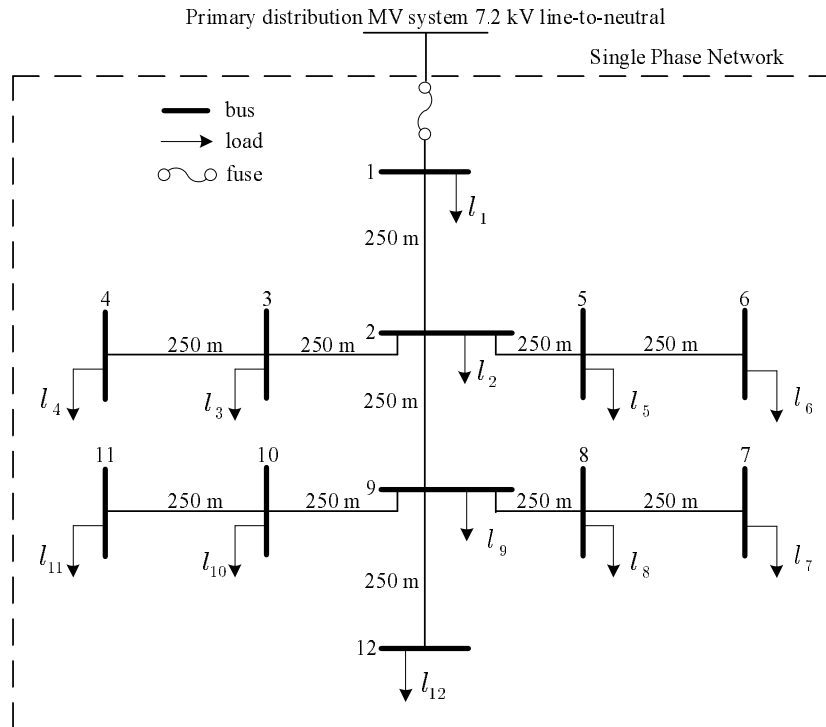


Figure C.1: Schematic diagram of the single-phase network.

Table C.5: Single-Phase Load Parameters

Load	Power
l_1	$0.0135 + j0.0065$
l_2	$0.0142 + j0.0047$
l_3	$0.0135 + j0.0065$
l_4	$0.0135 + j0.0065$
l_5	$0.0095 + j0.0031$
l_6	$0.0475 + j0.0156$
l_7	$0.0475 + j0.0156$
l_8	$0.0095 + j0.0031$
l_9	$0.0475 + j0.0156$
l_{10}	$0.0135 + j0.0065$
l_{11}	$0.0095 + j0.0031$
l_{12}	$0.0095 + j0.0031$

Appendix D

Base Values and System Parameters for Chapter 5

The base values of quantities are reported in Table D.1. The parameters of the DER systems, the parameters of the loads, and the parameters of the distribution lines are given in Tables D.2–D.4

Table D.1: Base Values

Base	Metric Value	Remark
P_b	2.0 [MVA]	base power
V_b	0.52 [kV]	base voltage
I_b	2.56 [kA]	$2P_b/(3V_b)$
ω_b	377 [rad/s]	grid nominal frequency
Z_b	202.8 [m Ω]	$3V_b^2/(2P_b)$
Y_b	4.931 [S]	$1/Z_b$
L_b	538 [μ H]	Z_b/ω_b
C_b	13079 [μ F]	Y_b/ω_b
m_b	188.5 [(rad/s)/MW]	ω_b/P_b
n_b	0.26 [kV/MVAr]	V_b/P_b
P_{b-dc}	2.0 [MW]	base dc power (P_b)
V_{b-dc}	1.04 [kV]	base dc voltage ($2V_b$)
I_{b-dc}	1.923 [kA]	P_{b-dc}/V_{b-dc}
C_{b-dc}	4904 [μ F]	$3C_b/8$

Table D.2: DER Systems Circuit and Control Parameters [pu]

Parameter	Value	Remark
L	0.278	PV
C_f	0.038	PV
R	0.0098	PV
C_{dc}	8.16	PV
L	1.115	BESS
C_f	0.0095	BESS
R	0.039	BESS
v_{dc}	1.15	BESS
C_{dc}	0.0203	BESS
ω_0	1.0	Both
V_0	1.0	Both
m	0.0212	PV
n	0.0384	PV
m	0.0636	BESS
n	0.115	BESS
k_ω	14.5	Both
$K_v(s)$	$0.369(s^2 + 1492s + 989011)/(s^2 + 568516)$	PV
$K_v(s)$	$0.092(s^2 + 1492s + 989011)/(s^2 + 568516)$	BESS
$K_p(s)$	$1.06(s^2 + 111s + 5816)/(13.1s^2 + 1454s)$	PV
$K_p(s)$	$0.344(s^2 + 111s + 5816)/(4.3s^2 + 477s)$	BESS
$K_q(s)$	$0.0769(s + 250)/s$	PV
$K_q(s)$	$0.231(s + 250)/s$	BESS
$K_{dc}(s)$	0.2	PV
$K_{bat}(s)$	$1.44(s + 30)/s$	BESS

Table D.3: Load Parameters [pu]

Load	Phase A	Phase B	Phase C
L_1	$0.916 + j0.419$	$0.850 + j0.384$	$0.831 + j0.394$
L_2	$0.033 + j0.017$	$0.038 + j0.022$	$0.056 + j0.027$
L_3	$0.008 + j0.006$	$0.030 + j0.017$	$0.014 + j0.009$
L_4	$0.022 + j0.011$	$0.011 + j0.005$	$0.011 + j0.005$
L_5	$0.029 + j0.011$	$0.021 + j0.007$	$0.005 + j0.003$
L_6	$0.006 + j0.002$	$0.012 + j0.004$	$0.032 + j0.012$
L_7	$0.012 + j0.004$	$0.024 + j0.008$	$0.012 + j0.004$
L_8	$0.011 + j0.005$	$0.017 + j0.008$	$0.022 + j0.011$
L_9	$0.012 + j0.004$	$0.018 + j0.006$	$0.012 + j0.004$
L_{10}	$0.017 + j0.008$	$0.011 + j0.005$	$0.028 + j0.014$
L_{11}	$0.022 + j0.012$	$0.022 + j0.012$	$0.016 + j0.010$
L_{12}	$0.024 + j0.017$	$0.024 + j0.017$	$0.024 + j0.017$
L_{13}	$0.010 + j0.005$	$0.010 + j0.005$	$0.010 + j0.005$
L_{an}	$0.032 + j0.017$	0	0
L_{bn}	0	$0.032 + j0.017$	0
L_{cn}	0	0	$0.032 + j0.017$

Table D.4: Distribution Line Parameters [1/km]

Parameter	Value
Positive-Sequence Series Resistance	173 [m Ω]
Positive-Sequence Series Reactance	432 [m Ω]
Positive-Sequence Shunt Susceptance	3.831×10^{-6} [1/ Ω]
Zero-Sequence Series Resistance	351 [m Ω]
Zero-Sequence Series Reactance	1800 [m Ω]
Zero-Sequence Shunt Susceptance	1.57×10^{-6} [1/ Ω]

Bibliography

- [1] H. L. Willis and W. G. Scott, *Distributed Power Generation*, Marcel Dekker, New York, 2000.
- [2] N. Hatziargyriou, H. Assano, R. Iravani and C. Marnay, "Microgrids," *IEEE Power and Energy Magazine*, vol. 5, no. 4, pp. 78-94, July-August 2007.
- [3] R. H. Lasseter and P. Paigi, "Microgrids: a conceptual solution," Proceedings of Power Electronics Specialists Conference, PESC04, pp. 4285-4290, June 2004.
- [4] F. Katiraei, R. Iravani, N. Hatziargyriou and A. Dimeas, "Microgrids management," *IEEE Power and Energy Magazine*, vol. 6, no. 3, pp. 54-65, May-June 2008.
- [5] B. Kroposki, R. Lasseter, T. Ise, S. Morozumi, S. Papathanassiou and N. Hatziargyriou, "Making microgrids work," *IEEE Power and Energy Magazine*, vol. 6, no. 3, pp. 40-53, May-June 2008.
- [6] H. Nikkhajoei and R. H. Lasseter, "Distributed generation interface to the CERTS micro-grid," *IEEE Transactions on Power Delivery*, vol. 24, no. 3, pp. 1598-1608, July 2009.
- [7] F. Katiraei, M. R. Iravani and P. W. Lehn, "Small-signal dynamic model of a micro-grid including conventional and electronically interfaced distributed resources," *IET Generation, Transmission and Distribution*, vol. 1, no. 3, pp. 369-378, May 2007.
- [8] J. A. Peças Lopes, C. L. Moreira and A. G. Madureira, "Defining control strategies for microgrids islanded operation," *IEEE Transactions on Power Systems*, vol. 21, no. 2, pp. 916-923, May 2006.

- [9] A. L. Dimeas and N. D. Hatziargyriou, "Operation of a multiagent system for microgrid control," *IEEE Transactions on Power Systems*, vol. 20, no. 3, pp. 1447-1455, August 2005.
- [10] A. Yazdani and R. Iravani, *Voltage-Sourced Converters in Power Systems*, IEEE/John-Wiley, 2010.
- [11] M. P. Kazmierkowski and L. Malesani, "Current-control techniques for three-phase voltage-source PWM converters: a survey," *IEEE Transactions on Industrial Electronics*, vol. 45, no. 5, pp. 691-703, October 1998.
- [12] A. Yazdani, A. R. Di Fazio, H. Ghoddami, M. Russo, M. Kazerani, J. Jatskevich, K. Strunz, S. Leva and J. A. Martinez "Modeling guidelines and a benchmark for power system simulation studies of three-phase single-stage photovoltaic systems," *IEEE Transactions on Power Delivery*, vol. 26, no. 2, pp. 1247-1264, April 2011.
- [13] A. G. Tsikalakis and N. D. Hatziargyriou, "Centralized control for optimizing microgrids operation," *IEEE Transactions on Energy Conversion*, vol. 23, no. 1, pp. 241-248, March 2008.
- [14] T. C. Green and M. Prodanović, "Control of inverter-based microgrids," *Electric Power Systems Research*, vol. 77, no. 9, pp. 1204-1213, July 2007.
- [15] Y. W. Li, D. M. Vilathgamuwa and P. C. Loh, "Design, analysis, and real-time testing of a controller for multibus microgrid system," *IEEE Transactions on Power Electronics*, vol. 19, no. 5, pp. 1195-1204, September 2004.
- [16] C. K. Sao and P. W. Lehn, "Control and power management of converter fed microgrids," *IEEE Transactions on Power Systems*, vol. 23, no. 3, pp. 1088-1098, August 2008.
- [17] H. Karimi, H. Nikkhajoei and R. Iravani "A linear quadratic gaussian controller for a stand-alone distributed resource unit-simulation case studies," IEEE Power Engineering Society General Meeting, PES07, June 2007.

- [18] H. Karimi, H. Nikkhajoei and M. R. Iravani, "Control of an electronically-coupled distributed resource unit subsequent to an islanding event," *IEEE Transactions on Power Delivery*, vol. 23, no. 1, pp. 493-501, January 2008.
- [19] C. K. Sao and P. W. Lehn, "Intentional islanded operation of converter fed microgrids," *IEEE Transactions on Power Delivery*, vol. 20, no. 2, pp. 1009-1016, April 2005.
- [20] C. K. Sao and P. W. Lehn, "Intentional islanded operation of converter fed microgrids," IEEE Power Engineering Society General Meeting, PES06, 6 pages, June 2006.
- [21] C. K. Sao and P. W. Lehn, "Voltage balancing of converter fed microgrids with single phase loads," IEEE Power and Energy Society General Meeting, PES08, 7 pages, July 2008.
- [22] C. K. Sao, "Autonomous load sharing of voltage source inverters," MSc Thesis, University of Toronto, 2002.
- [23] A. Yazdani, "Control of an islanded distributed energy resource unit with load compensating feed-forward," IEEE Power and Energy Society General Meeting, PES08, 7 pages, July 2008.
- [24] F. Katiraei and M. R. Iravani, "Power management strategies for a microgrid with multiple distributed generation units," *IEEE Transactions on Power Systems*, vol. 21, no. 4, pp. 1821-1831, November 2006.
- [25] M. C. Chandorkar, D. M. Divan and R. Adapa, "Control of parallel connected inverters in standalone ac supply systems," *IEEE Transactions on Industry Applications*, vol. 29, no. 1, pp. 136-143, January-February 1993.
- [26] N. Pogaku, M. Prodanovic, T. C. Green, W. L. Kling and L. Van Der Sluis, "Modeling, analysis and testing of autonomous operation of an inverter-based microgrid," *IEEE Transactions on Power Electronics*, vol. 22, no. 2, pp. 613-625, March 2007.
- [27] K. D. Brabandere, B. Bolsens, J. V. D. Keybus, A. Woyte, J. Driesen and R. Belmans, "A voltage and frequency droop control method for parallel inverters," *IEEE Transactions on Power Electronics*, vol. 22, no. 4, pp. 1107-1115, July 2007.

- [28] Y. A. I. Mohamed and E. F. El-Saadany, "Adaptive decentralized droop controller to preserve power sharing stability of paralleled inverters in distributed generation microgrids," *IEEE Transactions on Power Electronics*, vol. 23, no. 6, pp. 2806-2816, November 2008.
- [29] J. M. Guerrero, L. G. de Vicuna, J. Matas, M. Castilla and J. Miret, "A wireless controller to enhance dynamic performance of parallel inverters in distributed generation systems," *IEEE Transactions on Power Electronics*, vol. 19, no. 5, pp. 1205-1213, September 2004.
- [30] E. Rokrok and M. E. H. Golshan, "Adaptive voltage droop scheme for voltage source converters in an islanded multibus microgrid," *IET Generation, Transmission and Distribution*, vol. 4, no. 5, pp. 562-578, May 2010.
- [31] G. Diaz, C. Gonzales-Moran, J. Gomez-Aleixandre and A. Diez, "Complex-valued state matrices for simple representation of large autonomous microgrids supplied by PQ and Vf generation," *IEEE Transactions on Power Systems*, vol. 24, no. 4, pp. 1720-1730, November 2009.
- [32] H. Karimi, E. J. Davison and R. Iravani, "Multivariable servomechanism controller for autonomous operation of a distributed generation unit: design and performance evaluation," *IEEE Transactions on Power Systems*, vol. 25, no. 2, pp. 853-865, May 2010.
- [33] H. Karimi, A. Yazdani and R. Iravani, "Robust control of an autonomous four-wire electronically-coupled distributed generation unit," *IEEE Transactions on Power Delivery*, vol. 26, no. 1, pp. 455-466, January 2011.
- [34] C. Chen, Y. Wang, J. Lai, Y. Lee and D. Martin "Design of parallel inverters for smooth mode transfer microgrid applications," *IEEE Trans. on Power Electronics*, vol. 25, no. 1, pp. 6-15, January 2010.
- [35] F. Kariraei and R. Iravani, "Micro-grid autonomous operation during and subsequent to islanding process," *IEEE Transactions on Power Delivery*, vol. 20, no. 1, pp. 448-257, January 2005.

- [36] J. M. Guerrero, J. C. Vázquez, J. Matas, M. Castilla and L. G. Vicuña, "Control strategy for flexible microgrid based on parallel line-interactive UPS systems," *IEEE Transactions on Industrial Electronics*, vol. 56, no. 3, pp. 726-736, March 2009.
- [37] Se-Kyo Chung, "A phase tracking system for three phase utility interface inverters" *IEEE Transactions on Power Electronics*, vol. 15, no. 3, pp. 431-438, May 2000.
- [38] C. Schauder and H. Mehta, "Vector analysis and control of advanced static VAR compensators," *IEE Proceedings Generation, Transmission, and Distribution*, vol. 140, no. 4, pp. 299-306, July 1993.
- [39] W. Leonhard, *Control of Electrical Drives*, 3rd edition, Springer-Verlag, 2001.
- [40] PSCAD/EMTDC v. 4.2, Manitoba HVDC Research Centre, Winnipeg, MB, Canada.
- [41] T. Kawabata, T. Miyashita and Y. Yamamoto, "Dead beat control of three phase PWM inverter" *IEEE Transactions on Power Electronics*, vol. 5, no. 1, pp. 21-28, January 1990.
- [42] B. A. Francis and W. M. Wonham, "The internal model principle for linear multivariable regulators," *Applied Mathematics and Optimization*, vol. 2, no. 4, pp. 170-194, December 1975.
- [43] M. Steinbuch, "Repetitive control for systems with uncertain period-time," *Automatica*, vol. 38, no. 12, pp. 2103-2109, December 2002.
- [44] T. I. Laakso, V. Välimäki, M. Karjalainen and U. K. Laine, "Splitting the unit delay," *IEEE Signal Processing Magazine*, vol. 13, no. 1, pp. 30-60, January 1996.
- [45] G. Oetken, "A new approach for the design of digital interpolating filters," *IEEE Transactions on Acoustics, Speech and Signal Processing*, vol. 27, no. 6, pp. 637-643, December 1979.
- [46] K. K. Chew and M. Tomizuka, "Steady-state and stochastic performance of a modified discrete-time prototype repetitive controller," *ASME, Journal of Dynamic Systems, Measurement, and Control*, vol. 112, no. 1, pp. 35-41, March 1990.

- [47] G. Hillerström, “Adaptive suppression of vibrations—a repetitive control approach,” *IEEE Transactions on Control Systems Technology*, vol. 4, no. 1, pp. 72-78, January 1996.
- [48] F. R. Shaw and K. Srinivasan, “Discrete-time repetitive control system design using the regeneration spectrum,” *ASME, Journal of Dynamic Systems, Measurement, and Control*, vol. 115, no. 2, pp. 228-237, June 1993.
- [49] *IEEE recommended Practice for monitoring electric power quality*, IEEE Std. 1159-2009.
- [50] *IEEE recommended practice for electric power systems in commercial buildings*, ANSI/IEEE Std. 241-1990, (Gray Book).
- [51] *IEEE recommended practice for electric power distribution for industrial plants*, ANSI/IEEE Std. 141-1993, (Red Book).
- [52] S. R. Bowes and M. J. Mount, “Microprocessor control of PWM inverters,” *IEE Proceedings B Electric Power Application*, vol. 128, no. 6, pp. 293-305, November 1981.
- [53] A. Medio and M. Lines, *Nonlinear Dynamics: A Primer*, Cambridge University Press, 2001.
- [54] K. J. Åström and B. Wittenmark, *Adaptive control*, Addison-Wesley, second edition, 1995.
- [55] CIGRE Task Force C6.04.02, “Benchmark systems for network integration of renewable and distributed energy resources, CIGRE technical brochure,” 2011.
- [56] P. Kundur, *Power System Stability and Control*, McGraw-Hill, New York, 1994.
- [57] R. Majumder, B. Chaudhuri, A. Ghosh, R. Majumder, G. Ledwich and F. Zare, “Improvement of stability and load sharing in an autonomous microgrid using supplementary droop control loop,” *IEEE Transactions on Power Systems*, vol. 25, no. 2, pp. 796-808, May 2010.

Curriculum Vitae

Name: Mohammad Bagher Delghavi

Post-Secondary Education and Degrees: The University of Western Ontario
London, ON
2008 - 2011 Ph.D.

Iran University of Science and Technology
Tehran, Iran
1993-1996 M. Sc.

University of Urmia
Urmia, Iran
1989-1993 B. Sc.

Honours and Awards: Ontario Graduate Scholarship, 2011-2012
Western Engineering Scholarship since May 2008

Related Work Experience: Teaching Assistant
The University of Western Ontario
2008 - 2011

Research Assistant
The University of Western Ontario
2008 - 2011

Publications:

- M. B. Delghavi and A. Yazdani, "A unified control strategy for electronically-interfaced distributed energy resources in grid-tied and microgrid applications," Submitted to the IEEE Transactions on Power Delivery.
- M. B. Delghavi and A. Yazdani, "An adaptive feedforward compensation for stability enhancement in droop-controlled inverter-based microgrids," *IEEE Transactions on Power Delivery*, vol. 26, no. 3, pp. 1764-1773, July 2011.

- M. B. Delghavi and A. Yazdani, "Islanded-mode control of electronically-coupled distributed resource (DR) units under unbalanced and nonlinear load conditions," *IEEE Transactions on Power Delivery*, vol. 26, no. 2, pp. 661-673, April 2011.
- M. B. Delghavi and A. Yazdani, "A control strategy for islanded operation of a distributed resource (DR) unit," IEEE Power and Energy Society General Meeting, PES09, 8 pages, July 2009.